MATHEMATICAL SCIENCES

Collective scattering of subwavelength resonators in metamaterial systems

by

Derek Wesley Watson

A thesis submitted in partial fulfillment for the
degree of Doctor of Philosophy

in the
FACULTY OF SOCIAL, HUMAN AND MATHEMATICAL SCIENCES
MATHEMATICAL SCIENCES

August 15, 2017

MATHEMATICAL SCIENCES

ABSTRACT

FACULTY OF SOCIAL, HUMAN AND MATHEMATICAL SCIENCES
MATHEMATICAL SCIENCES

Doctor of Philosophy

COLLECTIVE SCATTERING OF SUBWAVELENGTH RESONATORS IN METAMATERIAL SYSTEMS

by Derek Wesley Watson

In this thesis, we model the electromagnetic (EM) interactions between plasmonic resonators and an incident EM field. By capturing the fundamental physics of each resonator, such as its resonance frequency and radiative decay rate, the dynamics of the EM interactions can be modeled by a linear set of equations. The system's eigenmodes exhibit characteristic line shifts and linewidths that may be subradiant or superradiant.

For simple resonator systems, we approximate each resonator as a point electric dipole. Nanorods and nanobars, are such resonators where the magnetization can be assumed to be negligible. However, closely spaced parallel electric dipoles can exhibit EM properties similar to higher order multipoles, e.g., electric quadrupoles. We show how, in an original way, simple systems comprising closely spaced parallel pairs of electric dipoles can be approximated as electric quadrupole and magnetic dipole resonators. When the resonators are close, their finite-size and geometry is important to the EM interactions, and we show how we cope with these important factors in our model.

We analyze in detail a nanorod configuration comprising pairs of plasmonic nanorods – a toroidal metamolecule, and show how the elusive toroidal dipole moment appears as a radiative eigenmode. In this original work, we find that the radiative interactions in the toroidal metamolecule can be qualitatively represented by our point electric dipole approximation and finite-size resonator model. The results demonstrate how the toroidal dipole moment is subradiant and difficult to excite by incident light. By means of breaking the geometric symmetry of the metamolecule, we show the toroidal mode can be excited by linearly polarized light and that it appears as a Fano resonance dip in the forward scattered light. We provide simple optimization protocols for maximizing the toroidal dipole mode excitation. This opens up possibilities for simplified control and driving of metamaterial arrays consisting of toroidal dipole unit-cell resonators.

Contents

List of Figures

List of Tables

Declaration of Authorship

I, Derek Wesley Watson, declare that the thesis entitled *Collective scattering of subwavelength resonators in metamaterial systems* and the work presented in the thesis are both my own, and have been generated by me as the result of my own original research. I confirm that:

- this work was done wholly or mainly while in candidature for a research degree at this University;
- where any part of this thesis has previously been submitted for a degree or any other qualification at this University or any other institution, this has been clearly stated;
- where I have consulted the published work of others, this is always clearly attributed;
- where I have quoted from the work of others, the source is always given. With the exception of such quotations, this thesis is entirely my own work;
- I have acknowledged all main sources of help;
- where the thesis is based on work done by myself jointly with others, I have made clear exactly what was done by others and what I have contributed myself;
- parts of this work have been published as: [1] and [2].

Signed:..

Date:...

Acknowledgements

Above all I would like to thank: my supervisors Professor Janne Ruostekoski and Dr Vassili A. Fedotov for the opportunity to study for a PhD in mathematics; the EPSRC for funding the project; and Dr Stewart D. Jenkins for his support and invaluable discussions throughout my studies at Southampton.

A special thank you to my parents; who never questioned why I should want to change my career and try my hand at academic research and have supported me in countless ways.

Finally, I would like to thank Marie and ‘Betty’ who kept me sane at the worst of times.

Chapter 1

Introduction

1.1 An introduction to metamaterials

1.1.1 What are metamaterials?

‘Metamaterials’ are artificial media which, through design, exhibit electromagnetic (EM) functions not observed in natural materials. The constituent components of the metamaterial are circuit element resonators distributed about a periodic array, whose spacings are much smaller than the wavelength of the incident light. It is through the design of these ‘subwavelength spaced resonators’ that metamaterials realize their properties. This is in contrast to natural materials, whose EM properties depend on their atomic and molecular structure.

1.1.2 A brief history motivating further study

The explicit concept of metamaterials in optical physics arguably began with Veselago in 1967, who demonstrated theoretically the concept of left-handed metamaterials [3]. These materials have simultaneously negative permittivity and permeability, therefore a negative index of refraction. The physical realization of left-handed metamaterials was not achieved until 1999 when Sir John Pendry proposed two oppositely facing, discontinuous, metallic loops (split ring resonators (SRRs)) as a means of achieving negative permeability [4, 5]. This was followed in 2000 when Smith et. al., demonstrated the concept experimentally [6, 7].

Advances in manufacturing techniques, e.g., lithography [8, 9, 10] and seeded growth processes [11, 12], have allowed experimentalists to produce a wide range of nanoscale resonators designed to invoke specific EM responses. This has led to novel functionalities such as perfect absorption [13] and optical magnetism [14]; with applications ranging from cloaking [15, 16, 17] to perfect lenses [18, 19, 20]. These advanced manufacturing methods, together with the diversity of applications, has resulted in metamaterials becoming a burgeoning field for experimentalists attempting to realize functioning devices and theorists to explain the complex interactions of the resonators.

1.1.3 Planar metamaterials

Though there have been great advances in manufacturing methods, fabricating 3-dimensional materials remains extremely difficult [21]. In planar metamaterial arrays, all the resonators are in one plane, comprising either a single layer or a small number of 'stacked' layers. These planar arrays are much more readily fabricated than 3-dimensional materials. Because of the 2-dimensional nature of the planar arrays, the propagation phase shift of the EM field is small, consequently the metamaterial's bulk properties such as permittivity and permeability are not always the primary focus for researchers. Even so, there is still active theoretical research deriving macroscopic material parameters from single nanoscale resonators [22, 23].

A different approach to modeling the metamaterial is to study the light-matter interactions of the resonators. This is because the scattering of light from the resonators (sometimes referred to as 'optical antennas') in planar arrays have the ability to produce strong interactions. These strong interactions cause changes in the array's optical properties such as scattering amplitude and phase shift. The resonance of these properties often occur at wavelengths similar to that of the incident light [24], i.e., much larger than the resonators or their separations, thus are much more readily accessible to experimentalists.

In planar metamaterials, it is not only the electric field that couples to the resonators, the magnetic field can also couple [25, 26]. This allows the impedance of the material to be matched with that of free space, thereby creating high energy transmit arrays with little to no reflection. In Reference 26, a material simulation comprising three stacked planar arrays with subwavelength plasmonic and dielectric components demonstrated a beam deflector and flat lens with high transmission. The nano resonators acted as inductors and capacitors at optical frequencies, precisely in the regime that we study in this thesis.

In addition to the response of each resonator to the incident EM field, resonators also respond to the scattered EM fields from other resonators. This coupling between resonators results in different eigenmodes of response that may exhibit decay rates that are much stronger (superradiant) or weaker (subradiant) than the decay rates of the individual resonators. Under prescribed conditions, these response eigenmodes can destructively interfere and manifest as Fano resonances in the transmitted field [27, 28, 29]. Typically, Fano resonances have a narrow linewidth resonance making them useful in

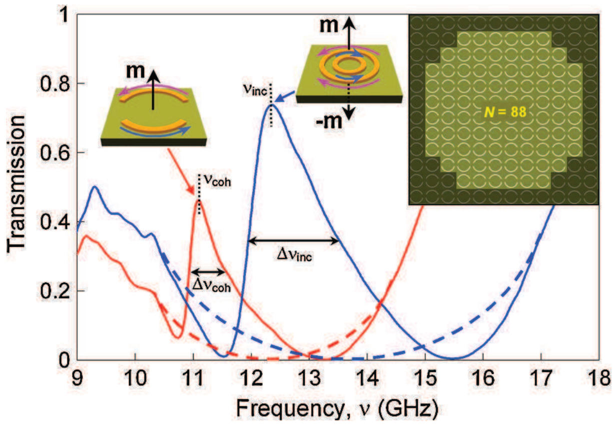

Figure 1.1: Fedotov et. al.'s planar array design showing the transmission spectrum for the ASRR array and concentric ring array. The metamolecule designs and 88 metamolecule array are shown as insets [32].

applications such as plasmonic rulers [30] which rely on the line shift occurring when two plasmonic nanoparticles approach each other, and biosensors [31] which rely on the detection of surface plasmon resonances.

In Reference 32, Fedetov et. al., conducted an experiment on two different planar arrays, each showed a Fano resonance in the transmission spectrum. The demonstration of this collective line collapse is fundamental for lasing spacers which are fueled by coherent plasmonic oscillations. One planar material comprised a regular array of 88 antisymmetric split ring resonators (ASRRs), the second comprised a regular array of 88 pairs of concentric rings, see Figure 1.1. Both planar materials were illuminated with an EM field in the microwave regime normal to the plane. The individual metamolecules (two paired ASRRs and two concentric rings) show antisymmetric current oscillations corresponding to magnetic dipole modes perpendicular to the planar array that could not couple to the illuminating magnetic field [33]. The concentric rings' magnetic dipole moments canceled each other out because the inner and outer ring have antisymmetric oscillations, hence dipole moments in opposite directions, and the planar array showed only a weak total magnetic dipole moment. The ASRRs' magnetic dipole moment was reinforced by each arc. This resulted in strong interactions between the different ASRRs and a coherent strong magnetic dipole response from the array.

Designing material structures to support Fano resonances at predetermined frequencies is difficult. Not least due to the complex interactions of different modes that result in the Fano resonance; but variations in the resonators comprising the material can affect the line shifts and widths of the interacting modes also. Nanorods (rods whose lengths are at most a few hundred nanometers long) can be consistently manufactured [34], making them an attractive choice of resonator, and have been shown to support metamaterial properties normally associated with more complex shaped resonators [35]. Also, along their longitudinal axis they are easily tunable, allowing one to more easily control the dipole-like interactions by varying the length of the nanorod in addition to controlling the inter-rod separations. Metamolecules can be easily formed from nanorods, yet another reason researchers are drawn to them. Such structures have been shown by researchers to support Fano resonances resulting from electric and magnetic dipole modes [36, 37]. The Fano resonance is important because we show later how it appears in our metamolecule design.

1.1.4 A brief point electric dipole and long thin rod comparison

Modeling the EM interactions of each resonator in any system is difficult. Strong interactions can also result from the photons repeatedly scattering of the same resonator and these interactions are difficult to account for. Simplifications often treat the array as an infinite lattice [4, 6] and the resonators as point multipole sources [38]. Nanorods are thus an attractive choice of resonator as they can readily be approximated as electric dipoles when the relative separations are large.

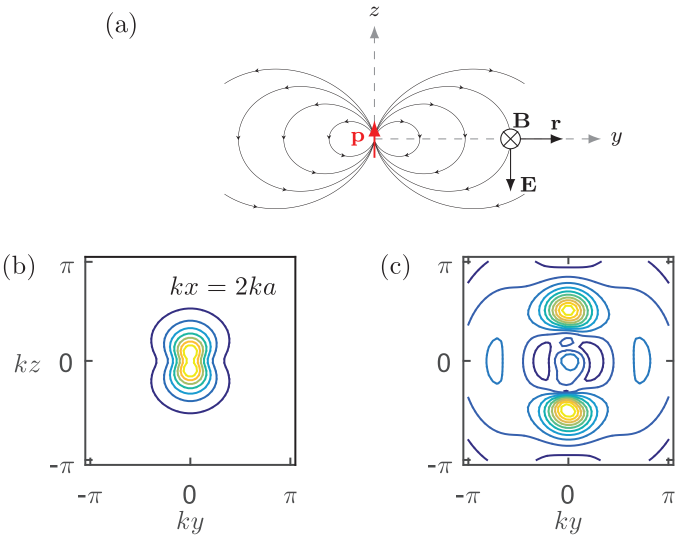

Figure 1.2: The electric field magnitude $|\tilde{\mathbf{E}}| = |\mathbf{E}|/E_0$ in the plane $x = 2a$ from an oscillating point electric dipole and a nanorod with length $H = \lambda/2$ and radius $a = \lambda/20$, where the wavelength $\lambda = 859$ nm. We show: (a) the location and orientation of the point electric dipole moment $\mathbf{p}$ (and center of the nanorod) and the electric $\mathbf{E}$ field direction and propagation vector $\mathbf{r}$ (the magnetic field $\mathbf{B}$ points into the page); (b) the electric field magnitude $|\tilde{\mathbf{E}}|$ of the point electric dipole; and (c) the electric field magnitude $|\tilde{\mathbf{E}}|$ of the nanorod. The factor E_0 is a normalization constant.

When subject to an incident EM field the rod is polarized, resulting in the disc at one end becoming positively charged, and the disc at the opposite end negatively charged. This causes the rod to act like a physical electric dipole.

In Figure 1.2, we show the electric field magnitude $|\mathbf{E}|$ (for a point electric dipole and a nanorod) in the plane $x = 2a$, where a denotes the radius of the nanorod. For a single point electric dipole source at the origin, $|\mathbf{E}|$ is maximum at the dipole location, rapidly falling off as the distance from the dipole increases ($ky > |\pi/2|$), see Figure 1.2(a). The nanorod can be approximated by a collection of atomic electric dipoles distributed throughout the volume of the rod. This causes the near field of the nanorod to behave notably different from that of a point electric dipole; compare, for example, Figure 1.2(b) and (c). For the point electric dipole, the maximum of $|\mathbf{E}|$ is limited to a small area in the center of the plane. For the nanorod, $|\mathbf{E}|$ is distributed over a wider area, in particular at the ends of the nanorod. However, at an observation point opposite the center of the nanorod, $|\mathbf{E}|$ is much less than at the ends of the rod and significantly less than the equivalent point of the electric dipole. Even at $ky \simeq |\pi/2|$, there is still a noticeable electric field magnitude for the nanorod, but not for the point electric dipole. Figure 1.2 highlights why one must be careful modeling nanorods as point electric dipoles, particularly when the observation point is close to the source and the near fields dominate.

1.2 Toroidal metamaterials

1.2.1 A brief introduction to the toroidal dipole

The standard literature on electrodynamics, when discussing the EM multipole expansion, deal with electric and magnetic multipoles [39, 40, 41], the dipole terms of which are associated with longitudinal and transverse currents, respectively. In the longwavelength limit, contributions from the radial currents are considered relativistic [40, 42] and omitted from the multipole expansion. However, it is precisely these oscillating radial currents that are responsible for the toroidal dipole [42, 43].

The static toroidal dipole, also known as an anapole, was first considered by Zel'dovich in 1957 [44]. The notion of the toroidal dipole was eventually extended to the dynamic case, where it generated a whole family of radiating toroidal multipoles [42, 43, 45, 46]. The toroidal dipole is produced by currents circulating on the surface of an imaginary torus along its meridians [47], see Figure 1.3.

1.2.2 Metamaterials that exhibit an enhanced toroidal response

In natural materials, the toroidal response is weak and usually masked by conventional EM effects. Recently, however, materials that exhibit an enhanced toroidal response, toroidal metamaterials, have generated much interest due to predicted backward waves

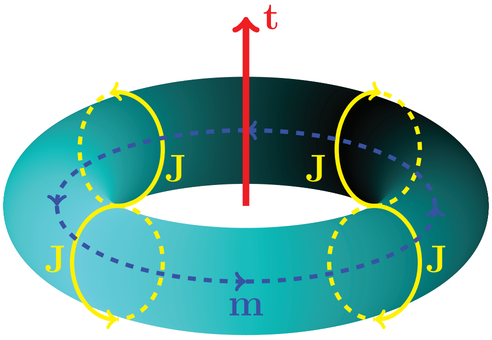

Figure 1.3: A toroidal dipole moment **t** (red) is formed from the poloidal currents **J** (yellow) on the surface meridians of a torus. The direction of the magnetic flux is shown in blue.

and negative refractive indices in such systems [48, 49]. The first recorded observation of an isolated toroidal resonance was in 2010 [50], by Kaelberer et. al.

Kaelberer's metamaterial design comprised an array of toroidal unit cells arranged to form a metamaterial slab, see Figure 1.4. The slab itself is approximately $\lambda/10$, where λ is the wavelength of the incident light in the microwave regime. Each unit cell comprised four split ring (wire) resonators (SRRs) embedded in a dielectric slab. The rings are arranged as diametrically opposite pairs about a common inversion center C. Each pair can be rotated into the position of the other pair through a rotation of $\pi/2$ about C. The SRRs form effective current loops on the surface of an imaginary torus. For example, compare the current loops in Figure 1.3 and the SRRs in Figure 1.4(a). The splits in each of the SRRs are identical, however, within each diametrically opposite pair, one SRR has the slit on the top, the other on the bottom. Their slab is formed by translating the unit cells along the y and z axes.

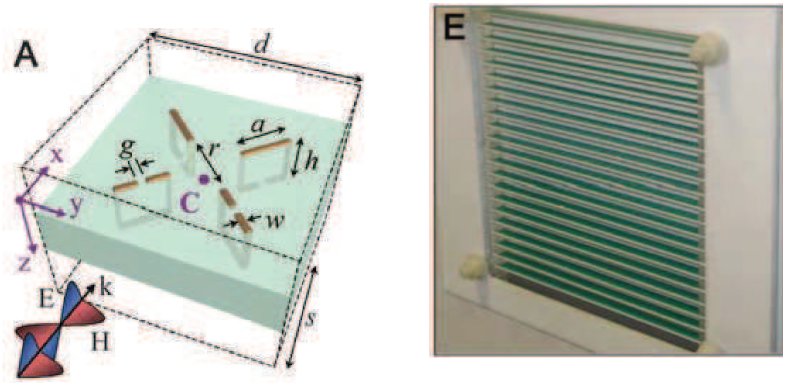
(a) (b)

Figure 1.4: Kaelberer et. al.'s design for a toroidal metamaterial slab [50]. In (a) we show the unit cell toroidal molecule, in (b) the 8 × 176 × 165 mm metamaterial slab.

To model the EM interactions, Kaelberer et. al., initially employed a three dimensional (finite element method) Maxwell's equation solver, with a driving EM field comprising linearly polarized light in the range 14.5–17.0 GHz (microwave) incident on the molecule. The scattered multipole powers were calculated from the densities of the induced electrical currents. Two resonance frequencies were identified at approximately: 16.1 GHz; and 15.4 GHz. At the former, the magnetic dipole moment radiated much more strongly than other electric or toroidal moments, and manifests as a peak in reflection and dip in transmission. At the latter, reflection peaks and transmission dips were also identified. However, here electric and magnetic multipole moments were not resonant and the quality factor was high. The resonance was attributed to the toroidal dipole moment which scattered more strongly than the other multipole moments. The high quality factor is attributed to the weak free space coupling of the toroidal dipole mode and its strong confinement.

Kaelberer et. al.'s simulation results were supported experimentally with a 22×22 array of toroidal unit cells. Transmission and reflection properties of the slab were measured and provided good agreement with the simulations. Where they found small discrepancies in resonance frequencies, these were readily attributed to small discrepancies in manufacturing. Both the simulation and experimental results provide credible evidence of resonant responses only attributable to toroidal dipole excitations.

Various metamaterial designs have since been utilized experimentally to promote a toroidal dipole response in the microwave and optical part of the spectrum: circular apertures in a metallic screen [51]; asymmetric split rings[52]; split rings [50, 53]; and double bars [54]. In numerical simulations, other resonator configurations [55, 56, 57, 58, 59] have also shown notable toroidal dipole responses. Each design comprises diametrically opposite effective current loops about a common inversion center. It is this inversion center that gives the metamolecule its toroidal response rather than other more symmetric responses.

1.2.3 Motivation for further study of toroidal metamaterials

Thus far, the theoretical understanding of the toroidal dipole response in resonator systems has been limited and the conditions under which the toroidal moment may be excited on the microscopic level have not been well known. In this thesis, we show theoretically how a simple structure formed by interacting subwavelength nanorods can support a collective excitation eigenmode that corresponds to a radiating toroidal moment. We show how the nanorods may be approximated as point electric dipole sources in the first instance and later accounting for the geometry of the resonators. We will study the transmission resonance of the toroidal dipole mode, and show that the mode is subradiant which could be important, e.g., for the applications of the toroidal moments in nonlinear optics [60, 61] and in surface plasmon sensors [62].

1.3 Electromagnetism for metamaterials

Maxwell's equations provide the fundamental laws of electromagnetism which all EM fields must satisfy. They are derived in many text books, see, e.g., References 39, 63, 64. Here, we provide the briefest of introductions, without any formal derivations, to Maxwell's equations and the other equations that relate the electromagnetic properties of materials to electromagnetic fields. In their macroscopic form, Maxwell's equations relate the: electric displacement **D**; magnetic flux **B**; electric field **E**; and magnetic field **H**, to the free charge and current densities, ρ_f and $\mathbf{J}_\mathrm{f}$, respectively. Maxwell's macroscopic equations of electromagnetism allow the rapidly varying microscopic fields to be averaged over distances larger than the structure of the material. This averaging allows the fundamental interactions between the charged particles and the EM fields to be neglected. In SI units, Maxwell's macroscopic equations are [39]:

$$\nabla\cdot \mathbf{D} = \rho_\mathrm{f}\,, \tag{1.1}$$

$$\nabla\cdot \mathbf{B} = 0\,, \tag{1.2}$$

$$\nabla\times \mathbf{E} = -\frac{\partial \mathbf{B}}{\partial t}\,, \tag{1.3}$$

$$\nabla\times \mathbf{H} = \mathbf{J}_\mathrm{f} + \frac{\partial \mathbf{D}}{\partial t}\,. \tag{1.4}$$

Equation (1.1), is Gauss's law and states that the free electric charge is the source of the electric displacement **D**. The equivalent law for magnetism, equation (1.2) states that there are no magnetic monopoles contributing to the magnetic flux. Maxwell-Faraday's equation, equation (1.3), states that a changing magnetic flux induces a rotating electric field **E**. Finally, Ampere's law, with Maxwell's correction, states that a changing electric displacement field induces a rotating magnetic **H** field. In the static limit, Ampere's law says that a rotating magnetic field is equal to the free current density enclosed by the current loop.

In addition to the free charge and current densities $(\rho_\mathrm{f}, \mathbf{J}_\mathrm{f})$, there are also bound charge and current densities $(\rho, \mathbf{J})$. The total charge and current $(\rho_\mathrm{tot},\ \mathbf{J}_\mathrm{tot})$ comprises both the free and bound densities [39]

$$\rho_\mathrm{tot} = \rho_\mathrm{f} + \rho\,, \tag{1.5}$$

$$\mathbf{J}_\mathrm{tot} = \mathbf{J}_\mathrm{f} + \mathbf{J}\,. \tag{1.6}$$

The bound charge and current densities, through conservation of charge, are linked via the continuity equation [39]

$$\nabla\cdot \mathbf{J} + \frac{\partial \rho}{\partial t} = 0\,. \tag{1.7}$$

Auxiliary equations further relate the electric displacement and magnetic field to the electric field and magnetic induction via the polarization density **P** and magnetization density $\mathbf{M}$ [39],

$$\mathbf{D} = \epsilon_0 \mathbf{E} + \mathbf{P}\,, \tag{1.8}$$

$$\mathbf{H} = \frac{1}{\mu_0}\mathbf{B} - \mathbf{M}\,. \tag{1.9}$$

Here, the quantities ϵ_0 and μ_0 are the permittivity and permeability, respectively, of free space. The densities $\mathbf{P}$ and $\mathbf{M}$ are measures of electric and magnetic dipole moments, respectively, aligning along the direction of the field.

1.3.1 Point multipole sources

The solutions to Maxwell's equations depend on the source material and its charge and current configuration. For all but the simplest of sources, these solutions are complicated at best and most often insoluble. An approximate solution is based on the electromagnetic multipole expansion, which allows the EM fields to be analyzed using moments of increasing complexity. Because the lower order multipoles dominate the expansion, the detailed structure of the resonator can be ignored.

In the majority of classical texts [39, 40, 65] treating the EM multipole expansion, the treatment is limited to the electric and magnetic multipole moments. Inconsistencies that appear in the expansions are often considered relativistic or due to retardation [39, 66]. The resulting electric $\mathbf{p}$ and magnetic $\mathbf{m}$ dipole moments at $\mathbf{r}$ from charge (ρ) and current ($\mathbf{J}$) densities, respectively, at $\mathbf{r}'$ are,

$$\mathbf{p}(\mathbf{r}) = \int \mathrm{d}^3 r'\, \mathbf{r}' \rho(\mathbf{r}')\,, \tag{1.10}$$

$$\mathbf{m}(\mathbf{r}) = \frac{1}{2}\int \mathrm{d}^3 r'\, \left[\mathbf{r}' \times \mathbf{J}(\mathbf{r}')\right]. \tag{1.11}$$

Both $\mathbf{p}$ and $\mathbf{m}$ are well known, however, to fully parametrize the EM field the toroidal multipole class is also required [42, 43, 45, 46]. The toroidal dipole moment $\mathbf{t}$ is defined as [43]

$$\mathbf{t}(\mathbf{r}) = \frac{1}{10}\int \mathrm{d}^3 r'\, \left[\mathbf{r}'(\mathbf{r}' \cdot \mathbf{J}(\mathbf{r}') - 2r'^2 \mathbf{J}(\mathbf{r}')\right]. \tag{1.12}$$

All three dipole moments share similar far field radiation patterns [49, 57]. The power, P, radiated through a sphere centered on each of an electric, magnetic and toroidal

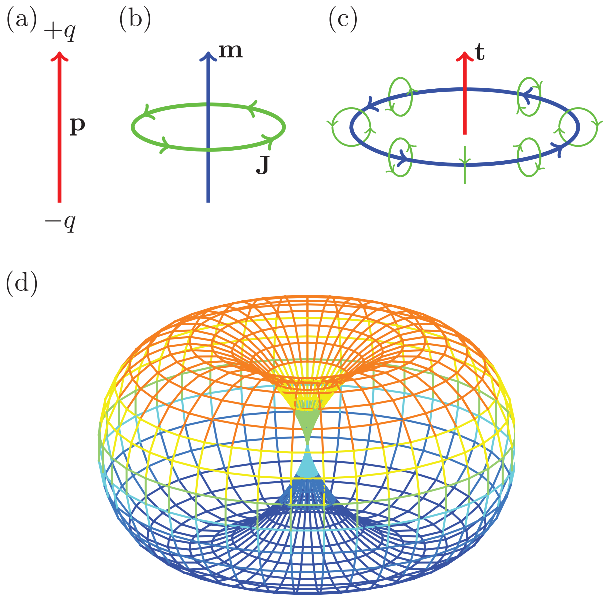

Figure 1.5: Representation of: (a) an electric dipole; (b) a magnetic dipole; and (c) a toroidal dipole. In (d), we show a typical dipole radiation plot for each of the dipole orientation vectors in (a–c).

dipole is [49]

$$P_{\mathrm{E1}} = \frac{\omega^4}{6\pi\epsilon_0 c^3}|\mathbf{p}|^2\left[1-(\hat{\mathbf{r}}\cdot\hat{\mathbf{p}})^2\right], \tag{1.13}$$

$$P_{\mathrm{M1}} = \frac{\omega^4}{6\pi\epsilon_0 c^3}|\mathbf{m}|^2\left[1-(\hat{\mathbf{r}}\cdot\hat{\mathbf{m}})^2\right], \tag{1.14}$$

$$P_{\mathrm{T1}} = \frac{\omega^6}{6\pi\epsilon_0 c^5}|\mathbf{t}|^2\left[1-(\hat{\mathbf{r}}\cdot\hat{\mathbf{t}})^2\right], \tag{1.15}$$

where $\hat{\mathbf{r}}$, $\hat{\mathbf{p}}$, etc, are unit vectors, ω is the resonance frequency and the subscripts 'E1', 'M1', and 'T1', denote the electric, magnetic and toroidal dipole contributions, respectively. What distinguishes each of the radiation patterns are the dipole moments $\mathbf{p}$, $\mathbf{m}$, and $\mathbf{t}$. In Figure 1.5, we show a typical dipole radiation pattern at some location $\mathbf{r}$. When $\hat{\mathbf{r}}$ is in the same direction as the dipole orientation vector there is no radiated power. When $\hat{\mathbf{r}}$ and the dipole orientation vector are perpendicular the radiated power is maximum. Both the electric and magnetic dipole radiated powers depend on ω^4. The toroidal dipole, however, depends on ω^6, more usually associated with electric and magnetic quadrupole radiation.

When we go beyond the dipole approximation, the radiation patterns become increasingly complicated. We show later, in Chapter 3, that an electric quadrupole moment is of the same order of magnitude as the magnetic dipole. We also show that the electric quadrupole is formed by two antisymmetrically excited electric dipoles. The radiation pattern, however, is vastly different from the electric dipole radiation. In Figure 1.6, we show the radiation pattern for two possible electric quadrupole moments. The electric

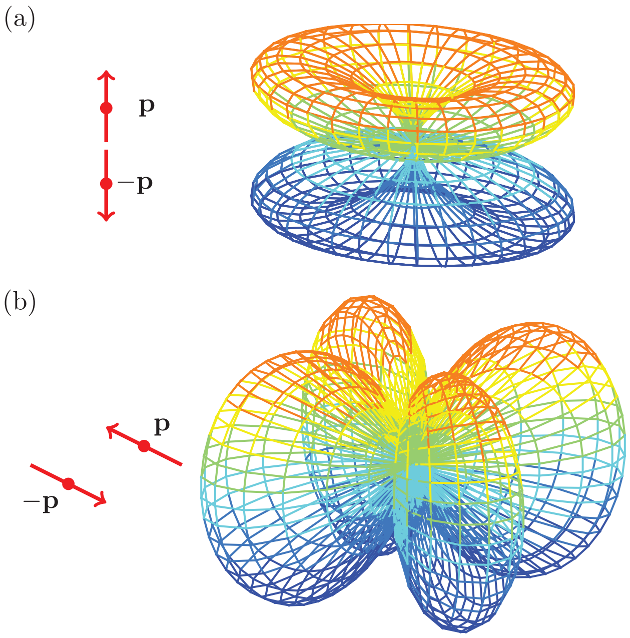

Figure 1.6: Electric quadrupole radiation patterns from two antisymmetric electric dipoles **p**. We show: (a) two axial; and (b) two lateral, antisymmetric electric dipoles.

quadrupole radiation depends on ω^6, the same order of magnitude as the toroidal dipole radiation.

1.4 Introduction to plasmonics

In this introduction we have already touched on the importance of plasmonic resonance. We now elaborate and give a brief introduction to what plasmonics and plasmonic resonances are. At the atomic level, the interior of metals comprise fixed positive nuclei about which a free electron gas is free to move. The interaction between an external EM field and a metal's free electrons is the study of plasmonics. When an EM field is incident on a metallic particle (plasmonic resonator), the optical energy couples with the EM waves propagating along the resonator's surface. The electric component of the incident field interacts with the free charges within the resonator, causing them to oscillate. The combined surface waves and charge oscillations are referred to as surface plasmons [67]. The resonance frequency (or frequencies) of these charge oscillations depends on the geometry of the resonator [68, 69]. Nanospheres, for example, have a single resonance frequency. Nanorods and nanowires, however, have distinct resonance frequencies associated with scattering along the longitudinal axis and the transverse axis [70]. The resonance frequency can also be influenced by the resonator size and its surrounding media [68, 71, 72, 73].

The polarization and magnetization of a material are closely linked to the material's permittivity ϵ and permeability μ. In most materials $\mu \simeq \mu_0$. However, ϵ depends strongly on the frequency of the incident field. The relative permittivity (ϵ_r) for noble metals such as gold and silver, is often modeled using the free electron Drude-Somerfield model [35, 62, 74, 75]. The Drude model is particularly useful in determining such properties of a particle as its scattering and absorption cross sections. We utilize the scattering cross section of cylindrical particles and the Drude model, later in Appendix F, to determine the resonance frequency of gold nanorods. The Drude model we utilize is [62],

$$\epsilon_\mathrm{r} = \frac{\epsilon}{\epsilon_0} = \epsilon_\infty - \frac{\omega_p^2}{\omega(\omega + i\Gamma_\mathrm{D})} \,. \tag{1.16}$$

Here: ϵ_∞ is a dimensionless parameter resulting from a residual polarization at high frequencies (in models that neglect any residual polarization, $\epsilon_\infty = 1$); ω is the frequency of the incident EM field; ω_p is the plasma frequency of the metal, which determines the minimum frequency EM waves will propagate inside the metal; and Γ_D is the relaxation time of the electron collisions.

The parameters ϵ_∞, ω_p, and Γ_D are different for each metal and are empirically obtained. Typical parameters for gold are [76, 77, 78], $\omega_p = (2\pi)2200$ THz, and $\Gamma_\mathrm{D} = (2\pi)17$ THz; and for silver [74, 76, 77], $\omega_p = (2\pi)2176$ THz, and $\Gamma_\mathrm{D} = (2\pi)4.8$ THz. In Figure 1.7, we show the relative permittivity for both gold and silver. When there is no residual polarization, for both gold and silver, at large frequencies the EM field propagates inside the medium with no absorption, and $\epsilon_\mathrm{r} \to 1$, see Figure 1.7(a). At low frequencies, the EM field is reflected and at very low frequencies, absorption occurs. When residual polarization is accounted for ($\epsilon_\infty \neq 1$) at high frequencies $\mathrm{Re}(\epsilon_\mathrm{r}) \simeq \epsilon_\infty$. The frequency at which EM waves propagate inside the medium reduces to: $\omega \approx 750(2\pi)$ THz for silver and $\omega \approx 1000(2\pi)$ THz for gold. Below $\omega = 500(2\pi)$ THz, both gold and silver are absorbing.

1.5 Structure of thesis

In this thesis, we develop a theoretical model to analyze a toroidal metamolecule comprising nanorods. In the first instance, the nanorods are approximated as point electric dipoles. Secondly, we account for the finite-size and geometry of the rods. We reach the analysis of the toroidal metamolecule by firstly introducing the general model describing the EM interactions, then introduce the different interacting resonators in pairs, analyzing each stage in detail.

In Chapter 2, we review the general model for an ensemble of interacting closely spaced resonators, leading to a linear equation of motion for a single dynamic variable. The model is derived in detail in Reference 79. Additionally, we review the point electric

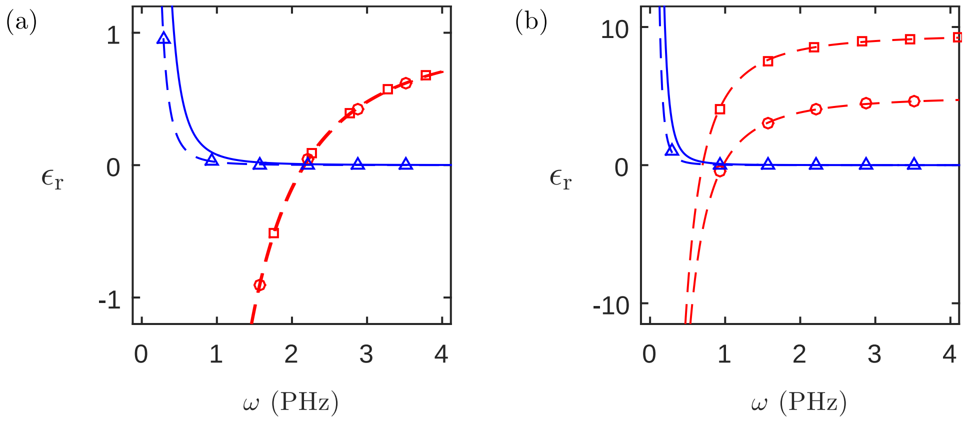

Figure 1.7: The complex valued relative permittivity ϵ_r of gold and silver as a function of frequency ω. In (a) we use the parameter $\epsilon_\infty = 1$, for both gold and silver. In (b) we use $\epsilon_\infty = 9.5$ for gold and $\epsilon_\infty = 5$ for silver. In both (a) and (b), we show: $\mathrm{Im}(\epsilon_r)$ for gold and silver in solid blue and blue dashed-triangle, respectively; and $\mathrm{Re}(\epsilon_r)$ for gold and silver in red dashed-square and red dashed-circle, respectively.

and magnetic dipole approximation of the resonators' scattered EM fields and their interaction with an incident EM field and those scattered by other resonators, also introduced in Reference 79.

Chapter 3 presents original work, whereby the point electric and magnetic dipole approximation is extended to include the electric quadrupole. We obtain an analytical expression for the radiative emission rate of a point electric quadrupole before showing how the point electric quadrupole source interacts with other electric quadrupoles and electric and magnetic dipoles. In Chapter 3.2, we analyze different systems of $N = 2$ point electric dipole emitters and show how a simple parallel pair of point electric dipoles can be approximated by a single resonator with both magnetic dipole and electric quadrupole moments. We then analyze in detail the interactions between $N = 2$ resonators with both magnetic dipole and electric quadrupole moments, and compare them to the equivalent system of $2N$ electric dipole resonators.

In Chapter 4, original work is presented whereby a model to account for the finite-size and geometry of each resonator is introduced. We then compare our finite-size model to the equivalent point multipole approximation of the preceding chapters. The key feature of Chapters 3 and 4 is the analysis of the interacting resonators in the geometry that is used later to model a toroidal dipole metamolecule.

In Chapter 5 we present original work analyzing a toroidal dipole metamaterial. In Chapter 5.2, we first review the EM multipole expansion to show the toroidal dipole moment formulation. In Chapter 5.3, a toroidal metamolecule comprising a finite number of individual plasmonic nanorods is modeled. We do this using the point electric dipole approximation [first introduced in Chapter 2], and the finite-size rod model introduced in Chapter 4. We optimize the toroidal response of a metamolecule and determine the conditions under which the toroidal response may be driven by linearly polarized light.

The thesis conclusions and future direction of studies are included in Chapter 6.

Chapter 2

General electromagnetic interactions in discrete resonator systems

In this thesis, we regard a metamaterial as an array of resonators separated by distances less than the wavelength of the incident light. In this chapter, we introduce the basic formalism used to analyze the interaction of an EM field to closely spaced resonators. The formalism is derived in detail in Reference 79. Here, we review how each of N resonators can be described by a single dynamic variable. This then leads to a linear equation of motion, describing how the polarization and magnetization sources within a resonator interact with the scattered EM field from each of the N resonators and an incident EM field. The general dynamics of the metamaterial system are introduced in Section 2.1. In Section 2.2, we provide an overview of the point electric and magnetic dipole approximation of the scattered EM fields and their interactions with the resonators.

2.1 Dynamics of metamaterial systems

In the general model of circuit resonator interactions with EM fields, we assume that the charge and current sources are initially driven by an incident electric displacement field $\mathbf{D}_{\text{in}}(\mathbf{r}, t)$, and magnetic induction $\mathbf{B}_{\text{in}}(\mathbf{r}, t)$, with frequency Ω_0. The electric $\mathbf{E}_{\text{sc},j}(\mathbf{r}, t)$ and magnetic $\mathbf{H}_{\text{sc},j}(\mathbf{r}, t)$ fields scattered by resonator j, are a result of its oscillating polarization $\mathbf{P}_j(\mathbf{r}, t)$ and magnetization $\mathbf{M}_j(\mathbf{r}, t)$ sources. In general, the electric and magnetic fields are related to the electric displacement and magnetic induction through the auxiliary equations

$$\mathbf{D}(\mathbf{r},t) = \epsilon_0 \mathbf{E}(\mathbf{r},t) + \mathbf{P}(\mathbf{r},t)\,, \tag{2.1}$$

$$\mathbf{H}(\mathbf{r},t) = \frac{1}{\mu_0}\mathbf{B}(\mathbf{r},t) - \mathbf{M}(\mathbf{r},t)\,. \tag{2.2}$$

When analyzing the EM fields and resonators, we adopt the rotating wave approximation where the dynamics is dominated by Ω_0. In the rest of this thesis, all the EM field and resonator amplitudes refer to the slowly-varying versions of the positive frequency components of the corresponding variables, where the rapid oscillations $e^{-i\Omega_0 t}$ due to the dominant laser frequency have been factored out. The scattered EM fields are then given by [79]

$$\mathbf{E}_{\mathrm{sc},j}(\mathbf{r}) = \frac{k^3}{4\pi\epsilon_0}\int \mathrm{d}^3r' \left[\mathbf{G}(\mathbf{r}-\mathbf{r}')\cdot \mathbf{P}_j(\mathbf{r}',t) + \frac{1}{c}\mathbf{G}_\times(\mathbf{r}-\mathbf{r}')\cdot \mathbf{M}_j(\mathbf{r}',t)\right], \tag{2.3}$$

$$\mathbf{H}_{\mathrm{sc},j}(\mathbf{r}) = \frac{k^3}{4\pi}\int \mathrm{d}^3r' \left[\mathbf{G}(\mathbf{r}-\mathbf{r}')\cdot \mathbf{M}_j(\mathbf{r}',t) - c\mathbf{G}_\times(\mathbf{r}-\mathbf{r}')\cdot \mathbf{P}_j(\mathbf{r}',t)\right], \tag{2.4}$$

where $k = \Omega/c$. Explicit expressions for the radiation kernels are [79]

$$\mathbf{G}(\mathbf{r}) = i\left[\frac{2}{3}\mathbf{I}h_0^{(1)}(kr) + \left(\frac{\mathbf{rr}}{r^2} - \frac{\mathbf{I}}{3}\right)h_2^{(1)}(kr)\right] - \frac{4\pi}{3}\mathbf{I}\delta(k\mathbf{r})\,, \tag{2.5}$$

$$\mathbf{G}_\times(\mathbf{r}) = \frac{i}{k}\nabla\times\frac{e^{ikr}}{kr}\mathbf{I}\,. \tag{2.6}$$

Here: the dyadic $\mathbf{rr}$, is the outer product of $\mathbf{r}$ with itself; $\mathbf{I}$ is the identity matrix; and $h_n^{(1)}(x)$ are spherical Hankel functions of the first kind, of order n, defined by

$$h_0^{(1)}(x) = -i\frac{e^{ix}}{x}\,, \tag{2.7}$$

$$h_2^{(1)}(x) = i\left[\frac{1}{x} + i\frac{3}{x^2} - \frac{3}{x^3}\right]e^{ix}\,, \tag{2.8}$$

see Appendix B also. The radiation kernel $\mathbf{G}(\mathbf{r}-\mathbf{r}')$ determines the electric (magnetic) field at $\mathbf{r}$, from polarization (magnetization) sources at $\mathbf{r}'$ [39]. Similarly, the cross kernel $\mathbf{G}_\times(\mathbf{r}-\mathbf{r}')$ determines the electric (magnetic) field at $\mathbf{r}$, from magnetization (polarization) sources at $\mathbf{r}'$ [39]. In the dipole approximation discussed in Section 2.2, equations (2.3) and (2.4) are readily recognized as those of oscillating dipoles [39].

Equations (2.3) and (2.4) give the total scattered EM fields as functions of the polarization and magnetization densities. In general, for sources other than point resonators, the scattered field equations are not readily solved for $\mathbf{P}_j(\mathbf{r},t)$ and $\mathbf{M}_j(\mathbf{r},t)$. When resonators are separated by distances less than, or of the order of a wavelength, a strongly coupled system results.

2.1.1 Interacting resonators

In Reference 79, a general theory was formulated to derive a coupled set of linear equations for the EM fields and strongly coupled resonators. The state of current oscillation in each resonator j is described by a single dynamic variable with units of charge $Q_j(t)$ and its rate of change $I_j(t)$, the current. The current oscillations within the jth resonator behave like an LC circuit with resonance frequency ω_j,

$$\omega_j = \frac{1}{\sqrt{L_j C_j}}\,, \tag{2.9}$$

where C_j and L_j are an effective self-capacitance and self-inductance, respectively. The polarization and magnetization of a resonator can be obtained from $Q_j(t)$ and $I_j(t)$ [79]

$$\mathbf{P}_j(\mathbf{r},t) = Q_j(t)\mathbf{p}_j(\mathbf{r})\,, \tag{2.10}$$

$$\mathbf{M}_j(\mathbf{r},t) = I_j(t)\mathbf{w}_j(\mathbf{r})\,. \tag{2.11}$$

The charge profile function $\mathbf{p}_j(\mathbf{r})$ and the current profile function $\mathbf{w}_j(\mathbf{r})$, in equations (2.10) and (2.11), may be considered independent of time. The geometry of individual resonators determines the form of the respective profile functions. The polarization and magnetization densities are related to the charge and current densities of the resonators by [79]

$$\rho_j(\mathbf{r},t) = -\nabla\cdot \mathbf{P}_j(\mathbf{r},t)\,, \tag{2.12}$$

$$\mathbf{J}_j(\mathbf{r},t) = \frac{\partial}{\partial t}\big[\mathbf{P}_j(\mathbf{r},t)\big] + \nabla\times \mathbf{M}_j(\mathbf{r},t)\,. \tag{2.13}$$

The charge and current densities within each resonator are initially driven by the incident EM fields $\mathbf{D}_{\text{in}}(\mathbf{r},t)$ and $\mathbf{B}_{\text{in}}(\mathbf{r},t)$. The incident electric displacement and magnetic flux, with polarization vector $\hat{\mathbf{e}}_{\text{in}}$, are:

$$\mathbf{D}_{\text{in}}(\mathbf{r}) = D_{\text{in}}\hat{\mathbf{e}}_{\text{in}}e^{i\mathbf{k}_{\text{in}}\cdot\mathbf{r}}\,, \tag{2.14}$$

$$\mathbf{B}_{\text{in}}(\mathbf{r}) = B_{\text{in}}\big[\hat{\mathbf{k}}_{\text{in}}\times\hat{\mathbf{e}}_{\text{in}}\big]e^{i\mathbf{k}_{\text{in}}\cdot\mathbf{r}}\,, \tag{2.15}$$

where $\hat{\mathbf{k}}_{\text{in}}$ is the propagation vector of the incident EM field. The total EM fields external to resonator j [$\mathbf{E}_{\text{ext},j}(\mathbf{r})$ and $\mathbf{H}_{\text{ext},j}(\mathbf{r})$] comprise the incident field and those fields scattered from all other resonators,

$$\mathbf{E}_{\text{ext},j}(\mathbf{r}) = \frac{1}{\epsilon_0}\mathbf{D}_{\text{in}}(\mathbf{r}) + \sum_{i\neq j}\mathbf{E}_{\text{sc},i}(\mathbf{r})\,, \tag{2.16}$$

$$\mathbf{H}_{\text{ext},j}(\mathbf{r}) = \frac{1}{\mu_0}\mathbf{B}_{\text{in}}(\mathbf{r}) + \sum_{i\neq j}\mathbf{H}_{\text{sc},i}(\mathbf{r})\,. \tag{2.17}$$

The total driving of the charge and current oscillations within the resonator is provided by the external EM fields, equations (2.16) and (2.17), aligned along the direction of the source [79], providing a net electromagnetic force (emf), $\mathcal{E}_{\mathrm{ext},j}$ and flux, $\Phi_{\mathrm{ext},j}$. We define the external emf and flux as [79]

$$\mathcal{E}_{\mathrm{ext},j} = \frac{1}{\sqrt{\omega_j L_j}} \int \mathrm{d}^3 r\, \mathbf{p}_j(\mathbf{r})\cdot \mathbf{E}_{\mathrm{ext},j}(\mathbf{r})\,, \tag{2.18}$$

$$\Phi_{\mathrm{ext},j} = \frac{\mu_0}{\sqrt{\omega_j L_j}} \int \mathrm{d}^3 r\, \mathbf{w}_j(\mathbf{r})\cdot \mathbf{H}_{\mathrm{ext},j}(\mathbf{r})\,. \tag{2.19}$$

The emf and flux can be decomposed into contributions from the incident and scattered EM fields,

$$\mathcal{E}_{\mathrm{ext},j} \quad = \quad \mathcal{E}_{\mathrm{in},j} + \sum_{i\neq j} \mathcal{E}^{\mathrm{sc}}_{i,j}\,, \tag{2.20}$$

$$\Phi_{\mathrm{ext},j} \quad = \quad \Phi_{\mathrm{in},j} + \sum_{i\neq j} \Phi^{\mathrm{sc}}_{i,j}\,. \tag{2.21}$$

Here: the emf and flux resulting from the driving by the incident EM field is $\mathcal{E}_{\mathrm{in},j}$ and $\Phi_{\mathrm{in},j}$, respectively; and the driving of resonator j by the scattered EM fields from resonator i are the emf $\mathcal{E}^{\mathrm{sc}}_{i,j}$ and flux $\Phi^{\mathrm{sc}}_{i,j}$. The total driving of a resonator can be summarized by the external driving $F_{\mathrm{ext},j}$, the sum of the incident $F_{\mathrm{in},j}$ and the scattered $F_{\mathrm{sc},j}$ driving contributions, respectively, where [79]

$$F_{\mathrm{ext},j} = F_{\mathrm{in},} + F_{\mathrm{sc},j} = F_{\mathrm{in},j} + \sum_{i\neq j} \mathcal{C}_{ij}\,, \tag{2.22}$$

where the components

$$F_{\mathrm{in},j} = \frac{i}{\sqrt{2}}\left[\mathcal{E}_{\mathrm{in},j} + i\omega_j \Phi_{\mathrm{in},j}\right], \tag{2.23}$$

$$\left[\mathcal{C}\right]_{i\neq j} = \frac{i}{\sqrt{2}} \sum_{i\neq j} \left[\mathcal{E}^{\mathrm{sc}}_{i,j} + i\omega_j \Phi^{\mathrm{sc}}_{i,j}\right]. \tag{2.24}$$

2.1.2 Normal modes

In order to express the coupled equations for the EM fields and resonators we introduce the slowly varying normal mode oscillator amplitudes [79] $b_j(t)$,

$$b_j(t) = \frac{1}{\sqrt{2\omega_j}} \left[\frac{Q_j(t)}{\sqrt{C_j}} + i\frac{\phi_j(t)}{\sqrt{L_j}}\right]. \tag{2.25}$$

Here, the generalized coordinate for the current excitation in the resonator j is the charge $Q_j(t)$ and $\phi_j(t)$ represents its conjugate momentum. In the rotating wave approximation, the conjugate momentum is linearly proportional to the current [79]. The dynamic variable in equation (2.25) can be used to describe a general resonator with both polarization and magnetization sources.

The normal mode amplitudes $b_j(t)$ describe the current oscillations of the resonator. These current oscillations are subject to radiative damping due to their own emitted radiation. The driving of $b_j(t)$ is achieved through the external fields and resulting emf and flux. The equations of motion for Q and ϕ, $\dot{Q}$ and $\dot{\phi} = \mathcal{E}$, together with the scattered fields from other resonators result in a linear system of equations for $b_j(t)$. For a system which comprises N resonators, these read as [79]

$$\dot{\mathbf{b}} = \mathcal{C}\mathbf{b} + \mathbf{F}_{\text{in}}\,, \tag{2.26}$$

where $\mathbf{b}$ is a column vector of N normal oscillator variables

$$\mathbf{b} = \begin{bmatrix} b_1 \\ b_2 \\ \vdots \\ b_N \end{bmatrix}\,, \tag{2.27}$$

$\dot{\mathbf{b}}$ its rate of change, and $\mathbf{F}_{\text{in}}$ is a column vector formed by equation (2.23). The matrix $\mathcal{C}$ describes the interactions between the resonator's self-generated EM fields (diagonal elements) and those scattered fields from different resonators [off-diagonal elements; the interaction terms in equation (2.24)] [79].

As we show in Section 2.2, and later in Chapters 3 and 4, the solutions to equation (2.24) become increasingly complicated and difficult to solve as the complexity of even simple resonators increases. The diagonal elements of $\mathcal{C}$ contain the resonance frequency shift and total decay rate Γ_j [79],

$$\left[\mathcal{C}\right]_{j,j} = -i(\omega_j - \Omega_0) - \frac{\Gamma_j}{2}\,. \tag{2.28}$$

The total decay rate Γ is a superposition of the resonator's radiative emission rate and ohmic losses. Although generally the emitters can have different resonance frequencies, in this chapter, for simplicity we focus on the case of equal frequencies, i.e., $\omega_j = \omega_0$, for all j. Later, in Chapter 5, where we explain how we account for the difference in resonance frequency and decay rate between resonators

2.1.3 Collective eigenmodes

In the present section, we introduce the eigenmode analysis of a general N resonator system when the EM scattered fields from the polarization and magnetization densities of the resonators are known.

The incident EM field driving the charge and current oscillations is tuned to the resonance frequency ω_0, i.e., $\Omega_0 = \omega_0$. Each resonator scatters light due to its polarization and magnetization densities that result from the charge and current oscillations, respectively. The light can multiply scatter between different resonators as well as causing recurrent scattering. Strong multiple scattering results in collective excitation modes of the system. The collective modes of current oscillation within the system are described by the eigenvectors $\mathbf{v}_n$ of the interaction matrix $\mathcal{C}$. The corresponding eigenvalues ξ_n have real and imaginary parts, corresponding to the decay rate and resonance frequency shift of the mode,

$$\xi_n = -\frac{\gamma_n}{2} - i(\Omega_n - \Omega_0)\,. \tag{2.29}$$

The number of resonators N, determines the number of collective modes. The collective eigenmodes can then exhibit different resonance frequencies and linewidths and line shifts [79, 80, 81, 82]. The different modes may have superradiant or subradiant characteristics. The former occurs when the emitted radiation is enhanced by the interactions of the resonators ($\gamma_n > \Gamma$). The latter occurs when the radiation is suppressed and confined to the metamaterial ($\gamma_n < \Gamma$).

2.2 Point electric and magnetic dipole approximation

The general model of interacting resonators summarized above and introduced formally in Reference 79, is applicable to any type of circuit element resonators. In practice, however, the EM scattered fields are not readily solved for $\mathbf{P}_j(\mathbf{r}, t)$ and $\mathbf{M}_j(\mathbf{r}, t)$, and some approximations to the intrinsic structure of the resonators is required. When the size of the resonator is much less than the wavelength λ_0 (of the incident EM field), the resonators' scattered EM fields are often approximated as those of point multipole sources. For split ring resonators, the scattered EM fields are dominated by electric and magnetic dipole radiation. This motivated the formal theory of the point electric and magnetic dipole approximation, introduced Reference 79, which we review in this section. Later, in Chapter 3, we introduce an electric quadrupole approximation and in Chapter 4, we account for the finite-size of the resonators. These extension to the formalism allow one to model more general resonator and emitter systems.

2.2.1 Radiating point dipoles

The electric $\mathbf{E}_{\mathrm{sc},j}(\mathbf{r})$ and magnetic $\mathbf{H}_{\mathrm{sc},j}(\mathbf{r})$ fields scattered from the jth resonator located at $\mathbf{r}'$ due to its polarization and magnetization sources follow from equations (2.3) and (2.4) with the polarization density equation (2.10) and magnetization density equation (2.11),

$$\mathbf{E}_{\mathrm{sc},j}(\mathbf{r}) = \frac{Q_j k^3}{4\pi\epsilon_0}\int \mathrm{d}^3r'\,\mathbf{G}(\mathbf{r}-\mathbf{r}')\cdot\mathbf{p}_j(\mathbf{r}') + \frac{I_j k^3}{4\pi\epsilon_0 c}\int \mathrm{d}^3r'\,\mathbf{G}_\times(\mathbf{r}-\mathbf{r}')\cdot\mathbf{w}_j(\mathbf{r}')\,, \tag{2.30}$$

$$\mathbf{H}_{\mathrm{sc},j}(\mathbf{r}) = \frac{I_j k^3}{4\pi}\int \mathrm{d}^3r'\,\mathbf{G}_\times(\mathbf{r}-\mathbf{r}')\cdot\mathbf{w}_j(\mathbf{r}') - \frac{Q_j c k^3}{4\pi}\int \mathrm{d}^3r'\,\mathbf{G}_\times(\mathbf{r}-\mathbf{r}')\cdot\mathbf{p}_j(\mathbf{r}')\,. \tag{2.31}$$

In the electric and magnetic dipole approximation, the mode functions, $\mathbf{p}_j(\mathbf{r}) = \mathbf{p}_j^{\mathrm{d}}(\mathbf{r})$ and $\mathbf{w}_j(\mathbf{r})$, respectively, are defined as [79]

$$\mathbf{p}_j^{\mathrm{d}}(\mathbf{r}) = H_j\hat{\mathbf{d}}_j\delta(\mathbf{r}-\mathbf{r}_j)\,, \tag{2.32}$$

$$\mathbf{w}_j(\mathbf{r}) = A_{\mathrm{M},j}\hat{\mathbf{m}}_j\delta(\mathbf{r}-\mathbf{r}_j)\,. \tag{2.33}$$

Here, the proportionality constant H_j has units of length and the unit vector $\hat{\mathbf{d}}_j$ indicates the orientation of the electric dipole, whilst $A_{\mathrm{M},j}$ has units of area and $\hat{\mathbf{m}}_j$ indicates the orientation of the magnetic dipole. The radiation kernels $\mathbf{G}(\mathbf{r})$ and $\mathbf{G}_\times(\mathbf{r})$, in equations (2.30) and (2.31), act directly on the dipole moments, equations (2.32) and (2.33). The interaction of the resonator with its self-generated EM fields causes radiative damping to occur. When contributions from the radiation cross kernel $\mathbf{G}_\times(\mathbf{r})$ are ignored, the lowest order contributions from the radiation kernel $\mathbf{G}(\mathbf{r})$ provide the expression for dipole radiation. The radiation rates of the electric and magnetic dipoles of the jth resonator are $\Gamma_{\mathrm{E1},j}$ and $\Gamma_{\mathrm{M1},j}$, respectively, where [79]

$$\Gamma_{\mathrm{E1},j} = \frac{C_j H_j^2\omega_j^4}{6\pi\epsilon_0 c^3}\,, \tag{2.34}$$

$$\Gamma_{\mathrm{M1},j} = \frac{\mu_0 A_{\mathrm{M},j}^2\omega_j^4}{6\pi L_j c^3}\,. \tag{2.35}$$

We account for nonradiative losses by adding the phenomenological decay rate $\Gamma_{\mathrm{O},j}$. For simple gold or silver resonators, $\Gamma_{\mathrm{O},j}$ can be estimated by applying the Drude model of permittivity with specific material parameters to the scattered cross section of the resonators, see e.g., Appendix F. The total decay rate is then the sum of the radiative emission rate and ohmic losses. In the dipole approximation the total decay rate Γ_j is [79]

$$\Gamma_j = \Gamma_{\mathrm{E1},j} + \Gamma_{\mathrm{M1},j} + \Gamma_{\mathrm{O},j}\,. \tag{2.36}$$

The amplitudes of the EM fields scattered by the electric and magnetic dipoles are proportional to their corresponding radiative emission rates $\Gamma_{\mathrm{E1},j}$ and $\Gamma_{\mathrm{M1},j}$. We write the EM fields due to the point electric and magnetic dipole sources as [79]

$$\mathbf{E}_{\mathrm{sc},j}(\mathbf{r}) = b_j \frac{3}{2}\sqrt{\frac{k^3}{12\pi\epsilon_0}}\left[\sqrt{\Gamma_{\mathrm{E1},j}}\mathbf{G}(\mathbf{r}-\mathbf{r}_j)\cdot\hat{\mathbf{d}}_j - i\sqrt{\Gamma_{\mathrm{M1},j}}\mathbf{G}_\times(\mathbf{r}-\mathbf{r}_j)\cdot\hat{\mathbf{m}}_j\right], \tag{2.37}$$

$$\mathbf{H}_{\mathrm{sc},j}(\mathbf{r}) = -ib_j \frac{3}{2}\sqrt{\frac{k^3}{12\pi\mu_0}}\left[\sqrt{\Gamma_{\mathrm{M1},j}}\mathbf{G}(\mathbf{r}-\mathbf{r}_j)\cdot\hat{\mathbf{m}}_j - i\sqrt{\Gamma_{\mathrm{E1},j}}\mathbf{G}_\times(\mathbf{r}-\mathbf{r}_j)\cdot\hat{\mathbf{d}}_j\right]. \tag{2.38}$$

2.2.2 Interacting point dipoles

The incident EM field, equations (2.14) and (2.15), driving the charge oscillations within a resonator resulting in the emf $\mathcal{E}^{\mathrm{E1}}_{\mathrm{in},j}$ and flux $\Phi^{\mathrm{M1}}_{\mathrm{in},j}$, follow from equations (2.18) and (2.19) [79]:

$$\mathcal{E}^{\mathrm{E1}}_{\mathrm{in},j} = \frac{1}{\epsilon_0\sqrt{\omega_j L_j}}\int \mathrm{d}^3r\, \mathbf{p}^{\mathrm{d}}_j(\mathbf{r})\cdot\mathbf{D}_{\mathrm{in}}(\mathbf{r},t)\,, \tag{2.39}$$

$$\Phi^{\mathrm{M1}}_{\mathrm{in},j} = \frac{1}{\sqrt{\omega_j L_j}}\int \mathrm{d}^3r\, \mathbf{w}_j(\mathbf{r})\cdot\mathbf{B}_{\mathrm{in}}(\mathbf{r},t)\,. \tag{2.40}$$

The scattered electric field from the jth resonator driving the polarization source oscillations within resonator $i \neq j$, result in the emf [79] $\mathcal{E}^{\mathrm{sc,E1}}_{i,j}$

$$\mathcal{E}^{\mathrm{sc,E1}}_{i\neq j} = \sqrt{\Gamma_{\mathrm{E1},i}\Gamma_{\mathrm{E1},j}}\,[\mathcal{G}_{\mathrm{E1}}]_{i\neq j}\frac{b_j}{\sqrt{2}}\,. \tag{2.41}$$

The matrix $\mathcal{G}_{\mathrm{E1}}$ determines how the geometrical properties and orientations of the resonators influence the scattered electric field contributions to the emf. The diagonal elements of $\mathcal{G}_{\mathrm{E1}}$ are zero, the off-diagonal elements, with point electric dipole sources, are

$$[\mathcal{G}_{\mathrm{E1}}]_{i\neq j} = \frac{3}{2}\hat{\mathbf{d}}_i\cdot\mathbf{G}(\mathbf{r}_i-\mathbf{r}_j)\cdot\hat{\mathbf{d}}_j\,. \tag{2.42}$$

In a similar manner, the scattered magnetic field from the jth resonator driving the magnetization source oscillations within resonator $i \neq j$, results in the flux [79] $\Phi^{\mathrm{sc,M1}}_{i,j}$, where

$$\Phi^{\mathrm{sc,M1}}_{i\neq j} = \frac{i}{\omega_j}\sqrt{\Gamma_{\mathrm{M1},i}\Gamma_{\mathrm{M1},j}}\,[\mathcal{G}_{\mathrm{M1}}]_{i\neq j}\frac{b_j}{\sqrt{2}}\,. \tag{2.43}$$

The matrix $\mathcal{G}_{\mathrm{M1}}$ is the magnetic counterpart of equation (2.42). The diagonal elements of $\mathcal{G}_{\mathrm{M1}}$ are zero, the off-diagonal elements, for point magnetic dipole sources, are

$$[\mathcal{G}_{\mathrm{M1}}]_{i\neq j} = \frac{3}{2}\hat{\mathbf{m}}_i\cdot\mathbf{G}(\mathbf{r}_i-\mathbf{r}_j)\cdot\hat{\mathbf{m}}_j\,. \tag{2.44}$$

The driving of the polarization (magnetization) sources within the jth resonator by the magnetic (electric) field scattered by resonator i result in additional contributions to the emf and flux. We call this type of driving "cross driving". In the dipole approximation the cross driving contributions to the emf and flux are [79], $\mathcal{E}^{\mathrm{sc,X1}}_{i\neq j}$ and $\Phi^{\mathrm{sc,X1}}_{i\neq j}$, respectively, where

$$\mathcal{E}^{\mathrm{sc,X1}}_{i\neq j} = -i\sqrt{\Gamma_{\mathrm{E1},i}\Gamma_{\mathrm{M1},j}}\,[\mathcal{G}_{\mathrm{X1}}]_{i\neq j}\,\frac{b_j}{\sqrt{2}}, \tag{2.45}$$

$$\Phi^{\mathrm{sc,X1}}_{i\neq j} = -\frac{1}{\omega_j}\sqrt{\Gamma_{\mathrm{M1},i}\Gamma_{\mathrm{E1},j}}\,[\mathcal{G}_{\mathrm{X1}}]^T_{i\neq j}\,\frac{b_j}{\sqrt{2}}. \tag{2.46}$$

The matrix, $\mathcal{G}_{\mathrm{X1}}$, and its transpose, $\mathcal{G}^T_{\mathrm{X1}}$, are the cross driving counterparts of equations (2.42) and (2.44), the off-diagonal elements are

$$[\mathcal{G}_{\mathrm{X1}}]_{i\neq j} = \frac{3}{2}\hat{\mathbf{m}}_i\cdot\mathbf{G}_\times(\mathbf{r}_i-\mathbf{r}_j)\cdot\hat{\mathbf{d}}_j\,. \tag{2.47}$$

In the point dipole approximation, the interactions between the resonators depend exclusively upon the orientation and relative positions of the point sources. The coupling matrix $\mathcal{C}$ is

$$\mathcal{C} = \Delta - \frac{1}{2}\Upsilon + \frac{1}{2}\Big[i\mathcal{C}_{\mathrm{E1}} + i\mathcal{C}_{\mathrm{M1}} + \mathcal{C}_{\mathrm{X1}} + \mathcal{C}^T_{\mathrm{X1}}\Big]\,, \tag{2.48}$$

where

$$\mathcal{C}_{\mathrm{E1}} = \Upsilon^{1/2}_{\mathrm{E1}}\mathcal{G}_{\mathrm{E1}}\Upsilon^{1/2}_{\mathrm{E1}}\,, \tag{2.49a}$$

$$\mathcal{C}_{\mathrm{M1}} = \Upsilon^{1/2}_{\mathrm{M1}}\mathcal{G}_{\mathrm{M1}}\Upsilon^{1/2}_{\mathrm{M1}}\,, \tag{2.49b}$$

$$\mathcal{C}_{\mathrm{X1}} = \Upsilon^{1/2}_{\mathrm{M1}}\mathcal{G}_{\mathrm{X1}}\Upsilon^{1/2}_{\mathrm{E1}}\,. \tag{2.49c}$$

The diagonal elements of $\mathcal{C}$ contain the detuning of the incident EM field from the resonator's resonance frequency ω_j, and the resonator's total decay rate Γ_j. The detuning is described by the diagonal matrix Δ, where [79]

$$\big[\Delta\big]_{j,j} \equiv -i(\omega_j - \Omega_0)\,, \tag{2.50}$$

and the decay rate by the diagonal matrix Υ, with

$$\big[\Upsilon\big]_{j,j} = \Gamma_{\mathrm{E1},j} + \Gamma_{\mathrm{M1},j} + \Gamma_{\mathrm{O},j}\,. \tag{2.51}$$

The radiative decay rates of each resonator are contained in the diagonal matrices Υ_{E1} and Υ_{M1}, where,

$$\big[\Upsilon_{\mathrm{E1}}\big]_{j,j} = \Gamma_{\mathrm{E1},j}\,, \tag{2.52}$$

$$\big[\Upsilon_{\mathrm{M1}}\big]_{j,j} = \Gamma_{\mathrm{M1},j}\,. \tag{2.53}$$

In principle, when one knows the resonance frequency of the resonator and the decay rates $\Gamma_{\mathrm{E1},j}$, $\Gamma_{\mathrm{M1},j}$ and $\Gamma_{\mathrm{O},j}$, then the scattered fields equations (2.37) and (2.38) are readily solved. In practice, however, the resonance frequency and decay rates are not readily available, and one must make approximations depending on the geometry and material of the resonators. In Appendix F, we utilize the Drude model, briefly introduced in Chapter 1, in a novel way to calculate the resonance frequency and relative decay rate $\Gamma_{\mathrm{E1}}/\Gamma_{\mathrm{O}}$ for gold nanorods.

2.3 Summary

The point dipole approximation reviewed above is suitable for general resonator systems which possess both electric and magnetic dipole sources. In the form presented, the point dipole approximation has previously been successfully applied to the studies of collective effects in planar resonator arrays, e.g., the transmission properties [80, 81] and the development of an electron-beam-driven light source from the collective response [83].

One can, in principle, tailor the dipole approximation to more accurately account for the geometry of the resonators. Such approximations may include sources which possess only one of electric or magnetic dipole moments; achieved above by simply setting, $\Gamma_{\mathrm{M1},j} \equiv 0$ and $\Gamma_{\mathrm{E1},j} \equiv 0$, respectively. Additionally, one may include higher order multipole moments. In Chapter 3, we extend the point dipole approximation, with original work, whereby the point electric quadrupole approximation is also included in the resonators' scattered EM fields. We show how simple $2N$ point electric dipole resonator systems can be approximated by N point magnetic dipole and electric quadrupole resonators. Additionally, in Chapter 4, we will show how the model can account for the finite-size and geometry of the resonators. In Chapter 5, we use the model introduced above and the original work contained in Chapter 4 to model a toroidal metamolecule comprising plasmonic nanorods.

Chapter 3

Interacting point multipole resonators

In Chapter 2, we reviewed the general model for interacting resonators and the point electric and magnetic dipole approximation of the scattered EM fields. The point dipole approximation works well for simple resonator systems. However, as the complexity of even simple systems increases one may have to incorporate higher order multipoles to explain the complex interactions of the simple resonators. Additionally, one may wish to simplify more complex resonator systems that are more appropriately modeled with higher order multipoles. In this chapter, we present original work whereby the point electric quadrupole contribution to each resonator is formulated. In Section 3.1, we introduce the formalism for the electric quadrupole contributions. In Section 3.2 we analyze in detail different point multipole resonator systems. Some concluding remarks are included in Section 3.3.

3.1 Point electric quadrupole approximation

The electric quadrupole moments can produce non trivial interacting terms with electric dipoles, magnetic dipoles and other electric quadrupoles. As we show later, the electric quadrupole radiative decay is of the same order of magnitude as the magnetic dipole, as such the magnetic dipole and electric quadrupole contributions to the EM scattered fields are not easily decoupled. In the remainder of this chapter, we make frequent reference to the equations and model reviewed in Chapter 2.

Equation (2.48) describes the interaction between point electric and magnetic dipole sources. When electric quadrupole sources are also included, we extend equation (2.48) to include the interactions between the electric and magnetic dipoles with electric quadrupoles, and the electric quadrupole–electric quadrupole interactions,

$$\begin{aligned}\mathcal{C} = \Delta - \frac{1}{2}\Upsilon + \frac{1}{2}\Big[& i\mathcal{C}_{\mathrm{E1}} + i\mathcal{C}_{\mathrm{M1}} + \mathcal{C}_{\mathrm{X1}} + \mathcal{C}_{\mathrm{X1}}^{T} \\ & + i\mathcal{C}_{\mathrm{E2}} + i\mathcal{C}_{\mathrm{X2e}} + i\mathcal{C}_{\mathrm{X2e}}^{T} + \mathcal{C}_{\mathrm{X2m}} + \mathcal{C}_{\mathrm{X2m}}^{T}\Big] \,. \end{aligned} \tag{3.1}$$

The diagonal elements of equation (3.1) contain the detuning Δ [see equation (2.50)], and the total decay rate Υ for the resonator

$$\left[\Upsilon\right]_{j,j} = \Gamma_{\mathrm{E1},j} + \Gamma_{\mathrm{M1},j} + \Gamma_{\mathrm{E2},j} + \Gamma_{\mathrm{O},j} \,. \tag{3.2}$$

Here, Γ_{E2} denotes the electric quadrupole radiative emission rate, the derivation of which is a major focus of this chapter. The electric and magnetic dipole emission rates are Γ_{E1} and Γ_{M1}, respectively, see equations (2.34) and (2.35). The matrices for electric and magnetic dipole interactions, $\mathcal{C}_{\mathrm{E1}}$, $\mathcal{C}_{\mathrm{M1}}$, and $\mathcal{C}_{\mathrm{X1}}$ are given in equation (2.49). The additional interaction terms are similarly defined,

$$\mathcal{C}_{\mathrm{E2}} = \Upsilon_{\mathrm{E2}}^{1/2}\mathcal{G}_{\mathrm{E2}}\Upsilon_{\mathrm{E2}}^{1/2} \,, \tag{3.3a}$$

$$\mathcal{C}_{\mathrm{X2e}} = \Upsilon_{\mathrm{E1}}^{1/2}\mathcal{G}_{\mathrm{X2e}}\Upsilon_{\mathrm{E2}}^{1/2} \,, \tag{3.3b}$$

$$\mathcal{C}_{\mathrm{X2m}} = \Upsilon_{\mathrm{M1}}^{1/2}\mathcal{G}_{\mathrm{X2m}}\Upsilon_{\mathrm{E2}}^{1/2} \,, \tag{3.3c}$$

and describe: electric quadrupole–electric quadrupole; electric quadrupole–electric dipole; and electric quadrupole–magnetic dipole interactions, respectively. The transpose matrices, $\mathcal{C}_{\mathrm{X2e}}^{T}$ and $\mathcal{C}_{\mathrm{X2m}}^{T}$ are, respectively, the electric dipole–electric quadrupole and magnetic dipole–electric quadrupole interactions. Explicit expressions for: $\mathcal{G}_{\mathrm{E2}}$; $\mathcal{G}_{\mathrm{X2e}}$; and $\mathcal{G}_{\mathrm{X2m}}$ are given in equations (3.41), (3.45), and (3.49), respectively, and are derived in this chapter.

The electric dipole and magnetic dipole radiative emission rates are contained in the diagonal matrices Υ_{E1} and Υ_{M1}, respectively, see equations (2.52) and (2.53). The electric quadrupole radiative emission rate is contained in the equivalent diagonal matrix Υ_{E2}, where

$$\left[\Upsilon_{\mathrm{E2}}\right]_{j,j} = \Gamma_{\mathrm{E2},j} \,. \tag{3.4}$$

Because we adopt the point multipole approximation, the interactions between resonators depend exclusively on the orientations and relative positions of the point sources. Still, equation (3.1) is complicated, however, we may model a range of resonator systems in a relatively simple manner. An electric dipole only approximation is achieved by setting, in equation (3.1), $\Gamma_{\mathrm{M1},j} \equiv \Gamma_{\mathrm{E2},j} \equiv 0$. Similarly, we can model magnetic dipole only interactions or electric quadrupole interactions, or some combination.

3.1.1 Interacting point electric quadrupoles

The scattered EM fields for a general polarization source are given by the first and second integrals of equations (2.30) and (2.31), respectively. In the point multipole approximation, the charge distribution comprises contributions from the electric multipole moments. In a similar manner, the polarization density also contains contributions from the different multipole moments, and we can expand $\mathbf{P}_j(\mathbf{r}, t)$ to include the electric quadrupole term $\mathbf{p}_j^{\mathrm{q}}(\mathbf{r})$,

$$\begin{aligned} \mathbf{P}_j(\mathbf{r}, t) &= Q_j(t)\mathbf{p}_j(\mathbf{r})\,, \\ &= Q_j(t)\Big[\mathbf{p}_j^{\mathrm{d}}(\mathbf{r}) + \mathbf{p}_j^{\mathrm{q}}(\mathbf{r}) + \ldots\Big]\,. \end{aligned} \tag{3.5}$$

While $\mathbf{p}_j^{\mathrm{d}}(\mathbf{r})$ is a vector quantity, $\mathbf{p}_j^{\mathrm{q}}(\mathbf{r})$ is a tensor. The index α of the Cartesian component of the electric quadrupole contribution of the jth resonator is $p_{\alpha,j}^{\mathrm{q}}(\mathbf{r})$, where we define [63]

$$p_{\alpha,j}^{\mathrm{q}}(\mathbf{r}) = -\sum_{\beta} A_{\alpha\beta,j}\frac{\partial}{\partial r_\beta}\delta(\mathbf{r} - \mathbf{r}_j)\,. \tag{3.6}$$

Here, $A_{\alpha\beta,j}$ is symmetric and traceless with dimensions of area, and the indices α, β refer to the Cartesian coordinates x, y, z and the summation is over β. The exact form of $A_{\alpha\beta,j}$ depends on the geometry of the resonator.

The scattered electric $\mathbf{E}_{\mathrm{E2},j}(\mathbf{r})$ and magnetic $\mathbf{H}_{\mathrm{E2},j}(\mathbf{r})$ fields due to the quadrupole moment located at $\mathbf{r}'$ are derived from the first terms, respectively, in equations (2.3) and (2.4). Here, the spatial profile of the polarization density in equation (2.10) has Cartesian component α defined in equation (3.6), and we find the Cartesian components ν of $\mathbf{E}_{\mathrm{E2},j}(\mathbf{r})$ and $\mathbf{H}_{\mathrm{E2},j}(\mathbf{r})$ are;

$$E_{\mathrm{E2},\nu,j}(\mathbf{r}) = \frac{Q_j k^3}{4\pi\epsilon_0}\sum_{\alpha}\int \mathrm{d}^3r'\, G_{\nu\alpha}(\mathbf{r} - \mathbf{r}')p_{\alpha,j}^{\mathrm{q}}(\mathbf{r}')\,, \tag{3.7}$$

$$H_{\mathrm{E2},\nu,j}(\mathbf{r}) = -\frac{cQ_j k^3}{4\pi}\sum_{\alpha}\int \mathrm{d}^3r'\, G_{\times,\nu\alpha}(\mathbf{r} - \mathbf{r}')p_{\alpha,j}^{\mathrm{q}}(\mathbf{r}')\,. \tag{3.8}$$

The radiation kernels $G_{\nu\alpha}(\mathbf{r})$ and $G_{\times,\nu\alpha}(\mathbf{r})$ are the tensor components ($\nu, \alpha = x, y, z$) of the radiation kernels defined in equations (2.5) and (2.6), respectively.

While in the electric and magnetic dipole limit the radiation kernels act directly on the moments $\mathbf{p}_j^{\mathrm{d}}(\mathbf{r})$ and $\mathbf{w}_j(\mathbf{r})$, respectively, the quadrupole EM fields, equations (3.7) and (3.8), are more complicated due to the derivative in $p_{\alpha,j}^{\mathrm{q}}(\mathbf{r})$. After integrating by parts equations (3.7) and (3.8), the EM field components ν are

$$E_{\mathrm{E2},\nu,j}(\mathbf{r}) = \frac{Q_j k^3}{4\pi\epsilon_0} \sum_{\alpha,\beta} \frac{\partial}{\partial r_\beta} G_{\nu\alpha}(\mathbf{r}-\mathbf{r}_j) A_{\alpha\beta,j}\,, \tag{3.9}$$

$$H_{\mathrm{E2},\nu,j}(\mathbf{r}) = -\frac{c Q_j k^3}{4\pi} \sum_{\alpha,\beta} \frac{\partial}{\partial r_\beta} G_{\times,\nu\alpha}(\mathbf{r}-\mathbf{r}_j) A_{\alpha\beta,j}\,. \tag{3.10}$$

The derivatives of the radiation kernel $\mathbf{G}(\mathbf{r})$ and cross kernel $\mathbf{G}_\times(\mathbf{r})$, with respect to the Cartesian coordinate $r_{\mu=x,y,z}$ are given in Appendix D, see equations (D.1) and (D.2).

In Reference 39, the EM fields of an oscillating electric quadrupole source in Cartesian coordinates are given only in the radiation zone. Equations (3.9) and (3.10) are the full EM field equations evaluated at $\mathbf{r}$ (in Cartesian coordinates), for an oscillating electric quadrupole source located at $\mathbf{r}'$. The EM fields are determined by contracting equations (D.1) and (D.2), acting on the quadrupole moment $A_{\alpha\beta,j}$.

In the electric dipole approximation, it is a relatively simple exercise to expand the radiation kernel, in powers of kr, to obtain an expression for the electric dipole radiative decay rate. For the electric quadrupole, there is no simple expansion for equation (D.1). In order to determine an expression for the electric quadrupole (and other higher order multipoles) self interaction strength and radiative emission rate, we find it convenient to compare standard formulae for the multipole radiated power [39, 63] to the [rate of change of] energy of an oscillator.

In general, the radiated power P may be calculated from the intensity of the radiated EM field, and its flux through a spherical surface in the region $kr \gg 1$. The total power is a superposition of all the multipole radiated powers: P_{E1}; P_{M1}; P_{E2}; etc, where the subscripts E1, M1, and E2 denote the electric dipole, magnetic dipole and electric quadrupole contributions, respectively.

The radiated power can be obtained by integrating [39]

$$\frac{\mathrm{d}P}{\mathrm{d}\Omega} = \lim_{r\to\infty} r^2 \hat{\mathbf{r}}\cdot \left[\mathbf{E}(\mathbf{r}) \times \mathbf{H}(\mathbf{r})\right], \tag{3.11}$$

over a spherical surface, where $\mathrm{d}\Omega$ is the solid angle element, and $\hat{\mathbf{r}}$ the vector normal to the surface. In the radiation zone, the fields $\mathbf{E}_{\mathrm{rad}}(\mathbf{r})$ and $\mathbf{H}_{\mathrm{rad}}(\mathbf{r})$ vary as $1/r$, and together with $\hat{\mathbf{r}}$, form a right handed triad. The magnitudes of the EM fields in the radiation zone are simply related, $|\mathbf{E}_{\mathrm{rad}}(\mathbf{r})| = c\mu_0 |\mathbf{H}_{\mathrm{rad}}(\mathbf{r})|$, and Faraday's law implies; $\hat{\mathbf{r}} \times \mathbf{E}_{\mathrm{rad}}(\mathbf{r}) = c\mu_0 \mathbf{H}_{\mathrm{rad}}(\mathbf{r})$. The angular distribution of power is more simply written, by taking the real part of equation (3.11),

$$\frac{\mathrm{d}P}{\mathrm{d}\Omega} = \frac{r^2}{c\mu_0} |\mathbf{E}_{\mathrm{rad}}(\mathbf{r})|^2\,. \tag{3.12}$$

The EM fields in the radiation zone for electric quadrupoles are much simpler than their full field equations; equations (3.9) and (3.10). In the limit $kr \gg 1$ we adopt the notation of Reference 39, and define a quadrupole vector component, of the jth resonator $\mathbf{q}_j(\hat{\mathbf{r}})$, where

$$[\mathbf{q}_j(\hat{\mathbf{r}})]_\alpha = \sum_{\beta=1}^{3} q_{\alpha\beta,j}\hat{r}_{\beta,j}\,. \tag{3.13}$$

Here, α, β refer to the Cartesian components, $\hat{\mathbf{r}}$ is the unit vector in the direction of $\mathbf{r}$, and $q_{\alpha\beta,j}$ is the electric quadrupole moment tensor, defined as [63]

$$q_{\alpha\beta,j} = \frac{1}{2}\int \mathrm{d}^3r\, r_\alpha r_\beta \rho_j(\mathbf{r},t)\,. \tag{3.14}$$

The charge density $\rho_j(\mathbf{r},t)$ in equation (3.14) is defined in equation (2.12). The electric $\mathbf{E}_{\mathrm{rad,E2},j}(\mathbf{r})$ and magnetic $\mathbf{H}_{\mathrm{rad,E2},j}(\mathbf{r})$ radiated fields from the jth electric quadrupole are [39]

$$\mathbf{E}_{\mathrm{rad,E2},j}(\mathbf{r}) = i\frac{k^3}{4\pi\epsilon_0}\frac{e^{ikr}}{r}\hat{\mathbf{r}} \times \left[\hat{\mathbf{r}} \times \mathbf{q}_j(\hat{\mathbf{r}})\right], \tag{3.15}$$

$$\mathbf{H}_{\mathrm{rad,E2},j}(\mathbf{r}) = i\frac{ck^3}{4\pi}\frac{e^{ikr}}{r}\hat{\mathbf{r}} \times \mathbf{q}_j(\hat{\mathbf{r}})\,, \tag{3.16}$$

where $r = |\mathbf{r} - \mathbf{r}_j|$. The electric quadrupole contribution to the power P_{E2} is [63]

$$\frac{\mathrm{d}P_{\mathrm{E2},j}}{\mathrm{d}\Omega} = \frac{\mu_0 c^3 k^6}{16\pi^2}|\hat{\mathbf{r}} \times \mathbf{q}_j(\hat{\mathbf{r}})|^2\,. \tag{3.17}$$

The electric quadrupole radiated power $P_{\mathrm{E2},j}$, is the integral of equation (3.17) over all angles [63]. We find [63] [see Appendix D.2],

$$P_{\mathrm{E2},j} = \frac{\mu_0 c^3 k^6}{20\pi}\sum_{\alpha,\beta}\left[q_{\alpha\beta,j}q_{\alpha\beta,j} - \frac{1}{3}q_{\alpha\alpha,j}q_{\beta\beta,j}\right], \tag{3.18}$$

The quadrupole moment tensors, $q_{\alpha\beta,j}$ and $A_{\alpha\beta,j}$, and the dynamic variable $b_j(t)$ of the jth resonator are related through the charge density $\rho_j(\mathbf{r},t)$. The electric quadrupole component of the charge density, from equations (2.12) and (3.6) is

$$\rho(\mathbf{r},t) = Q_j(t)\sum_{\alpha\beta,j}\frac{\partial}{\partial r_\alpha}\left[A_{\alpha\beta,j}\frac{\partial}{\partial r_\beta}\delta(\mathbf{r}-\mathbf{r}_j)\right], \tag{3.19}$$

where the summation is over the Cartesian coordinates ($\alpha, \beta = x, y, z$). Substituting equation (3.19) into equation (3.14),

$$q_{\alpha\beta,j} = \frac{1}{2}Q_j(t)\int \mathrm{d}^3r\, r_\mu r_\nu \frac{\partial}{\partial r_\alpha}\left[A_{\alpha\beta,j}\frac{\partial}{\partial r_\beta}\delta(\mathbf{r}-\mathbf{r}_j)\right]. \tag{3.20}$$

Integration of equation (3.20), by parts twice yields

$$q_{\alpha\beta,j} = \frac{1}{2}Q_j(t)\int \mathrm{d}^3r \left[\frac{\partial}{\partial r_\alpha}\frac{\partial}{\partial r_\beta} r_\mu r_\nu\right] A_{\alpha\beta,j}\delta(\mathbf{r}-\mathbf{r}_j)\,. \tag{3.21}$$

The term in parenthesis in equation (3.21), simplifies considerably because the derivatives result in Kronecker δ functions,

$$\frac{\partial}{\partial r_\alpha}\frac{\partial}{\partial r_\beta} r_\mu r_\nu = \frac{\partial}{\partial r_\alpha}\left[\delta_{\beta\mu} r_\nu + \delta_{\beta\nu} r_\mu\right] = \delta_{\alpha\nu}\delta_{\beta\mu} + \delta_{\alpha\mu}\delta_{\beta\nu} = 2\,. \tag{3.22}$$

The remaining integral is easily evaluated because of the δ function. Writing the charge $Q_j(t)$ in terms of the dynamic variable $b_j(t)$ [see equation (2.25)], we finally have the relationship between $q_{\alpha\beta,j}$, $b_j(t)$ and $A_{\alpha\beta,j}$;

$$q_{\alpha\beta,j} = \sqrt{\frac{\omega_j C_j}{2}}\, b_j(t) A_{\alpha\beta,j}\,. \tag{3.23}$$

The energy U_j of an isolated oscillator, from its Hamiltonian, is analogous to that of an LC circuit [79]

$$U_j(t) = \omega_j \left|b_j\right|^2 . \tag{3.24}$$

The electric quadrupole radiated power $P_{\mathrm{E2},j}$ of the oscillator, is the rate of change of equation (3.24),

$$P_{\mathrm{E2},j} = -\frac{\mathrm{d}U_j}{\mathrm{d}t} = \omega_j \Gamma_{\mathrm{E2},j} \left|b_j\right|^2 . \tag{3.25}$$

Here, ω_j is the resonance frequency and $\Gamma_{\mathrm{E2},j}$ the decay rate of the electric quadrupole. Comparing equations (3.18) and (3.25), we obtain the rate at which a resonator radiates energy in the point electric quadrupole approximation as

$$\Gamma_{\mathrm{E2},j} = \frac{C_j A_{\mathrm{E},j}^2 \omega_j^6}{20\pi\epsilon_0 c^5}\,, \tag{3.26}$$

where we define

$$A_{\mathrm{E},j}^2 = \sum_{\alpha,\beta}\left[A_{\alpha\beta,j}A_{\alpha\beta,j} - \frac{1}{3}A_{\alpha\alpha,j}A_{\beta\beta,j}\right]\,, \tag{3.27}$$

as an effective area of the electric quadrupole. Again, the indices α, β refer to the Cartesian components of the quadrupole moment and repeated indices are summed over.

With the radiative emission rates of the electric quadrupole equation (3.26), and the electric and magnetic dipoles equations (2.34) and (2.35), respectively, we can express the normal mode oscillator amplitudes equation (2.25) in terms of the contributing multipole moments

$$b_j(t) = \sqrt{\frac{k^3}{12\pi\epsilon_0}}\left[Q_j \frac{H_j}{\sqrt{\Gamma_{\mathrm{E1},j}}} + kQ_j\sqrt{\frac{3}{5}}\frac{A_{\mathrm{E},j}}{\sqrt{\Gamma_{\mathrm{E2},}}} + i\frac{I_j}{c}\frac{A_{\mathrm{M},j}}{\sqrt{\Gamma_{\mathrm{M1},j}}}\right]\,. \tag{3.28}$$

The real part of equation (3.28) comprises the electric dipole and electric quadrupole contributions. The imaginary part corresponds to the magnetic dipole contribution.

In the point multipole approximation, the radiative emission rates of the magnetic dipole and the electric quadrupole both depend on their respective effective cross sectional areas $A_{\mathrm{M},j}$ and $A_{\mathrm{E},j}$, see equations (2.35) and (3.26), respectively. For simplicity, we assume that the magnetic dipole and electric quadrupole have the same resonance frequency ω_j [equation (2.9)]. Comparing equations (2.35) and (3.26), we find $\Gamma_{\mathrm{M1},j}$ and $\Gamma_{\mathrm{E2},j}$ are of the same order of magnitude, their relative radiation emission rates are

$$\frac{\Gamma_{\mathrm{E2},j}}{\Gamma_{\mathrm{M1},j}} = \frac{3}{10}\frac{A_{\mathrm{E},j}^2}{A_{\mathrm{M},j}^2} \,. \tag{3.29}$$

In Section 2.2, the amplitudes of the scattered EM fields were proportional to the electric dipole and magnetic dipole radiative emission rates. Here, the full electric quadrupole EM field amplitudes, equations (3.9) and (3.10), are proportional to the electric quadrupole decay rate $\Gamma_{\mathrm{E2},j}$. We write the scaled EM fields of the jth electric quadrupole source as

$$E_{\mathrm{E2},\nu,j}(\mathbf{r}) = b_j\sqrt{\frac{\wp_0}{\epsilon_0}}\sum_{\alpha,\beta}\frac{\partial}{\partial k r_\beta}G_{\nu\alpha}(\mathbf{r}-\mathbf{r}_j)\hat{A}_{\alpha\beta,j}\,, \tag{3.30}$$

$$H_{\mathrm{E2},\nu,j}(\mathbf{r}) = -b_j\sqrt{\frac{\wp_0}{\mu_0}}\sum_{\alpha,\beta}\frac{\partial}{\partial k r_\beta}G_{\times,\nu\alpha}(\mathbf{r}-\mathbf{r}_j)\hat{A}_{\alpha\beta,j}\,, \tag{3.31}$$

where the constant $\wp_0$ is defined as

$$\wp_0 = \frac{5k^3}{8\pi}\Gamma_{\mathrm{E2},j}\,, \tag{3.32}$$

and $\hat{A}_{\alpha\beta,j}$ is a tensor which defines the charge configuration of the quadrupole moment

$$\hat{A}_{\alpha\beta,j} = \frac{A_{\alpha\beta,j}}{A_{\mathrm{E},j}}\,. \tag{3.33}$$

The jth electric quadrupole is also driven by the external electric fields $\mathbf{E}_{\mathrm{ext},j}(\mathbf{r})$, resulting in the induced emf $\mathcal{E}^{\mathrm{E2}}_{\mathrm{ext},j}$, with

$$\mathcal{E}^{\mathrm{E2}}_{\mathrm{ext},j} = \frac{1}{\sqrt{\omega_j L_j}}\sum_{\nu}\int \mathrm{d}^3r\, p^{\mathrm{q}}_{\nu,j}(\mathbf{r})E_{\mathrm{ext},\nu,j}(\mathbf{r})\,. \tag{3.34}$$

Here, the mode function $p^{\mathrm{q}}_{\nu,j}(\mathbf{r})$ is defined in equation (3.6). For point electric quadrupole sources, the jth electric quadrupole moment $A_{\alpha\beta,j}$ interacts with the gradient of the external electric field,

$$\mathcal{E}^{\mathrm{E2}}_{\mathrm{ext},j} = \frac{1}{\sqrt{\omega_j L_j}}\sum_{\alpha\beta}A_{\alpha\beta,j}\left[\frac{\partial}{\partial r_\beta}E_{\mathrm{ext},\alpha,j}(\mathbf{r})\right]. \tag{3.35}$$

The external electric field [equation (2.16)] comprises the incident electric field and the different multipole scattered fields. These different contributions to the external electric field driving the electric quadrupole source allow us to decompose the resulting emf into different components;

$$\mathcal{E}^{\mathrm{E2}}_{\mathrm{ext},j} = \mathcal{E}^{\mathrm{E2}}_{\mathrm{in},j} + \sum_{i\neq j}\left[\mathcal{E}^{\mathrm{sc,X2e}}_{i,j} + \mathcal{E}^{\mathrm{sc,X2m}}_{i,j} + \mathcal{E}^{\mathrm{sc,E2}}_{i,j} + \ldots\right]. \tag{3.36}$$

In equation (3.36), the incident EM field contribution to the electric quadrupole emf follows from equation (3.35), with the incident displacement field equation (2.14)

$$\mathcal{E}^{\mathrm{E2}}_{\mathrm{in},j} = \frac{1}{\sqrt{\omega_j L_j}} \sum_{\alpha\beta} A_{\alpha\beta,j}\left[\frac{\partial}{\partial r_\beta} E_{\mathrm{in},\alpha,j}(\mathbf{r})\right]. \tag{3.37}$$

The contributions $\mathcal{E}^{\mathrm{sc,X2e}}_{i,j}$ and $\mathcal{E}^{\mathrm{sc,X2m}}_{i,j}$ are due to the interactions of electric and magnetic dipoles, respectively, with electric quadrupoles. We discuss these contributions in detail later. Here, we provide the electric quadrupole driven contribution to the emf from two interacting electric quadrupoles, $\mathcal{E}^{\mathrm{sc,E2}}_{i,j}$, the counterpart to the emf from two electric dipoles [see equation (2.41)]. With the definition of the emf, equation (3.34), we have

$$\begin{aligned}\mathcal{E}^{\mathrm{sc,E2}}_{i,j} = -\frac{1}{\sqrt{\omega_j L_j}}\frac{Q_j k^3}{4\pi\epsilon_0}\sum_\nu \int \mathrm{d}^3 r \left[\sum_\eta A_{\nu\eta,i}\frac{\partial}{\partial r_\eta}\delta(\mathbf{r}-\mathbf{r}_i)\right] \\ \times\left[\sum_{\alpha\beta}\frac{\partial}{\partial r_\beta} G_{\nu\alpha}(\mathbf{r}-\mathbf{r}_j) A_{\alpha\beta,j}\right].\end{aligned} \tag{3.38}$$

The first term in parenthesis in equation (3.38) is the mode function $p^{\mathrm{q}}_{\nu,i}(\mathbf{r})$ of the ith electric quadrupole [see equation (3.6)]. The second term in parenthesis is the scattered electric field from the jth electric quadrupole, $E_{\mathrm{E2},\nu,j}(\mathbf{r})$ [see equation (3.9)]. Integration of equation (3.38) by parts, we have

$$\mathcal{E}^{\mathrm{sc,E2}}_{i,j} = \frac{1}{\sqrt{\omega_j L_j}}\frac{Q_j k^3}{4\pi\epsilon_0}\sum_\nu \int \mathrm{d}^3 r\, A_{\nu\eta,i}\delta(\mathbf{r}-\mathbf{r}_i)\sum_{\eta\alpha\beta}\left[\frac{\partial}{\partial r_\eta}\frac{\partial}{\partial r_\beta} G_{\nu\alpha}(\mathbf{r}_i-\mathbf{r}_j)\right] A_{\alpha\beta,j}. \tag{3.39}$$

The integral in equation (3.39) is readily carried out over the δ function. The second derivatives of the radiation kernel with respect to the Cartesian coordinate $r_{\mu=x,y,z}$ are given in equations (D.3) and (D.4), see Appendix D. The electric quadrupole moment $A_{\alpha\beta,j}$, in equation (3.39), and the decay rate $\Gamma_{\mathrm{E2},j}$ are related through the effective area $A_{\mathrm{E},j}$ appearing in both equations (3.26) and (3.33). This allows us to write equation (3.39) more compactly as

$$\mathcal{E}^{\mathrm{sc,E2}}_{i,j} = \sqrt{\Gamma_{\mathrm{E2},i}\Gamma_{\mathrm{E2},j}}\,[\mathcal{G}_{\mathrm{E2}}]_{i,j}\frac{b_j}{\sqrt{2}}. \tag{3.40}$$

The matrix $\mathcal{G}_{\mathrm{E2}}$ is the contribution to $\mathcal{C}_{\mathrm{E2}}$ in equation (3.3a), with off-diagonal components

$$[\mathcal{G}_{\mathrm{E2}}]_{i,j} = \frac{15}{4} \sum_{\nu,\eta,\alpha,\beta} \hat{A}_{\nu\eta,i} \frac{\partial^2}{\partial k r_\eta \partial k r_\beta} G_{\nu\alpha}(\mathbf{r}_i - \mathbf{r}_j) \hat{A}_{\alpha\beta,j} \,. \tag{3.41}$$

Equation (3.41) is, in general, complicated, however, as we show later in Section 3.2.3, for simple point quadrupole systems, equation (3.41) simplifies considerably. The coupling matrix $\mathcal{C}$ for interacting electric quadrupoles only is

$$\mathcal{C} = \Delta - \frac{1}{2}\Upsilon + \frac{i}{2}\mathcal{C}_{\mathrm{E2}} \,, \tag{3.42}$$

where $\mathcal{C}_{\mathrm{E2}}$ is given in equation (3.3a). The diagonal elements of $\mathcal{C}$ contain the detuning Δ and total decay rate Υ. Equation (2.50) gives the detuning, the decay rates in the electric quadrupole approximation are

$$\left[\Upsilon\right]_{j,j} = \Gamma_{\mathrm{E2},j} + \Gamma_{\mathrm{O},j} \,. \tag{3.43}$$

3.1.2 Interacting point electric and magnetic dipoles and electric quadrupoles

In Section 3.1, we discussed the interactions between two point electric quadrupoles. In principle, the scattered EM fields from an electric or magnetic dipole may drive the electric quadrupole current oscillations and vice versa. There may also be driving of the electric (magnetic) dipole current oscillations by the scattered EM fields from a magnetic (electric) dipole. The cross driving between electric and magnetic dipoles was discussed in Section 2.2. In this section, we introduce the cross coupling of the electric quadrupole to the electric and magnetic dipoles. The magnetic dipole-electric quadrupole interactions are of particular importance because their individual contributions are not easily decoupled as they can be of the same order of magnitude, see e.g., equation (3.29).

3.1.2.1 Electric dipole-electric quadrupole interactions

The electric field scattered by an electric dipole is given by the first integral in equation (2.37) and the electric field scattered by an electric quadrupole in equation (3.30). These scattered electric fields drive the charge oscillations in external electric quadrupole and electric dipole sources, respectively, giving rise to the cross driving emf $\mathcal{E}^{\mathrm{sc,X2e}}_{i,j}$, where

$$\mathcal{E}^{\mathrm{sc,X2e}}_{i,j} = \left[\sqrt{\Gamma_{\mathrm{E2},i}\Gamma_{\mathrm{E1},j}} \, [\mathcal{G}_{\mathrm{X2e}}]_{i,j} + \sqrt{\Gamma_{\mathrm{E1},i}\Gamma_{\mathrm{E2},j}} \, [\mathcal{G}_{\mathrm{X2e}}]^T_{i,j} \right] \frac{b_j}{\sqrt{2}} \,. \tag{3.44}$$

The matrix $\mathcal{G}_{\mathrm{X2e}}$ (and its transpose $\mathcal{G}^T_{\mathrm{X2e}}$) have zero diagonal elements; the off-diagonal elements are defined by

$$\left[\mathcal{G}_{\mathrm{X2e}}\right]_{i,j} = \sqrt{\frac{15}{2}} \sum_{\nu,\eta,\alpha} \hat{A}_{\nu\eta,i} \frac{\partial}{\partial k r_\eta} G_{\nu\alpha}(\mathbf{r}_i - \mathbf{r}_j) \hat{d}_{\alpha,j} \,. \tag{3.45}$$

The interactions between an electric quadrupole (electric dipole) with the EM fields from an electric dipole (electric quadrupole) are described by $\mathcal{G}_{\mathrm{X2e}}$ (and its transpose $\mathcal{G}^T_{\mathrm{X2e}}$). The derivatives of the radiation kernel are given in equation (D.1) [see Appendix D].

The interaction matrix $\mathcal{C}_{\mathrm{X2e}}$ (and its transpose $\mathcal{C}^T_{\mathrm{X2e}}$) in the equation of motion, equation (2.26), for the cross driving of electric dipoles and electric quadrupoles (and vice versa) are given in equation (3.3b). The components of $\mathcal{C}_{\mathrm{X2e}}$ and $\mathcal{C}^T_{\mathrm{X2e}}$ are related to $\mathcal{E}^{\mathrm{sc,X2e}}_{i,j}$ by

$$\left[C_{\mathrm{X2e}}\right]_{i,j} = \sqrt{\Gamma_{\mathrm{E2},i}\Gamma_{\mathrm{E1},j}} \left[\mathcal{G}_{\mathrm{X2e}}\right]_{i,j} . \tag{3.46}$$

3.1.2.2 Magnetic dipole-electric quadrupole interactions

The electric field from an oscillating magnetic dipole is given by the second integral in equation (2.37), and the magnetic field from an electric quadrupole in equation (3.31). These scattered EM fields drive the external electric quadrupole and magnetic dipole sources, respectively, resulting in an emf $\mathcal{E}^{\mathrm{sc,X2m}}_{i,j}$ and flux $\Phi^{\mathrm{sc,X2m}}_{i,j}$

$$\mathcal{E}^{\mathrm{sc,X2m}}_{i,j} = -\sqrt{\Gamma_{\mathrm{E2},i}\Gamma_{\mathrm{M1},j}} \left[\mathcal{G}_{\mathrm{X2m}}\right]_{i,j} \frac{b_j}{\sqrt{2}} , \tag{3.47}$$

$$\Phi^{\mathrm{sc,X2m}}_{i,j} = -\frac{1}{\omega_j} \sqrt{\Gamma_{\mathrm{E2},i}\Gamma_{\mathrm{M1},j}} \left[\mathcal{G}_{\mathrm{X2m}}\right]^T_{i,j} \frac{b_j}{\sqrt{2}} . \tag{3.48}$$

The terms in $\mathcal{C}_{\mathrm{X2m}}$ then follow as in the previous section, where the off-diagonal elements of $\mathcal{G}_{\mathrm{X2m}}$ are given by

$$\left[\mathcal{G}_{\mathrm{X2m}}\right]_{i,j} = \sqrt{\frac{15}{2}} \sum_{\nu,\eta,\alpha} \hat{A}_{\nu\eta,i} \frac{\partial}{\partial k r_\eta} G_{\times,\nu\alpha}(\mathbf{r}_i - \mathbf{r}_j) \hat{m}_{\alpha,j} \,, \tag{3.49}$$

where the derivatives of the cross kernel are given in equation (D.2) [see Appendix D], and

$$\left[C_{\mathrm{X2m}}\right]_{i,j} = -\sqrt{\Gamma_{\mathrm{E2},i}\Gamma_{\mathrm{M1},j}} \left[\mathcal{G}_{\mathrm{X2m}}\right]_{i,j} . \tag{3.50}$$

For simple interacting electric quadrupole-magnetic dipole systems, equation (3.50) simplifies considerably, as we show later in Section 3.2.3.

3.2 Examples of simple systems of interacting point emitters

In this section, we analyze in detail different point multipole resonator systems. We utilize the point dipole model reviewed in Section 2.2 and the electric quadrupole extension introduced in Section 3.1. Because we deal with point multipole resonators, we assume there is no variation in the different multipole radiative emission rates between resonators. That is: $\Gamma_{\mathrm{O},j} = \Gamma_{\mathrm{O}}$; $\Gamma_{\mathrm{E1},j} = \Gamma_{\mathrm{E1}}$; $\Gamma_{\mathrm{M1},j} = \Gamma_{\mathrm{M1}}$; and $\Gamma_{\mathrm{E2},j} = \Gamma_{\mathrm{E2}}$, for all j. Additionally, we assume that individual point electric dipoles have resonance frequency $\omega_j = \omega_0$, for all j. We show later how we determine the resonance frequency of magnetic dipole and electric quadrupole resonators.

In order to illustrate and test the point-emitter formalism, we introduce models for the interactions between effective point emitters that not only possess electric and magnetic dipoles, but also the electric quadrupole, developed in Section 3.1. After analyzing the elementary case of two point electric dipoles, we consider systems comprising two parallel pairs of point electric dipoles. When a parallel pair is symmetrically excited, it may be approximated by a single effective point emitter possessing an electric dipole located at the center of the two dipoles. For an antisymmetrically excited pair we use a single effective point emitter possessing both a magnetic dipole and electric quadrupole located at the center of the two dipoles. We denote the decay rates of the effective point emitters by $\gamma^{(1)}_{\mathrm{s,a}}$ for a symmetrically and antisymmetrically excited pair of dipoles, respectively, that depend on the separation of the dipoles within the pair.

3.2.1 Two parallel point electric dipoles

In general, the Cartesian coordinates of a two resonator system are

$$\mathbf{r}_1 = \frac{1}{2}\begin{bmatrix} s_1 \\ y_1 \\ 0 \end{bmatrix}, \quad \mathbf{r}_2 = \frac{1}{2}\begin{bmatrix} s_2 \\ y_2 \\ 0 \end{bmatrix}. \tag{3.51}$$

As the first example to illustrate our model, we take two parallel electric dipoles, see, e.g., Figure 3.1, and specifically set $s_1 = s_2 = 0$ and $|y_1 - y_2| = l$, i.e., $\mathbf{r}_1 = -\mathbf{r}_2 = [0, l/2, 0]$. The decay rate of an electric dipole,

$$\Gamma^{(1)} = \Gamma_{\mathrm{O}} + \Gamma_{\mathrm{E1}}, \tag{3.52}$$

depends on the rate of dipole radiation and nonradiative losses that we set to $\Gamma_{\mathrm{E1}} = 0.83\Gamma^{(1)}$ and $\Gamma_{\mathrm{O}} = 0.17\Gamma^{(1)}$, respectively; we justify these choices later, in Chapter 4 and Appendix F. The superscript (1) is used to denote properties relating to discrete electric dipole interactions.

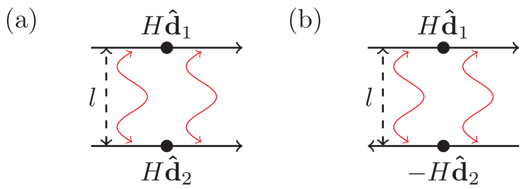

Figure 3.1: Geometry of two interacting point electric dipoles (black dots) with magnitude H and orientation vectors $\mathbf{d}_1$ and $\mathbf{d}_2$ (solid black arrows), separated by a distance l. In (a) we show the symmetric and in (b) the antisymmetric excitation.

When the driving field is tuned to the resonance frequency of the point electric dipoles, $\Omega_0 = \omega_0$, the coupling matrix in the equation of motion [equation (3.1), with $\Gamma_{\mathrm{M1}} \equiv \Gamma_{\mathrm{E2}} \equiv 0$], of a pair of electric dipoles is,

$$\mathcal{C} = \begin{bmatrix} -\frac{\Gamma^{(1)}}{2} & i\frac{3}{4}\Gamma_{\mathrm{E1}}G_{\mathrm{E1}}(\mathbf{r}_{12}) \\ i\frac{3}{4}\Gamma_{\mathrm{E1}}G_{\mathrm{E1}}(-\mathbf{r}_{12}) & -\frac{\Gamma^{(1)}}{2} \end{bmatrix}, \tag{3.53}$$

where $\Gamma^{(1)} = \Gamma_{\mathrm{O}} + \Gamma_{\mathrm{E1}}$ [see equation (3.52)], $\mathbf{r}_{12} = \mathbf{r}_2 - \mathbf{r}_1$, and $G_{\mathrm{E1}}(\mathbf{r}_{12}) = G_{\mathrm{E1}}(-\mathbf{r}_{12})$, from equation (2.5)

$$G_{\mathrm{E1}}(\mathbf{r}_{12}) = \frac{i}{3}\left[2h_0^{(1)}(kl) - h_2^{(1)}(kl)\right]. \tag{3.54}$$

Equation (3.53) has two eigenmodes of current oscillation: a symmetric mode (denoted by a subscript 's'), where both dipoles' current oscillations are in phase, i.e., $\hat{\mathbf{d}}_1 = \hat{\mathbf{d}}_2$, see Figure 3.1(a); and an antisymmetric mode (denoted by a subscript 'a'), where the current oscillations of the dipoles are out of phase, i.e., $\hat{\mathbf{d}}_1 = -\hat{\mathbf{d}}_2$, see Figure 3.1(b). The eigenvectors ($\mathbf{v}_n^{(1)}$) and corresponding eigenvalues ($\xi_n^{(1)}$) of the two modes of current oscillation are

$$\mathbf{v}_{\mathrm{s}}^{(1)} = \frac{1}{\sqrt{2}}\begin{bmatrix} 1 \\ 1 \end{bmatrix} \quad \text{and} \quad \mathbf{v}_{\mathrm{a}}^{(1)} = \frac{1}{\sqrt{2}}\begin{bmatrix} 1 \\ -1 \end{bmatrix}. \tag{3.55}$$

and

$$\xi_{\mathrm{a,s}}^{(1)} = -\frac{\Gamma^{(1)}}{2} \pm i\frac{3}{4}\Gamma_{\mathrm{E1}}G_{\mathrm{E1}}(\mathbf{r}_{12}), \tag{3.56}$$

respectively. The eigenvalues $\xi_{\mathrm{a,s}}^{(1)}$ determine the mode resonance frequency shifts $\delta\omega_{\mathrm{a,s}}^{(1)} = -(\Omega_{\mathrm{a,s}} - \Omega_0) = \mathrm{Im}(\xi_{\mathrm{a,s}}^{(1)})$, and mode decay rates $\gamma_{\mathrm{a,s}}^{(1)} = -2\mathrm{Re}(\xi_{\mathrm{a,s}}^{(1)})$, see equation (2.29). This example is important because the antisymmetric mode decay rate ($\gamma_{\mathrm{a}}^{(1)}$), and line shift ($\delta\omega_{\mathrm{a}}^{(1)}$), can be used to estimate the total decay rate and resonance frequency of a single resonator possessing both magnetic dipole and electric quadrupole moments, as we show in our next example. Similarly, the symmetric mode decay rate $\gamma_{\mathrm{s}}^{(1)}$ and line shift $\delta\omega_{\mathrm{s}}^{(1)}$ are used to estimate the total decay rate and resonance frequency of the effective electric dipole resonator obtained from two symmetrically excited point electric dipoles.

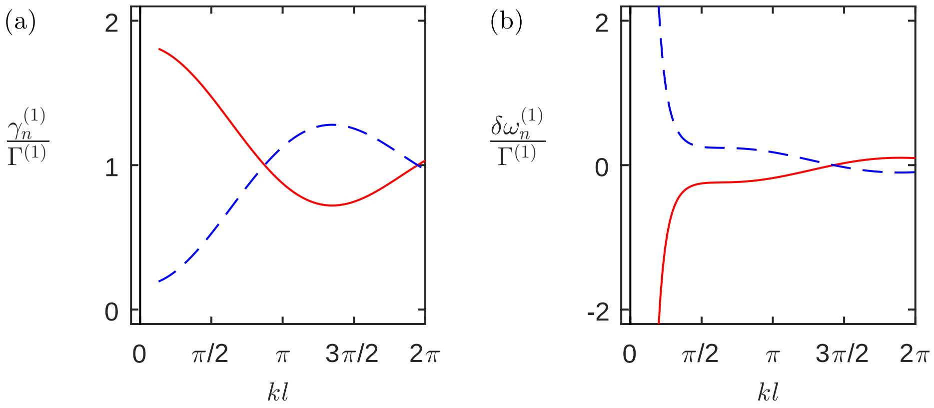

Figure 3.2: The radiative resonance linewidths (a) and line shifts (b) for the collective antisymmetric (blue dashed line) and symmetric (red solid line) eigenmodes, as a function of the separation parameter l, for two parallel point electric dipole resonators. The radiative losses of each dipole are $\Gamma_{\mathrm{E1}} = 0.83\Gamma^{(1)}$, the ohmic losses are $\Gamma_{\mathrm{O}} = 0.17\Gamma^{(1)}$.

In Figure 3.2 we show the radiative resonance linewidths and line shifts for the collective antisymmetric and symmetric eigenmodes. As the separation because small $l \to 0$, the linewidth of the antisymmetric mode approaches the ohmic loss rate ($\gamma_{\mathrm{a}}^{(1)} \to \Gamma_{\mathrm{O}}$) and is subradiant, the symmetric mode linewidth approaches $\gamma_{\mathrm{s}}^{(1)} \to 1.8\Gamma^{(1)}$ and is superradiant. At approximately $kl \approx \pi$ (where $k = 2\pi/\lambda_0$), the symmetric and antisymmetric modes become subradiant and superradiant, respectively. The line shifts of two modes are symmetric about Ω_0. At $kl \approx \pi/4$, the line shifts diverge with $\delta\omega_{\mathrm{s}}^{(1)}$ red shifted, and $\delta\omega_{\mathrm{a}}^{(1)}$ blue shifted, from Ω_0.

3.2.2 Effective point emitter for a pair of out-of-phase electric dipoles

Two closely-spaced parallel electric dipoles have eigenmodes that represent in-phase and out-of-phase excitations, equation (3.55). The in-phase oscillations of a pair of dipoles can be approximated by a single electric dipole point emitter. For the antisymmetric, out-of-phase oscillations the total electric dipole is weak, but the pair exhibits nonvanishing electric quadrupole and magnetic dipole moments, see Figure 3.3. We, therefore, approximate a pair of closely-spaced, parallel out-of-phase point electric dipoles by a single point emitter, possessing both a magnetic dipole and an electric quadrupole moment, located between the two electric dipoles.

We write the decay rate of a point emitter corresponding to the pair of out-of-phase electric dipoles as

$$\gamma_{\mathrm{a}}^{(1)} = \Gamma_{\mathrm{O}} + \Gamma_{\mathrm{M1}} + \Gamma_{\mathrm{E2}}\,, \tag{3.57}$$

where the antisymmetric collective mode linewidth $\gamma_{\mathrm{a}}^{(1)}$ of two parallel electric dipoles can be calculated and is shown in Figure 3.2. Using this formula, we may then derive analytical expressions for Γ_{M1} and Γ_{E2}.

Also shown in Figure 3.2, is the antisymmetric collective mode line shit $\delta\omega_{\mathrm{a}}^{(1)}$. The resonance frequency of the magnetic dipole and electric quadrupole resonator $\Omega_{\mathrm{a}}^{(1)}$, is related to the line shift of the antisymmetric mode of two parallel electric dipoles by

$$\Omega_{\mathrm{a}}^{(1)} = (\Omega_0 - \delta\omega_{\mathrm{a}}^{(1)})\,. \tag{3.58}$$

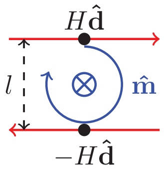

Figure 3.3: Visualization of the effective magnetic dipole moment [pointing into the page] and electric quadrupole moment, both located at the center of the blue cross, formed by two parallel antisymmetrically excited point electric dipoles (black dots), with magnitude H and orientation vectors $\pm\hat{\mathbf{d}}$ (solid red arrows), separated by a distance l.

3.2.2.1 Magnetic dipole moment of two parallel electric dipoles

In Section 2.2 and Reference 79, the magnetic dipole moment arose solely due to the magnetization $\mathbf{M}_j(\mathbf{r},t)$. Here, we assume the resonator comprises two electric dipoles with location vectors $\mathbf{r}_{\pm,j} = [x_j, \pm l_j/2, z_j]$, where $l_j \ll \lambda_0$, with linear charge and current oscillations along their axes. An effective magnetization $\mathbf{M}_{\mathrm{P},j}(\mathbf{r},t)$ is present due to the polarization of the two parallel electric dipoles, where

$$\mathbf{M}_{\mathrm{P},j}(\mathbf{r},t) = I_j(t)\bar{\mathbf{w}}_j(\mathbf{r})\,. \tag{3.59}$$

Here, $\bar{\mathbf{w}}_j(\mathbf{r})$ is the effective current profile function; also considered to be independent of time. The scattered EM fields due to the effective magnetic source located at $\mathbf{r}'$, follow from the EM fields, equations (2.3) and (2.4), with the effective magnetization equation (3.59).

In the point magnetic dipole approximation, the spatial profile function $\bar{\mathbf{w}}_j(\mathbf{r})$ of the effective magnetization is approximated as a δ function at the origin

$$\begin{aligned}\bar{\mathbf{w}}_j(\mathbf{r}) &= \frac{1}{2}\int \mathrm{d}^3r\,\mathbf{r}\times\left[\mathbf{p}_{+,j}(\mathbf{r}) + \mathbf{p}_{-,j}(\mathbf{r})\right]\\ &\approx A_{\mathrm{M},j}\hat{\mathbf{m}}_j\delta(\mathbf{r}-\mathbf{r}_j)\,.\end{aligned} \tag{3.60}$$

The rate at which this magnetic dipole radiates is Γ_{M1}, as before [see equation (2.35)]. The effective area $A_{\mathrm{M},j}$, of the point magnetic dipole [see Figure 3.3] may be approximated by evaluating equation (3.60) with $\mathbf{p}_{\pm,j}(\mathbf{r}) = \pm H\hat{\mathbf{d}}\delta(\mathbf{r}-\mathbf{r}_{\pm,j})$. We find the point magnetic dipole moment, of the jth pair of antisymmetrically excited point electric dipoles, has an effective area

$$A_{\mathrm{M},j} = \frac{l_j H_j}{2}\,. \tag{3.61}$$

The magnetic dipole decay rate is dependent upon the magnitude of the electric dipoles H_j which comprise the pair, and their separation l_j, i.e., their effective cross sectional area. It is immediately obvious from equation (3.61) that the magnetic dipole radiative emission rate disappears as the separation becomes small.

If the two electric dipoles are not extremely close to each other, the resonance frequency of the antisymmetric mode is close to that of a single isolated electric dipole. We use the same resonance frequency [equation (2.9)] in both equations (2.34) and (2.35), together with the effective area of the magnetic dipole equation (3.61), to find the ratio of the two emission rates is approximately given by

$$\Gamma_{\mathrm{M1}} = \frac{\pi^2 l_j^2}{\lambda^2}\Gamma_{\mathrm{E1}}\,. \tag{3.62}$$

3.2.2.2 Electric quadrupole moment of two parallel electric dipoles

The effective area of the point electric quadrupole is obtained from a pair of out-of-phase point electric dipoles. We compare equation (3.14) [using the charge density of the electric dipoles, i.e., $\rho_j(\mathbf{r},t) = -Q\nabla\cdot \mathbf{p}_j^{\mathrm{d}}(\mathbf{r})$], with equation (3.21), to obtain the effective area

$$A_{\alpha\beta,j} = -\sum_{\pm}\int \mathrm{d}^3r'\, r_\alpha r_\beta \frac{\partial}{\partial r_j} p_j^{\mathrm{d},\pm}(\mathbf{r}')\,, \tag{3.63}$$

where $\mathbf{r}' = \mathbf{r} - \mathbf{r}_j$ and the summation is over each of the ± orientated electric dipoles. Integrating equation (3.63) by parts results in Kronecker δ functions, see e.g., equation (3.22), and we find

$$A_{\alpha\beta,j} = \sum_{\pm}\int \mathrm{d}^3r \left[r_\beta p_{\alpha,j}^{\mathrm{d},\pm}(\mathbf{r}) + r_\alpha p_{\beta,j}^{\mathrm{d},\pm}(\mathbf{r})\right], \tag{3.64}$$

For an electric dipole pair whose separation is along the y axis, i.e., $y = l$ (see Figure 3.3), the orientation vectors $\hat{\mathbf{d}}_j^{\pm}$ of the electric dipoles are oppositely orientated and perpendicular to $\hat{\mathbf{y}}$, i.e., $\hat{\mathbf{d}}_j^{\pm} = \pm\hat{\mathbf{y}}_{\perp}$. By symmetry all elements of the tensor $A_{\alpha\beta,j}$ are zero, with the exception of $A_{y\hat{d},j} = A_{\hat{d}y,j}$. For example, let the electric dipoles be aligned along the x axis. Then, two antisymmetrically excited point electric dipoles located at $\mathbf{r}_{\pm,j} = [x_j, y_j \pm l_j/2, z_j]$, have mode functions $\mathbf{p}_j^{\mathrm{d},\pm}(\mathbf{r}) = \pm H_j\hat{\mathbf{x}}\delta(\mathbf{r}-\mathbf{r}_{\pm,j})$. The nonzero components of equation (3.64) are

$$\begin{aligned} A_{yx,j} = A_{xy,j} &= \int \mathrm{d}^3r \left[r_y p_{x,j}^{\mathrm{d},+}(\mathbf{r}) - r_y p_{x,j}^{\mathrm{d},-}(\mathbf{r})\right], \\ &= 2H_j \int \mathrm{d}^3r \left[r_y \delta(\mathbf{r}-\mathbf{r}_{+,j})\right], \end{aligned} \tag{3.65}$$

because the product $r_y\delta(\mathbf{r}-\mathbf{r}_{\pm,j})$ is even in r_y. The integral in equation (3.65) is carried out over the δ function, summing over the indices α, β in equation (3.27) provides the effective area of our point electric quadrupole

$$A_{\mathrm{E},j} = \sqrt{2} l_j H_j \,. \tag{3.66}$$

The electric quadrupole radiative emission rate also depends on the amplitudes of the point electric dipoles and their separation. If the electric dipoles are symmetrically excited, then one may readily verify the point electric quadrupole moment vanishes.

In the examples in this section, the radiative emission rates of the magnetic dipole and the electric quadrupole both depend the effective area of a pair of parallel electric dipoles. We assume that the resonance frequencies of the magnetic dipole and electric quadrupole moments of the jth source are ω_j, [equation (2.9)]. The relative decay rate of the magnetic dipole and electric quadrupole, equation (3.29), depends on the effective areas, $A_{\mathrm{M},j}$ and $A_{\mathrm{E},j}$, equations (3.61) and (3.66), respectively. We find the relative radiation rates for our example are

$$\Gamma_{\mathrm{E2}} = \frac{12}{5}\Gamma_{\mathrm{M1}} \,. \tag{3.67}$$

The radiative emission rate of an isolated point electric quadrupole may be related to the point electric dipole through equation (3.62). Equations (3.62) and (3.67) provide first approximations of the relative radiative emission rates of a pair of antisymmetrically excited electric dipoles. However, as we show in Chapter 4.2, this approximation is not accurate, particularly when the finite-size of the resonator is accounted for.

3.2.3 Two interacting pairs of point electric dipoles

In this section, we introduce two different $N = 4$ point electric dipole systems, each comprising two pairs of parallel electric dipoles. We later compare the interactions of four point electric dipoles to similar systems comprising two effective electric dipoles and separately two resonators with both magnetic dipole and electric quadrupole moments.

The regular structure of many metamaterial systems prompts the choice of two geometries. The systems we consider comprise four electric dipoles arranged such that they form: two horizontal parallel pairs, see, e.g., Figure 3.4(a); and two perpendicular parallel pairs, see, e.g., Figure 3.9(a). The separation between parallel electric dipoles is l.

When there are four discrete electric dipoles, the coupling matrix equation (3.53), increases to a 4×4 matrix. There are four collective eigenmodes of current oscillation. We classify the modes as: antisymmetric electric dipoles (E1a); antisymmetric magnetic dipole–electric quadrupoles (M1E2a); symmetric electric dipoles (E1s); and symmetric magnetic dipole–electric quadrupoles (M1E2s). In the E1a and E1s modes each parallel pair of resonators forms an effective electric dipole. However, in the E1a mode the different parallel pairs' current oscillations are out of phase, and in the E1s mode they are in phase. In the M1E2a and M1E2s modes, the different parallel pairs' current oscillations form effective magnetic dipoles. In the M1E2a mode the two parallel pairs are out of phase, in the M1E2s mode they are in phase. For the two geometries we consider, the modes: E1a; M1E2a; E1s; and M1E2s, are shown in Figures 3.4 and 3.9, for horizontal pairs and perpendicular pairs of electric dipoles, respectively.

In the remainder of this chapter, we will directly compare the E1a and E1s modes of the four point electric dipoles [denoted by a superscript (1)] to an effective electric dipole model [denoted by a superscript (2s)]. We also compare the M1E2a and M1E2s modes of the four point electric dipoles [also denoted by a superscript (1)] to an effective magnetic dipole-electric quadrupole model [denoted by a superscript (2a)].

3.2.3.1 Description of electric dipoles by two multipole point emitters

In general, the jth pair of parallel electric dipoles are located at $\mathbf{r}_{\pm,j} = [x_j, y_j \pm l/2, z_j]$. When the separation l, between parallel electric dipoles is small, the jth pair may be approximated by a single resonator located at $\mathbf{r}_j = [x_j, y_j, z_j]$. The type of resonator approximating each pair of electric dipoles depends on how each pair is excited, i.e., symmetrically or antisymmetrically excited.

When each parallel pair of electric dipoles are symmetrically excited [see, e.g., Figure 3.4(a) and 3.4(c), and Figure 3.9(a) and 3.9(c)], each pair may be approximated by a single resonator with a point electric dipole moment, located at the center of each pair. We introduced the interactions between two point electric dipoles in Section 3.2.1. We may use similar analysis to model the symmetric (E1s and E1a) collective modes of two interacting pairs of electric dipoles. The coupling matrix in this case is given by equation (3.53); with $\Gamma^{(1)} \to \gamma_{\mathrm{s}}^{(1)}$ and the driving field is tuned to the resonance frequency of the symmetrically excited pair of point electric dipoles, i.e, $\Omega_0 = \Omega_{\mathrm{s}}^{(1)}$. The eigenvectors of the effective electric dipole interaction matrix are

$$\mathbf{v}_{\mathrm{E1s}}^{(2\mathrm{s})} = \frac{1}{\sqrt{2}}\begin{bmatrix}1\\1\end{bmatrix} \quad \text{and} \quad \mathbf{v}_{\mathrm{E1a}}^{(2\mathrm{s})} = \frac{1}{\sqrt{2}}\begin{bmatrix}1\\-1\end{bmatrix}, \tag{3.68}$$

with corresponding eigenvalues $\xi_{\mathrm{E1s}}^{(2\mathrm{s})}$ and $\xi_{\mathrm{E1a}}^{(2\mathrm{s})}$, where

$$\xi_{\mathrm{E1s,E1a}}^{(2\mathrm{s})} = -\frac{\gamma_{\mathrm{s}}^{(1)}}{2} \pm \frac{3}{4}\Gamma_{\mathrm{E1}}\mathcal{G}_{\mathrm{E1}}(\mathbf{r}_{12}). \tag{3.69}$$

Here, $\mathcal{G}_{\mathrm{E1}}(\mathbf{r}_{12})$ is defined in equation (2.42), and the argument $\mathbf{r}_{12}$ depends on the locations of the effective electric dipoles.

On the other hand, we argued in Section 3.2.2 how a pair of antisymmetrically excited point electric dipoles can be approximated by a single point emitter posessing both magnetic dipole and electric quadrupole moments, see Figure 3.4(b,d) and Figure 3.9(b,d). For two point emitters located at $\mathbf{r}_1$ and $\mathbf{r}_2$, with both magnetic dipole and electric quadrupole moments (driven at the resonance frequency of the point electric dipole, i.e., $\Omega_0 = \omega_0$), the interaction matrix, $\mathcal{C}$, is

$$\mathcal{C} = \Delta' - \frac{1}{2}\Upsilon + \frac{1}{2}\left[i\mathcal{C}_{\mathrm{M1}} + i\mathcal{C}_{\mathrm{E2}} + \mathcal{C}_{\mathrm{X2}} + \mathcal{C}_{\mathrm{X2}}^{T}\right]. \tag{3.70}$$

Similar to our example of two electric dipoles, the contributing matrices in equation (3.70) are also 2×2. However, the off-diagonals elements of $\mathcal{C}$ are more complicated, and there are subtle differences in the diagonal elements. The total decay rate of each resonator is $\gamma_{\mathrm{a}}^{(1)}$, given in equation (3.57). In general, the resonance frequency $\Omega_{\mathrm{a}}^{(1)} \neq \omega_0$ [see equation (3.58)], thus Δ' is not trivial and contains a frequency shift. The matrix contributions to $\mathcal{C}$ are then

$$\Delta' = \begin{bmatrix} i\delta\omega_{\mathrm{a}}^{(1)} & 0 \\ 0 & i\delta\omega_{\mathrm{a}}^{(1)} \end{bmatrix}, \tag{3.71}$$

$$\Upsilon = \begin{bmatrix} \gamma_{\mathrm{a}}^{(1)} & 0 \\ 0 & \gamma_{\mathrm{a}}^{(1)} \end{bmatrix}, \tag{3.72}$$

$$\mathcal{C}_{\mathrm{M1}} = \Gamma_{\mathrm{M1}} \begin{bmatrix} 0 & G_{\mathrm{M1}}(\mathbf{r}_{12}) \\ G_{\mathrm{M1}}(\mathbf{r}_{12}) & 0 \end{bmatrix}, \tag{3.73}$$

$$\mathcal{C}_{\mathrm{E2}} = \Gamma_{\mathrm{E2}} \begin{bmatrix} 0 & G_{\mathrm{E2}}(\mathbf{r}_{12}) \\ G_{\mathrm{E2}}(\mathbf{r}_{12}) & 0 \end{bmatrix}, \tag{3.74}$$

$$\mathcal{C}_{\mathrm{X2}} = \sqrt{\Gamma_{\mathrm{M1}}\Gamma_{\mathrm{E2}}} \begin{bmatrix} 0 & G_{\mathrm{X2}}(\mathbf{r}_{12}) \\ G_{\mathrm{X2}}(\mathbf{r}_{12}) & 0 \end{bmatrix}, \tag{3.75}$$

where $G_{\mathrm{M1}}(\mathbf{r}_{12})$, $G_{\mathrm{E2}}(\mathbf{r}_{12})$ and $G_{\mathrm{X2}}(\mathbf{r}_{12})$ depend exclusively on the orientations and locations of the magnetic dipoles and electric quadrupoles and we have utilized the symmetry property of the matrices, e.g., $[\mathcal{C}_{\mathrm{M1}}]_{i,j} = [\mathcal{C}_{\mathrm{M1}}]_{j,i}$, etc, and again, $\mathbf{r}_{12} = \mathbf{r}_2 - \mathbf{r}_1$. The eigenvectors $\mathbf{v}_n^{(2\mathrm{a})}$ of equation (3.70) are independent of the resonator locations, and correspond to symmetric and antisymmetric oscillations,

$$\mathbf{v}_{\mathrm{M1E2s}}^{(2\mathrm{a})} = \frac{1}{\sqrt{2}}\begin{bmatrix} 1 \\ 1 \end{bmatrix} \quad \text{and} \quad \mathbf{v}_{\mathrm{M1E2a}}^{(2\mathrm{a})} = \frac{1}{\sqrt{2}}\begin{bmatrix} 1 \\ -1 \end{bmatrix}. \tag{3.76}$$

However, the eigenvalues ($\xi_n^{(2\mathrm{a})}$) of equation (3.70) depend on both the orientations and locations of the resonators. In the following section, we analyze in detail the point magnetic dipole and electric quadrupole interacting systems, utilizing the geometries introduced in Figures 3.4 and 3.9.

3.2.3.2 Two horizontal pairs of point electric dipoles

When the point electric dipoles are arranged in horizontal pairs, the Cartesian coordinations of each electric dipole are

$$\mathbf{r}_{1,2} = \frac{1}{2}\begin{bmatrix} s \\ \pm l \\ 0 \end{bmatrix}, \quad \mathbf{r}_{3,4} = \frac{1}{2}\begin{bmatrix} -s \\ \pm l \\ 0 \end{bmatrix}. \tag{3.77}$$

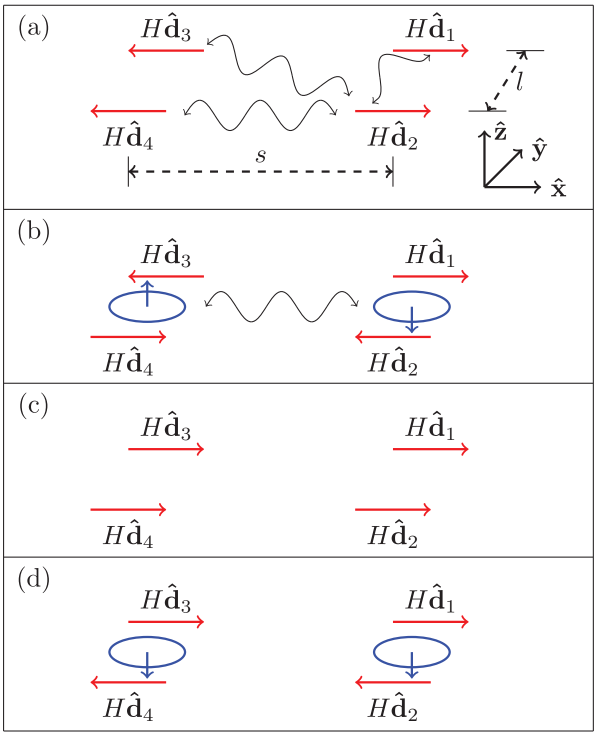

Figure 3.4: Schematic illustration of the eigenmodes of two horizontal pairs of parallel electric dipoles. The red arrows indicate the electric dipole orientation vectors, the blue loops with blue arrows effective magnetic dipole moments. The separation between parallel pairs is l and the position of the dipole on an axis perpendicular to the y-axis is determined by s. We show the mode classifications: (a) E1a; (b) M1E2a; (c) E1s; and (d) M1E2s. In (a) the three black wave lines represent the interactions of one electric dipole with the other three electric dipoles. In (b) the single black wave line represents the interaction of two resonators with effective magnetic dipole and electric quadrupole moments.

In Figure 3.4(a) and 3.4(c), we show the E1a and E1s modes of two horizontal pairs of point electric dipoles. The E1a and E1s modes can be approximated by two effective electric dipoles located at the center of each pair. In Figure 3.4(b) and 3.4(d), we show the antisymmetric excitation of the parallel pairs of electric dipoles, i.e., the M1E2a and M1E2s modes, respectively. We demonstrated in Section 3.2.2, that each antisymmetrically excited pair can be approximated by a single resonator with both a point magnetic dipole and point electric quadrupole moment. The resonators with magnetic dipole and electric quadrupole moments, (and the effective electric dipole resonators) are located at $\mathbf{r}_1 = -\mathbf{r}_2 = [s/2, 0, 0]$.

The interaction terms: $G_{\mathrm{M1}}(\mathbf{r}_{12})$; $G_{\mathrm{E2}}(\mathbf{r}_{12})$; and $G_{\mathrm{X2}}(\mathbf{r}_{12})$, in equations (3.73)–(3.75), are given by

$$G_{\mathrm{M1}}(\mathbf{r}_{12}) = \frac{i}{2}\left[2h_0^{(1)}(ks) - h_2^{(1)}(ks)\right] , \tag{3.78}$$

$$G_{\mathrm{E2}}(\mathbf{r}_{12}) = -i\frac{5}{2}\left[\frac{16}{35}h_4^{(1)}(ks) - \frac{3}{7}h_2^{(1)}(ks) + \frac{2}{5}h_0^{(1)}(ks)\right] , \tag{3.79}$$

$$G_{\mathrm{X2}}(\mathbf{r}_{12}) = -\sqrt{\frac{15}{2}}h_2^{(1)}(ks) , \tag{3.80}$$

respectively. In this example, the eigenmodes correspond to antisymmetric excitations ($\hat{\mathbf{m}}_1 = -\hat{\mathbf{m}}_2$, and $\hat{A}_{\alpha\beta,1} = -\hat{A}_{\alpha\beta,2}$), see Figure 3.4(b), and symmetric excitations of the resonators ($\hat{\mathbf{m}}_1 = \hat{\mathbf{m}}_2$, and $\hat{A}_{\alpha\beta,1} = \hat{A}_{\alpha\beta,2}$), see Figure 3.4(d). These eigenmodes are represented by the eigenvectors $\mathbf{v}^{(2\mathrm{a})}_{\mathrm{M1E2a}}$ and $\mathbf{v}^{(2\mathrm{a})}_{\mathrm{M1E2s}}$, respectively, given in equation (3.76). The eigenvalues $\xi^{(2\mathrm{a})}_{\mathrm{M1E2a}}$ and $\xi^{(2\mathrm{a})}_{\mathrm{M1E2s}}$, of equation (3.75) with equations (3.78)–(3.80), are complicated and include contributions from $h_4^{(1)}(ks)$, $h_2^{(1)}(ks)$, and $h_0^{(1)}(ks)$. In the leading order expansion of the spherical Hankel functions, the real and imaginary parts of $\xi^{(2\mathrm{a})}_{\mathrm{M1E2a}}$ and $\xi^{(2\mathrm{a})}_{\mathrm{M1E2s}}$ are dominated by $h_0^{(1)}(ks)$ and $h_4^{(1)}(ks)$, respectively. Specifically, we find:

$$\gamma^{(2\mathrm{a})}_{\mathrm{M1E2a}} = \mathrm{Re}\big(\xi^{(2\mathrm{a})}_{\mathrm{M1E2a}}\big) \approx -\frac{\gamma_{\mathrm{a}}^{(1)}}{2} + \frac{1}{2}\Big[\Gamma_{\mathrm{M1}} + \Gamma_{\mathrm{E2}}\Big] , \tag{3.81a}$$

$$\gamma^{(2\mathrm{a})}_{\mathrm{M1E2s}} = \mathrm{Re}\big(\xi^{(2\mathrm{a})}_{\mathrm{M1E2s}}\big) \approx -\frac{\gamma_{\mathrm{a}}^{(1)}}{2} - \frac{1}{2}\Big[\Gamma_{\mathrm{M1}} + \Gamma_{\mathrm{E2}}\Big] , \tag{3.81b}$$

$$\delta\omega^{(2\mathrm{a})}_{\mathrm{M1E2a}} = \mathrm{Im}\big(\xi^{(2\mathrm{a})}_{\mathrm{M1E2a}}\big) \approx \delta\omega_{\mathrm{a}}^{(1)} - \frac{240}{(ks)^5}\Gamma_{\mathrm{E2}} , \tag{3.81c}$$

$$\delta\omega^{(2\mathrm{a})}_{\mathrm{M1E2s}} = \mathrm{Im}\big(\xi^{(2\mathrm{a})}_{\mathrm{M1E2s}}\big) \approx \delta\omega_{\mathrm{a}}^{(1)} + \frac{240}{(ks)^5}\Gamma_{\mathrm{E2}} . \tag{3.81d}$$

Here, we have the antisymmetric collective mode decay rate $\gamma^{(2\mathrm{a})}_{\mathrm{M1E2a}}$ is subradiant approaching Γ_{O}, while the symmetric excitation is superradiant with $\gamma^{(2\mathrm{a})}_{\mathrm{M1E2s}}$ approaching $2\gamma_{\mathrm{a}}^{(1)}$. When the resonators are close together, the line shifts of the collective modes are dominated by Γ_{E2} and quickly diverge, with $\delta\omega^{(2\mathrm{a})}_{\mathrm{M1E2a}}$ red shifted, and $\delta\omega^{(2\mathrm{a})}_{\mathrm{M1E2s}}$ blue shifted, from $\delta\omega_{\mathrm{a}}^{(1)}$.

In Figures 3.5 and 3.6, we show how the collective mode linewidths and line shifts, respectively, for the $N = 4$ interacting point electric dipoles vary with the separation of

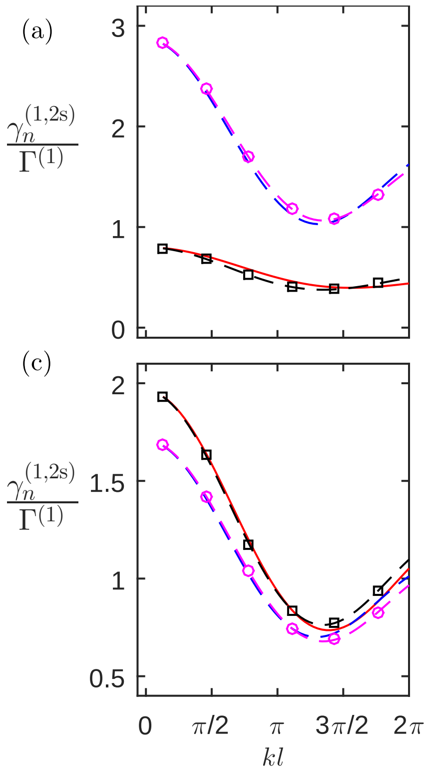

Figure 3.5: The radiative resonance linewidth $\gamma_n^{(1,2s,2a)}$ for the collective eigenmodes as a function of the separation of dipoles within each pair l, for two horizontal pairs of point electric dipoles, with: (a) and (b) $ks = 2\pi/3$; and (c) and (d) $ks = 2\pi$. We show the linewidth $\gamma_n^{(1)}$ in the $N = 4$ point electric dipole model, with the different modes shown as: E1a–red solid line (a) and (c); E1s–blue dashed line (a) and (c); M1E2a–red solid line (b) and (d); and M1E2s–blue dashed line (b) and (d). We show the linewidth $\gamma_n^{(2s)}$ in the $N = 2$ effective electric dipole resonator model: antisymmetric (E1a) excitations–magenta dash circles (a) and (c); and symmetric (E1s) excitations–black dash squares (a) and (c). The linewidth $\gamma_n^{(2a)}$ in the $N = 2$ effective magnetic dipole–electric quadrupole resonator model: antisymmetric (M1E2a) excitations–magenta dash circles (b) and (d); and symmetric (M1E2s) excitations–black dash squares (b) and (d). The radiative losses of each electric dipole are $\Gamma_{\text{E1}} = 0.83\Gamma^{(1)}$, the ohmic losses are $\Gamma_{\text{O}} = 0.17\Gamma^{(1)}$.

dipoles within each pair l, when $ks = 2\pi/3$ and $ks = 2\pi$. Also, in Figures 3.5 and 3.6, we show the collective mode linewidths and line shifts for the effective $N = 2$ interacting (magnetic dipole and electric quadrupole, and electric dipole) point multipole resonators.

When l is varied, the line widths $\gamma_n^{(2s,2a)}$ of the $N = 2$ effective resonators closely approximate the corresponding linewidths $\gamma_n^{(1)}$ of the $N = 4$ point electric dipoles; both when $ks = 2\pi/3$ and $ks = 2\pi$. When s is small [$ks = 2\pi/3$, see Figure 3.5(a) and 3.5(b)], the E1s mode is always superradiant, while both the E1a and M1E2a modes are always subradiant. When s is small, the M1E2s mode exhibits both superradiant and subradiant behavior. For large $kl \gtrsim \pi/2$, we have superradiant behavior $\gamma_{\text{M1E2s}}^{(1)} > \Gamma^{(1)}$ and $kl \lesssim \pi/2$, subradiant behavior; $\gamma_{\text{M1E2s}}^{(1)} < \Gamma^{(1)}$. The maximum (minimum) linewidths of the M1E2s

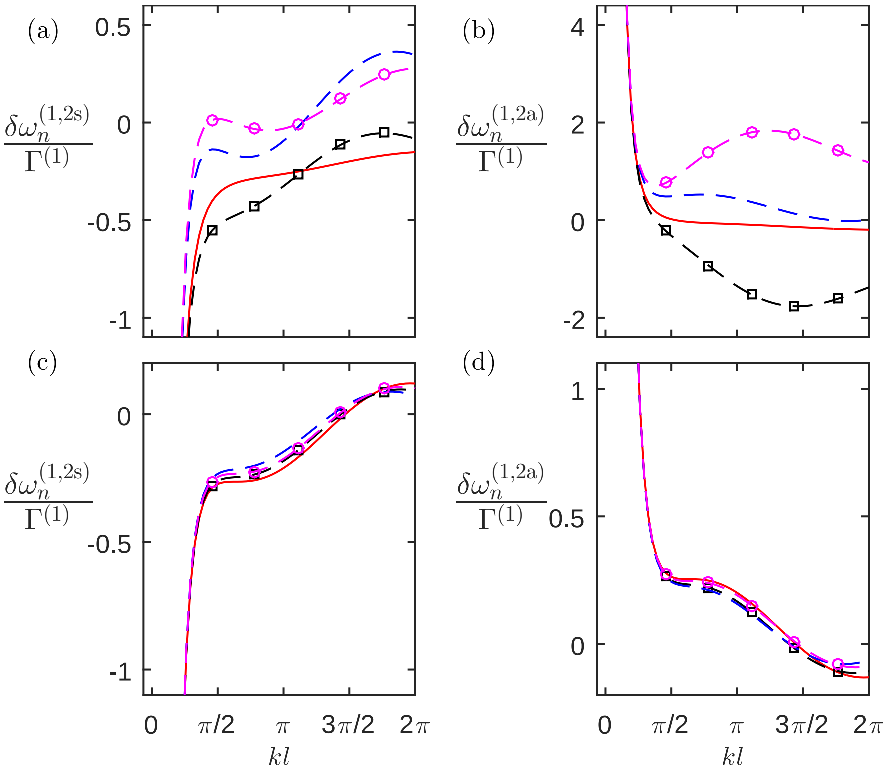

Figure 3.6: The radiative resonance line shift $\delta\omega_n^{(1,2s,2a)}$ for the collective eigenmodes as a function of the separation parameter l, for two horizontal pairs of point electric dipoles, with: (a) and (b) $ks = 2\pi/3$; and (c) and (d) $ks = 2\pi$. For plot descriptions, see Figure 3.5 caption.

(E1s) modes (when $ks = 2\pi/3$) occur at $kl \simeq 5\pi/4$, with $\gamma^{(1)}_{\rm M1E2s} \simeq 2\Gamma^{(1)}$ [$\gamma^{(1)}_{\rm E1s} \simeq 1.1\Gamma^{(1)}$]. When s is large [$ks = 2\pi$, see Figure 3.5(c) and 3.5(d)], all the linewidths exhibit both superradiant and subradiant behavior. The E1s and E1a modes are superradiant for $kl \lesssim \pi$ and subradiant for $kl \gtrsim \pi$. Conversely, the M1E2a and M1E2s modes are subradiant for $kl \lesssim \pi$ and superradiant for $kl \gtrsim \pi$.

While the collective mode linewidths resulting from the effective resonator interactions qualitatively match those of the electric dipole interactions as l varies at both large and small s, the corresponding line shifts show greater variations. In particular, when $ks = 2\pi/3$, see Figure 3.6(a) and 3.6(b), the collective line shifts $\delta\omega^{(2a)}_{\rm M1E2a}$ and $\delta\omega^{(2a)}_{\rm M1E2s}$ begin to deviate from the corresponding line shifts $\delta\omega^{(1)}_{\rm M1E2a}$ and $\delta\omega^{(1)}_{\rm M1E2s}$, when $kl \simeq \pi/4$. When $kl \simeq \pi/4$, all the collective mode line shifts begin to significantly diverge as l reduces further. In contrast, the E1a and E1s line shifts of the point electric dipole model qualitatively agree with the corresponding shifts of the effective multipole resonator model. When s is large and l is varied, there is no significant difference in the line shifts, even when l is large. As we reduce the separation l, the line shifts $\delta\omega^{(1)}_{\rm E1a}$ and $\delta\omega^{(1)}_{\rm E1s}$ are red shifted from Ω_0, see Figure 3.6(a) and 3.6(c). In contrast, $\delta\omega^{(1)}_{\rm M1E2a}$ and $\delta\omega^{(1)}_{\rm M1E2s}$ are blue shifted, see Figure 3.6(b) and 3.6(d).

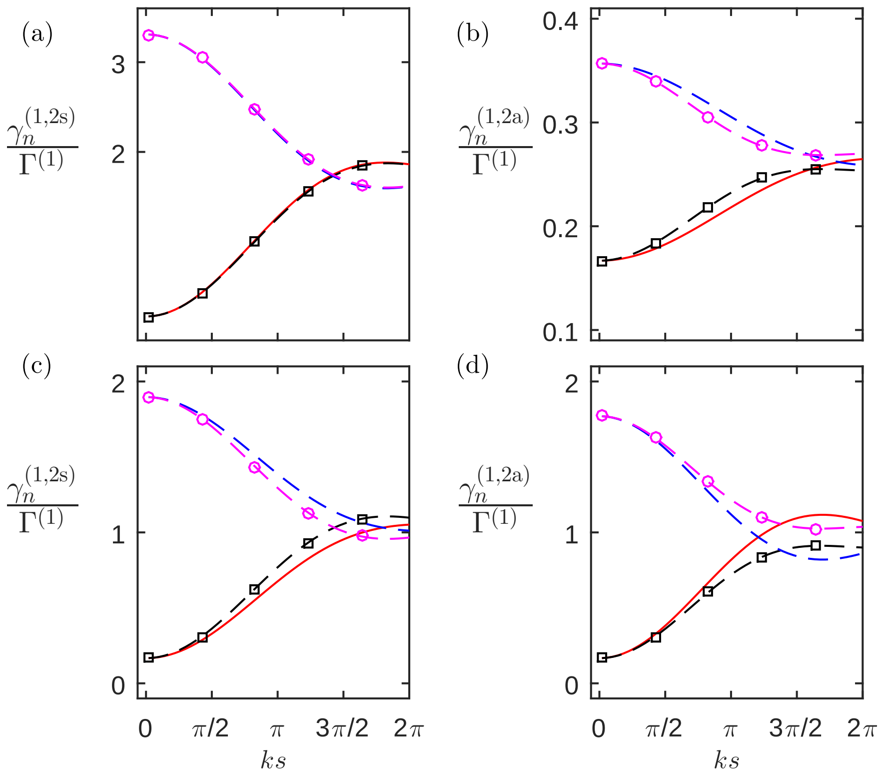

Figure 3.7: The radiative resonance linewidth $\gamma_n^{(1,2s,2a)}$ for the collective eigenmodes as a function of the separation parameter s, for two horizontal pairs of point electric dipoles, with: (a) and (b) $kl = \pi/4$; and (c) and (d) $kl = 2\pi$. For plot descriptions, see Figure 3.5 caption.

In Figures 3.7 and 3.8, we show how the collective mode linewidths and line shifts, respectively, for the $N = 4$ interacting point electric dipoles vary with the parameter s, when $kl = \pi/4$ and $kl = 2\pi$. Also, in Figures 3.7 and 3.8, we show the collective mode linewidths and line shifts for the effective $N = 2$ interacting (magnetic dipole and electric quadrupole, and electric dipole) point multipole resonators.

As s varies, both when $kl = \pi/4$ and $kl = 2\pi$, the linewidths of the collective E1a and E1s modes of four electric dipoles qualitatively agree with the corresponding linewidths of the effective electric dipoles ($\gamma_{\mathrm{n}}^{(2s)} \simeq \gamma_{\mathrm{s}}^{(1)}$). The linewidth $\gamma_{\mathrm{E1s}}^{(1)}$ is always superradiant: when l is small, $\gamma_{\mathrm{E1s}}^{(1)} \simeq 3.2\Gamma^{(1)}$ as s approaches zero, and $\gamma_{\mathrm{E1s}}^{(1)} \simeq 1.6\Gamma^{(1)}$ as $ks \simeq 2\pi$; and when l is large, we find $\gamma_{\mathrm{E1s}}^{(1)} \simeq 2\Gamma^{(1)}$ as s approaches zero, and $\gamma_{\mathrm{E1s}}^{(1)} \simeq \Gamma^{(1)}$.

When l is small, the M1E2a and M1E2s collective mode linewidths are always subradiant, and there is no significant difference in the different models, see Figure 3.7(b). The maximum linewidth here is when s approaches zero and $\gamma_{\mathrm{M1E2s}}^{(1)} = \gamma_{\mathrm{M1E2s}}^{(2a)} \simeq 0.4\Gamma^{(1)}$. The minimum is also when s approaches zero and $\gamma_{\mathrm{M1E2s}}^{(1)} = \gamma_{\mathrm{M1E2s}}^{(2a)} \simeq \Gamma_{\mathrm{O}}$. Here, also, the radiative decay of effective magnetic dipole–electric quadrupole resonator is minimal, $\gamma_{\mathrm{a}}^{(1)} \approx \Gamma_{\mathrm{O}}$, see Figure 3.2.

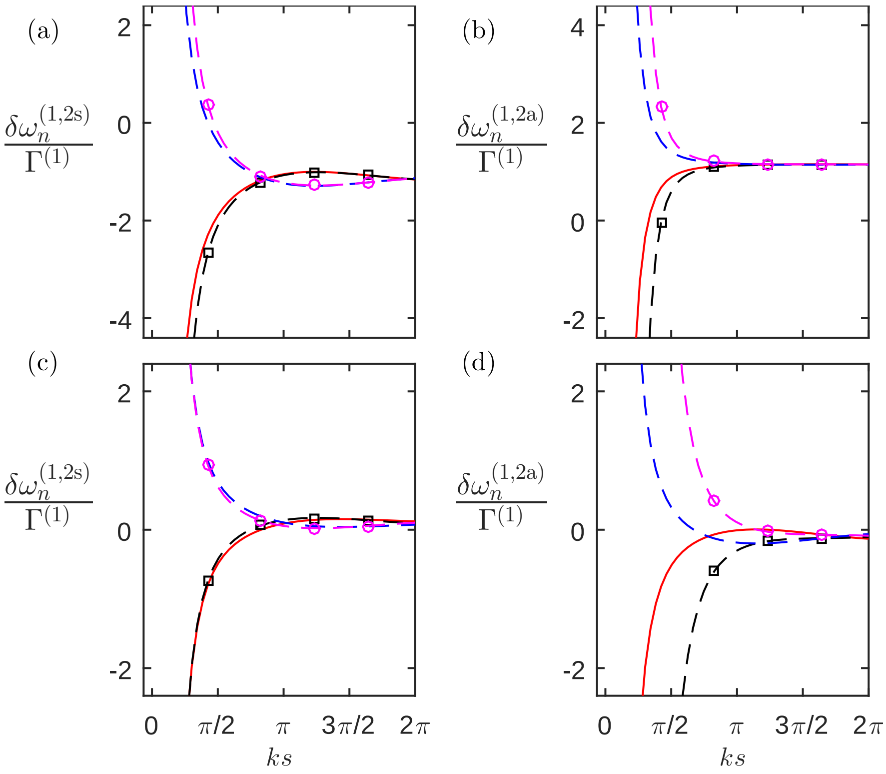

Figure 3.8: The radiative resonance line shift $\delta\omega_n^{(1,2s,2a)}$ for the collective eigenmodes as a function of the separation parameter s, for two horizontal pairs of point electric dipoles, with: (a) and (b) $kl = \pi/4$; and (c) and (d) $kl = 2\pi$. For plot descriptions, see Figure 3.6 caption.

When l is large, the M1E2s is superradiant for small s, only becoming subradiant when $ks \gtrsim \pi$. Here, the radiative decay of the magnetic dipole–electric quadrupole resonator is large, $\gamma_a^{(1)} \simeq \gamma_s^{(1)} \simeq \Gamma^{(1)}$, see Figure 3.2. At $ks \simeq 3\pi/4$, the collective mode linewidths of the effective magnetic dipole–electric quadrupole model deviate from those of the electric dipole model as s increases, see Figure 3.7(d).

In Figure 3.8, we show the line shifts of the different collective modes as s varies. The line shifts $\delta\omega_{\mathrm{E1a}}^{(2s)}$ and $\delta\omega_{\mathrm{E1s}}^{(2s)}$, show no significant deviation from the E1a and E1s modes, even at small s and $kl = \pi/4$. In contrast, the line shifts $\delta\omega_{\mathrm{M1E2a}}^{(2a)}$ and $\delta\omega_{\mathrm{M1E2s}}^{(2a)}$ begin to deviated from the M1E2a and M1E2s line shifts when $ks \simeq \pi/2$ (when $kl = \pi/4$), and $ks \simeq \pi$ (when $kl = 2\pi$). When s becomes small, the line shifts $\delta\omega_{\mathrm{E1s}}^{(2s)}$ and $\delta\omega_{\mathrm{M1E2s}}^{(2a)}$ are blue shifted from Ω_0 and $\delta\omega_{\mathrm{E1a}}^{(2s)}$ and $\delta\omega_{\mathrm{M1E2a}}^{(2a)}$ are red shifted.

3.2.3.3 Two perpendicular pairs of point electric dipoles

Our second example is two perpendicular pairs of point electric dipoles. The Cartesian coordinates of each electric dipole are

$$\mathbf{r}_{1,2} = \begin{bmatrix} s \\ \pm\dfrac{l}{2} \\ 0 \end{bmatrix}, \quad \mathbf{r}_{3,4} = \begin{bmatrix} 0 \\ \pm\dfrac{l}{2} \\ s \end{bmatrix}. \tag{3.82}$$

In Figure 3.9(a) and 3.9(c), we show the E1a and E1s modes, respectively. In Figure 3.9(b) and 3.9(d), we show the M1E2a and M1E2s modes, respectively. The locations vectors of the effective resonators with both point magnetic dipole and point electric quadrupole sources [and effective electric dipole sources] are $\mathbf{r}_1 = [s, 0, 0]$ and $\mathbf{r}_2 = [0, 0, s]$.

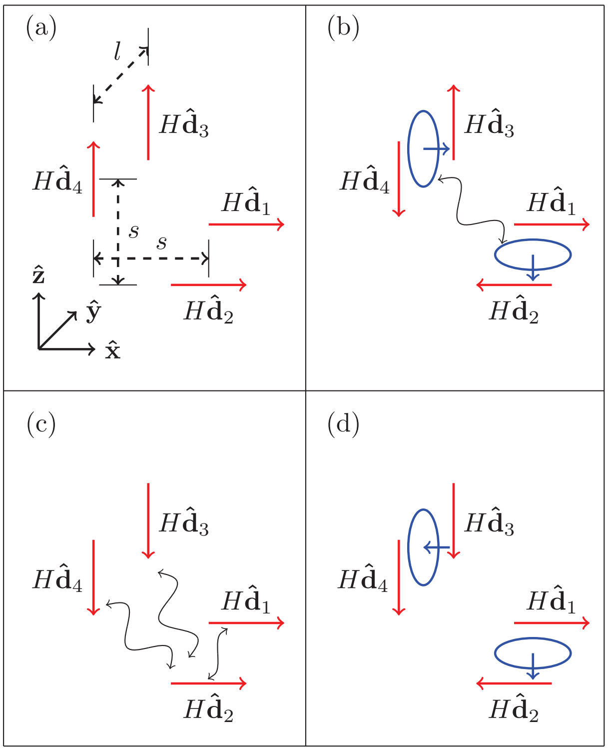

Figure 3.9: A representation of the eigenmodes of four perpendicular electric dipoles. The red arrows indicate the electric dipole orientation vectors, the blue arrows effective magnetic dipole moments. The separation between parallel pairs is l and the position of the dipole on an axis perpendicular to the y-axis is determined by s. We show the mode classifications: E1a (a); M1E2a (b); E1s (c); and M1E2s (d). In (b) the three black wave lines represent the interactions of one electric dipole with the other three electric dipoles. In (c) the single black wave line represent the interaction between single resonators with effective magnetic dipole and electric quadrupole moments.

In this example, the magnetic dipole orientation vectors $\hat{\mathbf{m}}_{1,2}$ and the unit vector $\hat{\mathbf{k}}$ form an orthonormal set, i.e., $\hat{\mathbf{m}}_1 = \pm\hat{\mathbf{k}} \times \hat{\mathbf{m}}_2$, corresponding to symmetric (+) and antisymmetric (−) oscillations, see Figure 3.9(d), and 3.9(b), respectively. Similarly, the electric quadrupole unit tensors, for the symmetric (+) and antisymmetric (−) excitations are

$$\hat{A}_1 = \begin{bmatrix} 0 & 1 & 0 \\ 1 & 0 & 0 \\ 0 & 0 & 0 \end{bmatrix} \quad \text{and} \quad \hat{A}_2 = \pm \begin{bmatrix} 0 & 0 & 0 \\ 0 & 0 & 1 \\ 0 & 1 & 0 \end{bmatrix} . \tag{3.83}$$

These oscillations are represented through the eigenvectors $\mathbf{v}^{(2a)}_{\mathrm{M1E2s}}$ and $\mathbf{v}^{(2a)}_{\mathrm{M1E2s}}$, respectively, see equation (3.76). The interaction terms: $G_{\mathrm{M1}}(\mathbf{r}_{12})$; $G_{\mathrm{E2}}(\mathbf{r}_{12})$; and $G_{\mathrm{X2}}(\mathbf{r}_{12})$, in equations (3.73)–(3.75), respectively, in this case are given by

$$G_{\mathrm{M1}}(\mathbf{r}_{12}) = i\frac{3}{4}h_2^{(1)}(\sqrt{2}ks)\,, \tag{3.84}$$

$$G_{\mathrm{E2}}(\mathbf{r}_{12}) = i\frac{20}{28}\left[h_4^{(1)}(\sqrt{2}ks) - \frac{3}{4}h_2^{(1)}(\sqrt{2}ks)\right], \tag{3.85}$$

$$G_{\mathrm{X2}}(\mathbf{r}_{12}) = -\sqrt{\frac{15}{4}}h_2^{(1)}(\sqrt{2}ks)\,. \tag{3.86}$$

The eigenvalues ($\xi^{(2a)}_{\mathrm{M1E2a}}$ and $\xi^{(2a)}_{\mathrm{M1E2s}}$) of equation (3.75), with equations (3.84)–(3.86) are complex, involving contributions from $h_4^{(1)}(\sqrt{2}ks)$ and $h_2^{(1)}(\sqrt{2}ks)$. For analytical expressions of $\xi^{(2a)}_{\mathrm{M1E2a}}$ and $\xi^{(2a)}_{\mathrm{M1E2s}}$, we again consider the leading order expansions of the spherical Hankel functions. In this limit $\mathrm{Im}(\xi^{(2a)}_{\mathrm{n}})$ is dominated by $h_4^{(1)}(\sqrt{2}ks)$ and $\mathrm{Re}(\xi^{(2a)}_{\mathrm{n}})$ by $h_2^{(1)}(\sqrt{2}ks)$. Specifically, we find

$$\delta\omega^{(2a)}_{\mathrm{M1E2a}} = \mathrm{Im}\big(\xi^{(2a)}_{\mathrm{M1E2a}}\big) \approx \delta\omega^{(1)}_{\mathrm{a}} + \frac{1125}{(\sqrt{2}ks)^5}\Gamma_{\mathrm{E2}}\,, \tag{3.87a}$$

$$\delta\omega^{(2a)}_{\mathrm{M1E2s}} = \mathrm{Im}\big(\xi^{(2a)}_{\mathrm{M1E2s}}\big) \approx \delta\omega^{(1)}_{\mathrm{a}} - \frac{1125}{(\sqrt{2}ks)^5}\Gamma_{\mathrm{E2}}\,, \tag{3.87b}$$

$$\gamma^{(2a)}_{\mathrm{M1E2a}} = \mathrm{Re}\big(\xi^{(2a)}_{\mathrm{M1E2a}}\big) \approx -\frac{\gamma^{(1)}_{\mathrm{a}}}{2} + \left[\frac{\Gamma_{\mathrm{M1}}}{10} + \frac{\Gamma_{\mathrm{E2}}}{28} + \sqrt{\frac{15}{4}}\sqrt{\Gamma_{\mathrm{M1}}\Gamma_{\mathrm{E2}}}\right](\sqrt{2}ks)^2\,, \tag{3.87c}$$

$$\gamma^{(2a)}_{\mathrm{M1E2s}} = \mathrm{Re}\big(\xi^{(2a)}_{\mathrm{M1E2s}}\big) \approx -\frac{\gamma^{(1)}_{\mathrm{a}}}{2} - \left[\frac{\Gamma_{\mathrm{M1}}}{10} + \frac{\Gamma_{\mathrm{E2}}}{28} - \sqrt{\frac{15}{4}}\sqrt{\Gamma_{\mathrm{M1}}\Gamma_{\mathrm{E2}}}\right](\sqrt{2}ks)^2\,. \tag{3.87d}$$

When the dipoles are close and perpendicular, they interact only weakly, $\gamma^{(2a)}_{\mathrm{M1E2a}} \approx \gamma^{(2a)}_{\mathrm{M1E2s}} \approx \gamma^{(1)}_{\mathrm{a}}$. The resonance line shifts of the modes diverge as $ks \to 0$ and are dominated by Γ_{E2}, with $\delta\omega^{(2a)}_{\mathrm{M1E2a}}$ blue shifted and $\delta\omega^{(2a)}_{\mathrm{M1E2s}}$ red shifted from $\delta\omega^{(1)}_{\mathrm{a}}$. When s is fixed and we vary the separation l between electric dipoles, the resonance frequency line shifts are again dominated by $\delta\omega^{(1)}_{\mathrm{a}}$.

When we vary the parameter l for perpendicular pairs of resonators, we find the collective mode linewidths and line shifts behave similar to those collective mode widths and shifts of horizontal pairs. We show plots in Appendix E (for ease of reading) showing how the collective mode linewidths and line shifts, respectively, for the $N = 4$ interacting point electric dipoles vary with the parameter l, when $ks = 2\pi/3$ and $ks = 2\pi$, for two perpendicular pairs. These are shown in Figures E.1 and E.2, respectively, where we also show the linewidths and line shifts resulting from $N = 2$ interacting effective (electric dipoles and magnetic dipole and electric quadrupole) point multipole resonators.

When $ks = 2\pi/5$, and l is varied, the linewidths of all the collective modes of perpendicular pairs, closely resemble the linewidths of the corresponding horizontal pairs, see Figures 3.5(c) and 3.5(d), and Figures E.1(a) and E.1(b). There is no significant difference in the line widths between the two different models, even when s is small. Both the E1a and E1s modes exhibit superradiant behavior when $kl \lesssim \pi$ and subradiant behavior for $\pi \lesssim kl \lesssim 2\pi$. The M1E2a and M1E2s modes also exhibit different radiative behavior, superradiant for $\pi \lesssim kl \lesssim 2\pi$ and subradiant for $kl \lesssim \pi$.

The collective mode decay rates of two pairs of perpendicular electric dipoles exhibit similar characteristics to those of two horizontal pairs of electric dipoles, only when the horizontal pairs have large separations s. In contrast, the line shifts of the perpendicular pairs have very similar characteristics to horizontal pairs, both when s is large and when s is small see Figures 3.6 and E.2. When $ks = 2\pi/3$, the line shifts $\delta\omega^{(2a)}_{\mathrm{M1E2a}}$ and $\delta\omega^{(2a)}_{\mathrm{M1E2s}}$ begin to deviate from $\delta\omega^{(1)}_{\mathrm{M1E2a}}$ and $\delta\omega^{(1)}_{\mathrm{M1E2s}}$ at $kl \simeq \pi/2$. As the separation parameter s increases, the influence of l on the line shift significantly decreases. Like the horizontal pairs, the line shifts of the E1a and E1s modes are red shifted from Ω_0 and the M1E2a and M1E2s modes blue shifted, when l is varied.

In Figure 3.10, we show how the linewidths vary with the parameter s, when $kl = \pi/4$ and $kl = 2\pi$, for $N = 4$ interacting point perpendicular electric dipoles. We also show in Figure 3.10 the corresponding linewidths for the $N = 2$ effective (electric dipole and magnetic dipole and electric quadrupole) point multipole resonators. These linewidths notably differ from the corresponding horizontal collective mode linewidths.

When we vary s, the perpendicular dipoles collective mode linewidths exhibit different characteristic behavior to those of horizontal dipoles. When $kl = \pi/4$, and s varies, the collective mode linewidths of the effective multipole model provides a good approximation of the corresponding point electric dipole model linewidths. Both the E1a and E1s modes only exhibit superradiant behavior when l is small, with $\gamma^{(1)}_{\mathrm{E1a}}$ and $\gamma^{(1)}_{\mathrm{E1s}}$ oscillating about $1.5\Gamma^{(1)}$, see Figure 3.10(a). Conversely, the M1E2a and M1E2s modes only exhibit subradiant behavior, $\gamma^{(1)}_{\mathrm{M1E2a}} \simeq \gamma^{(1)}_{\mathrm{M1E2s}} \simeq 0.5\Gamma^{(1)}$, see Figure 3.10(b). When $l = \lambda_0$, the collective modes of the electric dipole model exhibit both superradiant and subradiant behaviour, now $\gamma^{(1)}_{\mathrm{E1a}}$ and $\gamma^{(1)}_{\mathrm{E1s}}$ oscillate about $\Gamma^{(1)}$, see Figure 3.10(c). The $N = 2$ effective point electric dipole collective mode linewidths effectively approximate the $N = 4$ point electric dipole collective mode linewidths throughout the range of s. In contrast, the $N = 2$ effective magnetic dipole and electric quadrupole resonator collective mode

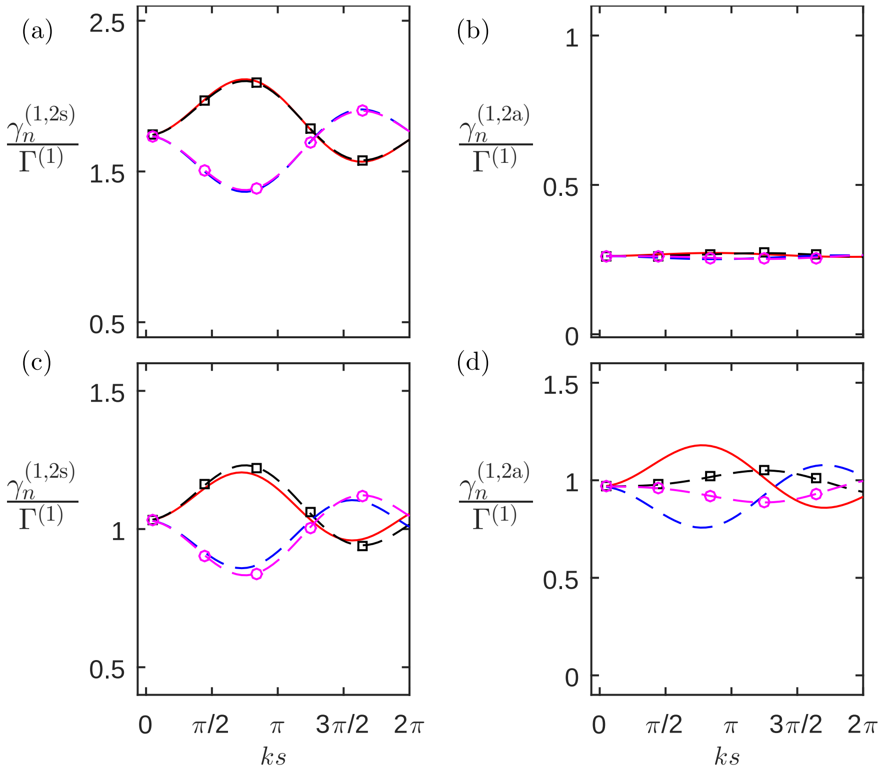

Figure 3.10: The radiative resonance linewidth γ for the collective eigenmodes as a function of the separation parameter s, for two perpendicular pairs of point electric dipoles, with: (a) and (b) $kl = \pi/4$; and (c) and (d) $kl = 2\pi$. For plot descriptions, see Figure 3.5 caption.

linewidths deviate from the $N = 4$ electric dipoles even when $ks \ll \pi/2$. Here, also $\gamma^{(1)}_{\mathrm{M1E2a}}$ and $\gamma^{(1)}_{\mathrm{M1E2s}}$ oscillation about $\Gamma^{(1)}$.

While the linewidths for perpendicular pairs have different characteristics from the horizontal pairs, the corresponding line shifts are very similar. We show the line shifts for perpendicular pairs in Appendix E, see Figure E.3. The line shifts $\delta\omega^{(2s)}_{\mathrm{E1a}}$ and $\delta\omega^{(2s)}_{\mathrm{E1s}}$ closely resemble those of $\delta\omega^{(1)}_{\mathrm{E1a}}$ and $\delta\omega^{(1)}_{\mathrm{E1s}}$, throughout s, both when $kl = \pi/4$ and when $kl = 2\pi$. When s varies the E1s line shift is blue shifted from Ω_0 and the E1a mode is red shifted.

The line shifts $\delta\omega^{(2a)}_{\mathrm{M1E2a}}$ and $\delta\omega^{(2a)}_{\mathrm{M1E2s}}$ begin to deviate from $\delta\omega^{(1)}_{\mathrm{M1E2a}}$ and $\delta\omega^{(1)}_{\mathrm{M1E2s}}$ at $ks \simeq 3\pi_0/4$, when $kl = \pi/4$ and $kl = 2\pi$. However, $\delta\omega^{(2a)}_{\mathrm{M1E2a}}$ and $\delta\omega^{(2a)}_{\mathrm{M1E2s}}$ deviate much faster when $kl = 2\pi$. The M1E2a mode is blue shifted from Ω_0 and the M1E2s mode red shifted.

3.2.4 The response of an effective point emitter model to external fields

In this section, we compare the response of the four point electric dipole system with that of the effective two point emitter model under external driving, when we approximate the effective point emitter model with only one eigenmode. We consider the antisymmetric excitations, in which case the point emitter model exhibits the magnetic dipole and electric quadrupole moments. The driven dipoles radiate and induce excitations in the nearby dipoles, resulting in a strongly coupled system.

We solve the equation of motion, equation (2.26), in a steady-state ($\dot{\mathbf{b}} = 0$) for horizontal pairs of electric dipoles. We focus on the case when the external EM field drives one pair of dipoles only and propagates in the direction normal to the pair. For simplicity, we assume that the field perfectly couples to the antisymmetric excitation of the pair. In the point electric dipole system, we drive the pair 12, formed by the dipoles $n = 1, 2$. The driving by incident fields, $\mathbf{F}_{\text{in}}$ in equation (2.26), takes the form

$$\mathbf{F}_{\text{in}} = \frac{F_0}{\sqrt{2}} \begin{bmatrix} 1 \\ -1 \\ 0 \\ 0 \end{bmatrix} . \tag{3.88}$$

We only take the antisymmetric mode for the $N = 2$ effective point emitter system that exhibits magnetic dipole and electric quadrupole moments. The incident driving takes the form

$$\mathbf{F}_{\text{in}} = F_0 \begin{bmatrix} 1 \\ 0 \end{bmatrix} . \tag{3.89}$$

The coupling matrix $\mathcal{C}$ in equation (2.26) is non-Hermitian, but we can define an occupation measure for a particular eigenmode $\mathbf{v}_n$ in an excitation $\mathbf{b}$ by

$$O_n(\mathbf{b}) \equiv \left|\mathbf{v}_n^T \mathbf{b}\right|^2 . \tag{3.90}$$

For the four electric dipoles, we project the excitation onto the basis

$$\mathbf{v}_{12}^{(\pm)} = \frac{1}{\sqrt{2}} \begin{bmatrix} 1 \\ \pm 1 \\ 0 \\ 0 \end{bmatrix} , \quad \mathbf{v}_{34}^{(\pm)} = \frac{1}{\sqrt{2}} \begin{bmatrix} 0 \\ 0 \\ 1 \\ \pm 1 \end{bmatrix} . \tag{3.91}$$

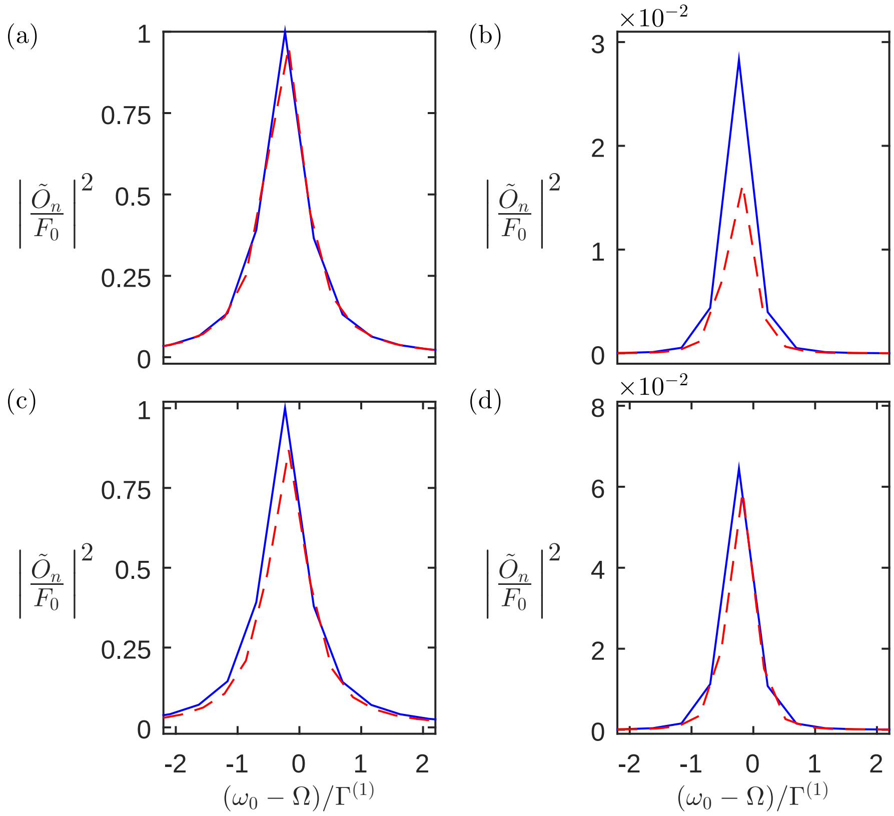

Figure 3.11: The excitation spectra of the antisymmetric modes of the electric dipole pairs (a,c) 1 and 2; (b,d) 3 and 4, as a function of the detuning of the incident frequency Ω from the resonance frequency ω_0 of a single point electric dipole. The resonance is at $-(\omega_0 - \Omega) \simeq 0.25\Gamma^{(1)}$. The full four point electric dipole model (blue solid line) and the corresponding effective two-point-emitter model, exhibiting magnetic dipole and electric quadrupole moments (red dashed line). In (a,b) $ks = 4\pi/3$ and $kl = \pi/3$, (c,d) $ks = 8\pi/11$ and $kl = 8\pi/7$.

Here, the superscript $(\pm)$ indicates symmetric/antisymmetric excitations of the dipole pair. In the effective two-emitter model we use the basis

$$\mathbf{v}_1^{(-)} = \begin{bmatrix} 1 \\ 0 \end{bmatrix}, \qquad \mathbf{v}_2^{(-)} = \begin{bmatrix} 0 \\ 1 \end{bmatrix}. \tag{3.92}$$

In Figure 3.11, we show the excitation spectra of the antisymmetric modes for the two models. For our choice of the driving in equation (3.88), the symmetric excitations of the electric dipoles are negligible. We find that, despite the inclusion of only one mode, the effective model agrees with the four-dipole case, provided that neither s nor l is too small. For small s the geometry of the configuration starts becoming important, while for small l, the contribution of the symmetric excitations would need to be included. For $ks = 4\pi/3$ and $kl = \pi/3$ (a,b), the effective model underestimates the excitation of the non-driven pair, while for $ks = 8\pi/9$ and $kl = 4\pi/9$ (c,d) the agreement is better.

3.3 Summary

In this chapter, we have extended and built upon the work of Chapter 2. Not just by including the electric quadrupole in the description of the normal mode oscillator $b(t)$, but also showing how simple systems comprising only point electric dipoles can be approximated by other higher order multipoles. In particular, we have shown how two antisymmetrically excited electric dipoles create an effective current loop, and can be modeled as a single resonator with both a magnetic dipole and electric quadrupole moment.

This effective current loop is important for our later work in Chapter 5, where we wish to create a system of effective current loops, and an effective toroidal dipole. Here, we have shown how simple point multipole systems interact. Each system has collective modes of oscillation, the number of which is determined by the number of interacting resonators. In our work analyzing two pairs of parallel electric dipoles, we have shown that the collective modes comprise symmetric and antisymmetric oscillating pairs. This is important because it shows exactly how diametrically opposite or perpendicular pairs can oscillate antisymmetrically, as they must if we wish to form effective current loops on an imaginary torus. The collective modes can be superradiant or subradiant. In certain configurations, some modes can exhibit one or the other, depending upon the choice in separation parameters. This is important to know, because it is often the subradiant modes that are the most interesting as they are difficult to excite. Understanding, the conditions under which superradiance and subradiance occurs is particularly beneficial to experimentalists in the design of their experiments.

Chapter 4

Interacting plasmonic nanorods

In Chapter 2, we described the general model for the EM interactions between plasmonic resonators, and reviewed the point dipole approximation. In Chapter 3, we produced original work introducing the point electric quadrupole approximation to our resonator, and its interactions with other point electric quadrupoles and electric and magnetic dipoles. When the resonators themselves are much smaller than the length of the incident light, and the separation between the resonators is large, a point multipole approximation is often sufficient to model the EM interactions. In metamaterial systems the separation between resonators, especially nearest neighbor resonators, is also much less than the incident light wavelength. The finite-size of the resonators can significantly affect the interactions. In this chapter, we introduce a model which accounts for the resonators' finite-size. We approximate individual resonators as cylinders (nanorods), with radius a and length H_j, see Figure 4.1. In Section 4.1, we introduce the formalism for interacting plasmonic nanorods. In Section 4.2, we analyze simple systems comprising the nanorods and compare the results to the equivalent point multipole approximation of Chapters 2 and 3. Some concluding remarks are included in Section 4.3.

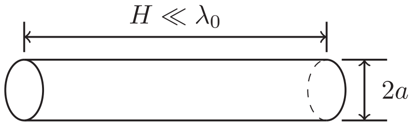

Figure 4.1: Geometry of a single nanorod with length H and radius a. The wavelength of the incident light is λ_0.

4.1 Finite-size resonator model

In the previous chapters, we approximated individual resonators as a series of point EM multipole sources. Specifically, we developed a general point multipole model up to, and including, the electric quadrupole interactions. In this section, we extend the formalism of Section 2.1, and determine the polarization and magnetization densities to solve the scattered EM fields taking into account the finite-size and geometry of the resonator.

For simplicity, the charge and current oscillations are assumed to be linear along the axis of the nanorod. For single, discrete, nanorods the magnetization is negligible $\mathbf{M}_j(\mathbf{r},t) \simeq 0$. The scattered EM fields of single nanorods, are thus determined by the corresponding polarization sources $\mathbf{P}_j(\mathbf{r},t)$ within the nanorod alone resulting in accumulation of charge on the ends of the nanorod. In the point dipole approximation reviewed in Section 2.2, a single nanorod may be approximated as a single point electric dipole only, the electric quadrupole moment of the cylinder is also zero.

The point electric quadrupole interactions introduced in Section 3.1 assumed two parallel antisymmetrically excited electric dipoles. When each nanorod is approximated as an electric dipole, a pair of antisymmetrically excited nanorods separated by a distance $l_j \ll \lambda_0$, see Figure 4.2, has similar characteristics as the electric quadrupole, see Figure 3.3. Whilst the magnetization of single nanorods is negligible, two parallel antisymmetrically excited nanorods possess an effective magnetization that gives rise to an effective magnetic dipole moment. The effective electric quadrupole and magnetic dipole interactions of closely spaced pairs of nanorods also cannot be readily decoupled and can be non trivial.

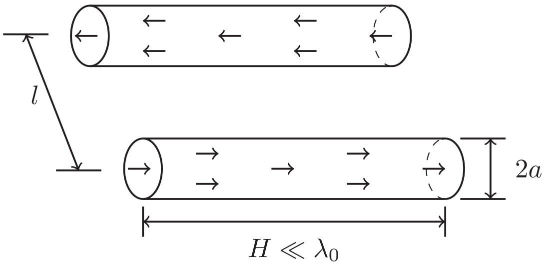

Figure 4.2: Schematic diagram of two antisymmetrically excited nanorods of radius a and length $H \ll \lambda_0$, separated by a distance l, which posses both magnetic dipole and electric quadrupole moments. The arrows indicate the orientation of the electric dipoles comprising each nanorod.

Analogous to the point multipole approximation, pairs of nanorods scatter EM fields that may drive the polarization sources within single nanorods, and vice versa. However, as in Section 3.2, we only consider the interactions between single nanorods and pairs of nanorods, separately.

4.1.1 Single discrete nanorod interactions

In the present section, the interactions between single nanorods are considered. Because the charge and current oscillations are assumed to be linear along the cylinder's axis, the magnetization of a single cylinder is negligible $\mathbf{M}_j(\mathbf{r}, t) \simeq 0$. The scattered EM fields, equations (2.3) and (2.4), are hence determined by the polarization density equation (2.10) within each nanorod alone. The polarization density of the jth nanorod is a uniform distribution of atomic point electric dipoles throughout the volume of the nanorod. For a single nanorod centered at the origin and aligned along the z axis, i.e., $\hat{\mathbf{d}}_j = \hat{\mathbf{z}}$, the spatial profile distribution of the polarization density is

$$\mathbf{p}_j(\mathbf{r}) = \frac{1}{\pi a^2}\hat{\mathbf{z}}\Theta(a-\rho)\Theta(H_j/2 - z)\Theta(H_j/2 + z)\,. \tag{4.1}$$

The scattered electric field $\mathbf{E}_{\mathrm{sc},j}(\mathbf{r})$ of a single nanorod due to polarization sources alone is given in equation (2.30), where the integral is taken over the volume of the cylinder centered at $\mathbf{r}_j$. Analytical solutions to equation (2.30) for finite-size cylinders exist in the far field, where they behave like those of point electric dipoles. The near and intermediate fields however, with spatial contributions which vary as $1/r^3$ and $1/r^2$, respectively, are much more complex. The full field solution to equation (2.30) must be integrated numerically, taking into account the finite thickness of the nanorods. The amplitude of the full EM fields from nanorods are proportional to the decay rate of a single nanorod Γ_{E1} [in Appendix F, we describe how we estimate the radiative and ohmic decay rates of isolated gold nanorods].

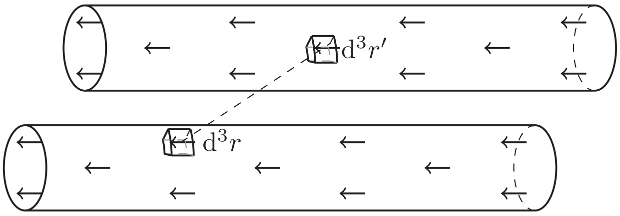

Figure 4.3: Schematic of the interaction between two nanorods which comprise a uniform distribution of electric dipoles (arrows) aligned along the axis of the cylinder.

The polarization sources within the jth nanorod are driven by the external emf $\mathcal{E}_{\mathrm{ext},j}$. The incident emf $\mathcal{E}_{\mathrm{in},j}$ follows from equation (2.18), with the incident EM field equation (2.14), integrated over the volume of the nanorod. The emf $\mathcal{E}^{\mathrm{sc}}_{i,j}$ resulting from the scattered EM fields from nanorod j driving the oscillations within nanorod i is given in equation (2.41). For single discrete interacting nanorods, the counterpart of equation (2.42) is $\mathcal{G}_{\mathrm{d}}$, with elements

$$\left[\mathcal{G}_{\mathrm{d}}\right]_{i,j} = \frac{3}{2}\int \mathrm{d}^3r\,\mathrm{d}^3r'\,\frac{\mathbf{p}_i(\mathbf{r})}{H_i}\cdot\mathbf{G}(\mathbf{r}-\mathbf{r}')\cdot\frac{\mathbf{p}_j(\mathbf{r}')}{H_j}\,. \tag{4.2}$$

The integral in equation (4.2) is taken over the volume of the nanorod located at $\mathbf{r}$ and the volume of the nanorod located at $\mathbf{r}'$, see, e.g., Figure 4.3.

4.1.2 Magnetic interactions between pairs of nanorods

In this section, we calculate the magnetic interactions between different pairs of parallel nanorods. We use the analogy introduced in Chapter 3.2.2, where two antisymmetrically excited electric dipoles possessed an effective magnetic dipole and electric quadrupole moment. We extend the formalism of Chapter 3.2.2.1 to account for the finite-size and geometry of the pair of nanorods and the associated magnetic interactions of antisymmetrically excited nanorods. The electric quadrupole interactions are discussed later.

We assume that the jth pair comprises two symmetric parallel nanorods with radii a and lengths H_j, separated by a distance l_j, see Figure 4.2. The jth pair of nanorods is located at $\mathbf{r}_j$. Each ± nanorod comprising the pair has its center located at $\mathbf{r}_{\pm,j} = [x_j, y_j \pm l/2, z_j]$. Additionally, we assume the individual nanorods are described by the model introduced in Section 4.1.1. When the jth nanorod pair are antisymmetrically excited, there is an effective current circulation about $\mathbf{r}_j$ resulting in an effective magnetic dipole moment and an effective electric quadrupole moment centered at $\mathbf{r}_j$. The spatial profile of the effective magnetization, accounting for the finite-size of the nanorods comprising the pair, is

$$\bar{\mathbf{w}}_j(\mathbf{r}) = \frac{1}{2}\int \mathrm{d}^3r\, \mathbf{r} \times \left[\mathbf{p}_{+,j}(\mathbf{r}) + \mathbf{p}_{-,j}(\mathbf{r})\right]. \tag{4.3}$$

The integral in equation (4.3) must be evaluated over the volume of each ± nanorod. The EM fields due to the effective magnetization are given by the second and first integrals in equations (2.30) and (2.31), respectively. The full field solutions must be integrated numerically, taking into account the geometry, finite-size and separation of both nanorods.

The effective magnetization within the pair of nanorods is driven by the external flux $\Phi_{\mathrm{ext},j}$. The incident flux $\Phi_{\mathrm{in},j}$ follows from equation (2.19), with the incident EM field equation (2.15), integrated over the volume of both nanorods. The flux $\Phi^{\mathrm{sc}}_{i,j}$ resulting from the EM interactions between different pairs of nanorods is given in equation (2.43). The finite-size counterpart of equation (2.44) is $\mathcal{G}_{\mathrm{w}}$, with components

$$\left[\mathcal{G}_{\mathrm{w}}\right]_{i,j} = \frac{3}{2}\int \mathrm{d}^3r\, \mathrm{d}^3r'\, \frac{\bar{\mathbf{w}}_i(\mathbf{r})}{A_{\mathrm{M},i}} \cdot \mathbf{G}(\mathbf{r}-\mathbf{r}') \cdot \frac{\bar{\mathbf{w}}_j(\mathbf{r}')}{A_{\mathrm{M},j}}. \tag{4.4}$$

The integral in equation (4.4) must integrated numerically over the pair of nanorods centered at $\mathbf{r}'$ and the pair at $\mathbf{r}$.

4.1.3 Electric interactions between pairs of nanorods

In addition to the EM fields scattered by the effective magnetization, the pair of rods also scatter EM fields from the polarization sources within the pair. The dipole fields of antisymmetrically excited nanorods is negligible. However, the antisymmetric excitation produces an electric quadrupole field which is not trivial.

Equations (3.7) and (3.8) give the EM scattered by an electric quadrupole. For a pair of finite-size nanorods, the integrals are evaluated numerically over the volume of both nanorods comprising the pair. The driving of the charge oscillations within the jth pair of nanorods is provided by the emf, equation (2.18). The incident emf is obtained from equation (3.37), integrated over the volume of both nanorods. The emf $\mathcal{E}^{\mathrm{sc}}_{i,j}$, a result of different pairs of nanorods interacting, is given in equation (3.40). The finite-size counterpart of equation (3.41) is the matrix $\mathcal{G}_{\mathrm{p}}$. The off-diagonal elements are given by

$$[\mathcal{G}_{\mathrm{p}}]_{i,j} = \sum_{\nu\alpha} \int \mathrm{d}^3 r\, \mathrm{d}^3 r' \, \frac{p^{\mathrm{q}}_{\nu,i}(\mathbf{r})}{A_{\mathrm{E},i}} G^{\nu\alpha}(\mathbf{r}-\mathbf{r}') \frac{p^{\mathrm{q}}_{\alpha,j}(\mathbf{r}')}{A_{\mathrm{E},j}} \,, \tag{4.5}$$

The integral in equation (4.5) must be integrated over the pair of rods centered at $\mathbf{r}'$ and the pair of rods centered at $\mathbf{r}$.

4.1.4 Magnetic-electric interactions between pairs of nanorods

In this section, we briefly describe the cross coupling between the magnetic moments of a pair of antisymmetrically excited parallel nanorods and their corresponding electric moments. The emf and flux resulting from point magnetic dipoles and point electric quadrupoles interacting are given in equations (3.47) and (3.48). The finite-size counterpart of the equation (3.45) appearing in the $\mathcal{E}^{\mathrm{sc}}_{i,j}$ and $\Phi^{\mathrm{sc}}_{i,j}$ is $\mathcal{G}_{\mathrm{X2}}$, with elements

$$[\mathcal{G}_{\mathrm{X2}}]_{i,j} = \frac{3}{2} \sum_{\nu\alpha} \int \mathrm{d}^3 r\, \mathrm{d}^3 r' \, \frac{p^{\mathrm{q}}_{\nu,i}(\mathbf{r})}{A_{\mathrm{E},i}} G^{\nu\alpha}_{\times}(\mathbf{r}-\mathbf{r}') \frac{\bar{w}_{\alpha,j}(\mathbf{r}')}{A_{\mathrm{M},j}} \,, \tag{4.6}$$

The integrals in equation (4.6) must be integrated over the pair of rods centered at $\mathbf{r}'$ and the pair of rods centered at $\mathbf{r}$.

4.2 Interacting nanorods

In Chapters 2.2 and 3.1, and Section 4.1, we have developed a formalism to model the interactions between different resonators. In our finite-size model, we approximated the resonators as nanorods. To accurately compare the different approaches and provide valuable insight for experimentalist, we must choose our resonance frequencies and radiative and ohmic decay rates with care.

In Appendix F, we calculate the resonance frequency ω_0 and relative decay rate $\Gamma_{\mathrm{O}}/\Gamma_{\mathrm{E1}}$ as a function of the nanorod length for a single finite-size gold nanorod. We use formulae for resonant light scattering from metal particles developed in Reference 84, where the nonradiative losses are incorporated in the analysis by the Drude model. We choose the parameters for the gold nanorods such that the length $H_0 = 1.5\lambda_p \simeq 209$ nm and radius $a = \lambda_p/5 \simeq 27.9$ nm, where λ_p denotes the plasma wavelength of gold (see Appendix F). This yeilds $H_0 \simeq 0.243\lambda_0$ and $a \simeq 0.0324\lambda_0$, where $\lambda_0 = 2\pi c/\omega_0 \simeq 859$ nm denotes the resonance wavelength of the nanorod. We use these as the dimensions of our nanorods throughout the remainder of this chapter (in the following chapter, we also use these properties). The corresponding decay rates are $\Gamma_{\mathrm{E1}} \simeq 0.83\Gamma^{(1)}$ and $\Gamma_{\mathrm{O}} \simeq 0.17\Gamma^{(1)}$, see Figure F.1 and Appendix F. Again, the (1) indicates the decay rate is that of a single nanorod. The choice of these parameters ensures that the decay rates are only weakly sensitive to small changes in the length of the nanorod.

In this section, we model the EM interactions of nanorods accounting for their finite-size and geometry. We utilize the model introduced in Section 4.1 for the interactions between discrete nanorods and pairs of nanorods. We compare the EM interactions of the finite-size nanorods (and pairs of nanorods), to the corresponding point multipole resonator interactions.

Before we analyze the EM interactions of finite size nanorods, we firstly calculate the magnetic dipole and electric quadrupole radiative emission rate of a pair of noninteracting antisymmetrically excited parallel nanorods. The electric dipole radiative emission rate of a single isolated gold nanorod was calculated in Appendix F.

For interacting nanorods, we initially introduce a single pair of parallel nanorods. We investigate how changes to the asymmetry of two nanorods affect the resonance shifts and widths, relative to two parallel point electric dipoles. We use the collective antisymmetric mode of oscillation to estimate the radiative emission rate of a pair of interacting antisymmetrically excited nanorods. We then compare this to our estimated radiative emission rate of the earlier introduced noninteracting pair, using the geometries introduced in Section 3.2, namely Figures 3.4(a) and 3.9(a).

The collective mode resonance frequency shifts and linewidths of the nanorod model [Section 4.1.1] are compared to those of the point electric dipole model. We then investigate how the relative line shift and linewidth deviations of two interacting pairs of nanorods [Sections 4.1.2–4.1.4] compare to the corresponding point multipole resonators.

4.2.1 Radiative emission of two parallel nanorods

In the present section, we determine the electric and magnetic radiative emission rates of a pair of antisymmetrically excited nanorods, taking into account their finite-size and geometry. The radiation emitted from each isolated gold nanorod comprising the pair is discussed in Appendix F. Each nanorod has the geometry introduced at the beginning of this chapter, namely radius $a = \lambda_p/5$ and height $H = 1.5\lambda_p$, and characteristic decay rate Γ_{E1}. Here, we compare the power radiated by spherical multipole moments to the power radiated by a general isolated resonator to obtain the magnetic dipole and electric quadrupole radiative emission rates of a pair of finite-size nanorods.

The total power P_{T} radiated by spherical multipoles is [39]

$$P_{\mathrm{T}} = \frac{2}{\epsilon_0 c k^2} \sum_{lm} \left[\left| \Lambda_{lm}^{(\mathrm{E})} \right|^2 + \left| \Lambda_{lm}^{(\mathrm{M})} \right|^2 \right] . \tag{4.7}$$

The moments $\Lambda_{lm}^{(\mathrm{E})}$ and $\Lambda_{lm}^{(\mathrm{M})}$ are the spherical electric and magnetic multipole moments, respectively. Explicit expressions for these read [39]

$$\Lambda_{lm}^{(\mathrm{E})} = -\frac{ik^2}{\sqrt{l(l+1)}} \int \mathrm{d}^3 r\, j_l(kr) Y_{lm}^{*} \times \left[ik\mathbf{r}\cdot\mathbf{J} + c(2+\mathbf{r}\cdot\nabla)\rho \right] , \tag{4.8}$$

$$\Lambda_{lm}^{(\mathrm{M})} = \frac{ik^2}{\sqrt{l(l+1)}} \int \mathrm{d}^3 r \left[\mathbf{r}\times\mathbf{J} \right]\cdot\nabla \left[j_l(kr) Y_{lm}^{*} \right] , \tag{4.9}$$

where $j_l(kr)$ are the spherical Bessel functions of order l, and $Y_{lm}(\theta,\phi)$ are the spherical harmonics with complex conjugate $Y_{l,-m}(\theta,\phi) = (-1)^{-m} Y_{lm}^{*}(\theta,\phi)$. The expression for the spherical multipole moments, equations (4.8) and (4.9), are exact expressions for arbitrary source sizes and geometries. In the long wavelength limit ($kr \ll 1$), the spherical Bessel function is expanded to leading order resulting in the familiar point multipole moments [39, 63], see Appendix C. The total radiated power is, again, the superposition of all multipole radiated powers. Conservation of energy ensures the total power is not affected by interference in the angular distribution of the power. For finite-size nanorods with charge and current densities given by equations (2.12) and (2.13), the spherical multipole moments must be integrated numerically over both nanorods.

Firstly, we use the electric dipole radiative emission rate Γ_{E1}, estimated in Appendix F, in order to determine the polarization density $\mathbf{P}_{\mathrm{E1}}(\mathbf{r},t)$ of an isolated nanorod that produces the electric dipole radiated power $P_{\mathrm{E1},j}$, where

$$P_{\mathrm{E1},j} = \omega_j \Gamma_{\mathrm{E1}} |b_j|^2 . \tag{4.10}$$

The polarization density, $\mathbf{P}_{\mathrm{E1}}(\mathbf{r},t)$, is related to ρ and $\mathbf{J}$ through equations (2.12) and (2.13), respectively. We define the polarization of the ± parallel nanorods, comprising the pair, to be $\pm\mathbf{P}_{\mathrm{E1}}(\mathbf{r},t)$, i.e., antisymmetrically excited.

We then obtain the magnetic dipole and electric quadrupole contributions, P_{M1} and P_{E2}, respectively, in the total radiated power equation (4.7). Comparing the corresponding power contributions of an isolated resonator, $P_{\mathrm{M1},j} = \omega_j \Gamma_{\mathrm{M1}} |b_j(t)|^2$ and equation (3.25), respectively, the decay rates Γ_{M1} and $\Gamma_{\mathrm{E2},}$ of a pair of parallel antisymmetrically excited nanorods are estimated.

In Figure 4.4, we show the relative magnetic dipole and electric quadrupole radiative emission rates as a function of the separation between the nanorods. The maximum

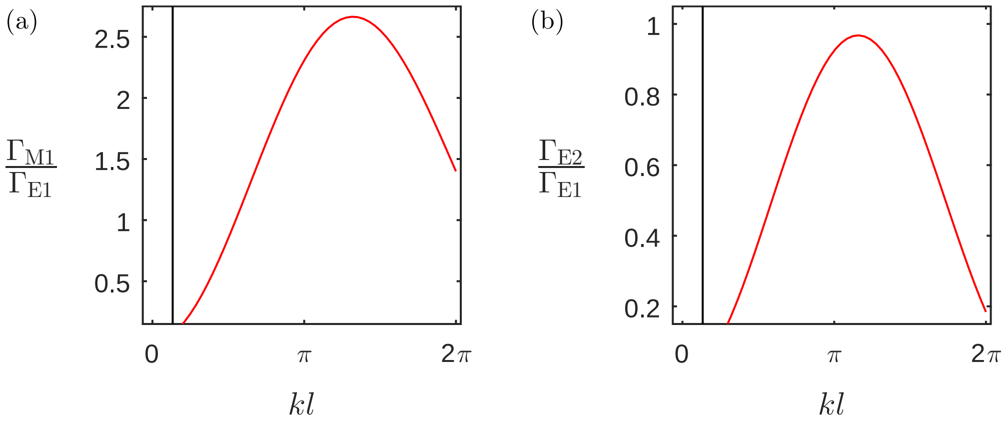

Figure 4.4: The relative radiative emission rates of two parallel oppositely orientated nanorods as a function of their separation parameter l. We show: (a) the magnetic dipole decay rate; and (b) the electric quadrupole decay rate. $\Gamma_{\mathrm{E1}} = (2\pi)85$ THz is the radiative emission rate of our single reference nanorod in isolation.

decay rates are $\Gamma_{\mathrm{M1}}/\Gamma_{\mathrm{E1}} \approx 2.7$ and $\Gamma_{\mathrm{E2}}/\Gamma_{\mathrm{E1}} \approx 0.97$, occurring at $kl \approx 4\pi/3$ and $kl \approx 6\pi/5$, respectively. These radiative emission rates notably differ from those estimated by the point multipole approach, where we find the corresponding decay rates to be $\Gamma_{\mathrm{M1}}/\Gamma_{\mathrm{E1}} \approx 4.4$ and $\Gamma_{\mathrm{E2}}/\Gamma_{\mathrm{E1}} \approx 3.5$.

4.2.2 Two nanorod systems

For the interactions between two nanorods, we choose their locations to be $\mathbf{r}_1 = -\mathbf{r}_2 = [0, l/2, 0]$. As in the case of two point electric dipoles, there are two eigenmodes of current oscillation: a symmetric mode, where both nanorods current oscillations are in phase (again denoted by a subscript 's'); and an antisymmetric mode (denoted by a subscript 'a'), where the current oscillations of the rods are out of phase. In Figure 4.5, we show the radiative resonance linewidths and line shifts for the collective eigenmodes of two parallel nanorods and two parallel point electric dipoles. As the separation becomes small $kl < \pi/2$, the line shift of the point electric dipole model begins to deviate from the line shift of the finite-size resonator model. Here, the line shift for the finite-size model is $\Omega_{\mathrm{a}}^{(1)} - \Omega_0 = -(\Omega_{\mathrm{s}}^{(1)} - \Omega_0) \approx 2.5\Gamma^{(1)}$. For $kl < \pi/2$, the line shift of the point electric dipole model antisymmetric mode is blue shifted from Ω_0, and the symmetric mode red shifted.

When $kl \approx 2\pi/3$, the decay rates of the point multipole approximation are: $\gamma_{\mathrm{a}}^{(1)} \approx 0.7\Gamma^{(1)}$ (subradiant); and $\gamma_{\mathrm{s}}^{(1)} \approx 1.3\Gamma^{(1)}$ (superradiant). The finite-size model shows decay rates: $\gamma_{\mathrm{a}}^{(1)} \approx 0.8\Gamma^{(1)}$; and $\gamma_{\mathrm{s}}^{(1)} \approx 1.2\Gamma^{(1)}$. As the separation becomes small $kl \approx \pi/6$, the antisymmetric linewidths approach the ohmic loss rate, $\gamma_{\mathrm{a}}^{(1)} \approx 0.2\Gamma^{(1)}$ and the symmetric mode linewidths become more superradiant $\gamma_{\mathrm{s}}^{(1)} \approx 1.8\Gamma^{(1)}$.

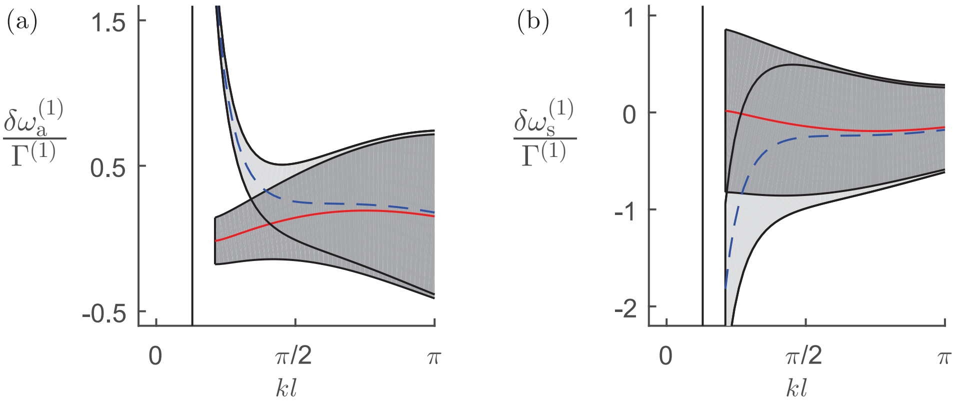

Figure 4.5: The radiative resonance linewidths and line shifts for the collective antisymmetric (a) and symmetric (b) eigenmodes, as a function of their separation parameter l, for two parallel rods. We show the line shift in the point electric dipole model (blue dashed line) and finite-size model (red solid line), the linewidth in the point electric dipole model (light shading about the blue dashed line), and the linewidth in the finite-size model (dark shading about the red solid line). The finite-size rods have lengths $H = 0.243\lambda_0$ and radii $a = 0.0324\lambda_0$. The radiative losses of each nanorod are $\Gamma_{\mathrm{E1}} = 0.83\Gamma^{(1)}$, the ohmic losses are $\Gamma_{\mathrm{O}} = 0.17\Gamma^{(1)}$.

4.2.2.1 Effects of different geometries

Here, we study how different nanorod orientations affect the validity of the point electric dipole approximation. We analyze how the orientations and displacements of the nanorods affect the collective mode resonance frequency shifts and decay rates. We consider the following systems: two parallel nanorods; two parallel but off-set nanorods [see Figure 4.6(a)]; and two nanorods tilted, such that their orientation vectors make an angle θ [see Figure 4.6(b)].

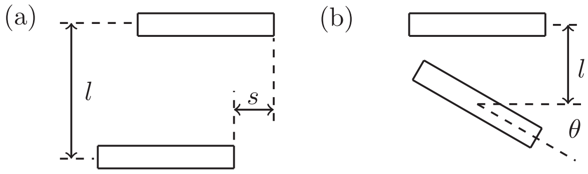

Figure 4.6: Schematic diagram of the different geometries for two interacting nanorods and two interacting point electric dipole resonators located at the center each nanorod.

In Figure 4.7, we show how the radiative linewidths and line shifts for the different two nanorod systems vary with the parameter l. The systems we consider are two parallel symmetric point electric dipoles, and the two nanorod systems shown in Figure 4.6.

At large separations, there is no significant effect on collective symmetric or antisymmetric mode linewidths. The linewidths $\gamma_{\mathrm{a,s}}^{(1)}$ of the systems with broken symmetry

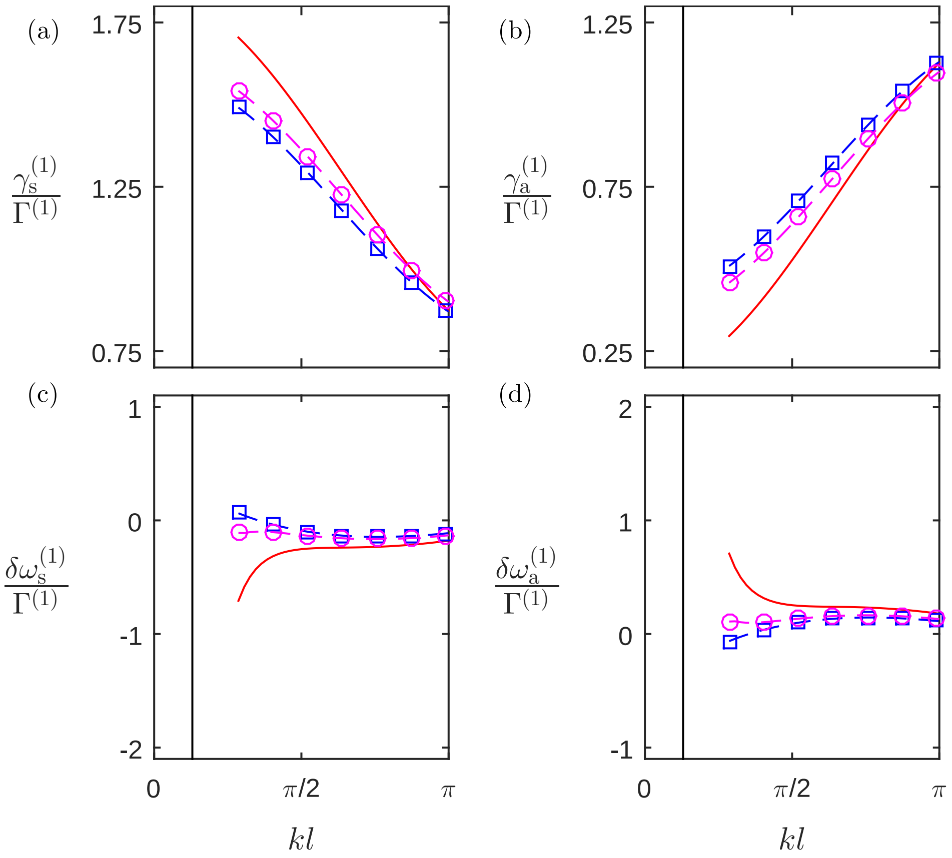

Figure 4.7: We show the radiative resonance linewidths and line shifts as a function of the parameter l for two interacting nanorods, when the symmetry between the nanorods is broken. We show: (a) the radiative linewidth $\gamma_s^{(1)}$ of the symmetric mode; (b) the linewidth $\gamma_a^{(1)}$ of the antisymmetric mode; (c) the line shift $\delta\omega_s^{(1)}$ of the symmetric mode; and (d) the line shift $\delta\omega_a^{(1)}$ of the antisymmetric mode. In (a–d) the lines represent the linewidths and line shifts of the: red solid line, two parallel point electric dipole; blue square dash, two parallel nanorods with off-set $ks = \pi/2$ [see Figure 4.6(a)]; and magenta circle dash, two parallel nanorods with orientation vectors making the angle $\theta = \pi/6$ [see Figure 4.6(b)].

[Figure 4.6] begin to deviate when $kl \simeq 3\pi/4$. Though the linewidths show deviations, when the rods are off-set by $ks = \pi/2$, the greatest deviation is at $kl \simeq \pi/4$ and is only approximately 11 % of the corresponding linewidth of two parallel point electric dipoles. When the nanorods are angled, $\theta = \pi/6$, the greatest deviation is again when $kl \simeq \pi/4$, and is only approximately 9 % of the corresponding linewidth of two parallel point electric dipoles.

The line shifts of the two nanorod systems do not begin to show significant deviations from the point electric dipole model until $kl \simeq \pi/2$. However, the line shift deviations here begin to deviate significantly. Interestingly, the two nanorod systems; off-set nanorods or angled nanorods, show the same collective mode line shifts when $kl \gtrsim \pi/4$. Only when $kl \lesssim \pi/4$ do the two line shifts begin to show deviations from each other.

Here, the angled nanorods begins to deviate following the trend of the corresponding point electric dipole line shift.

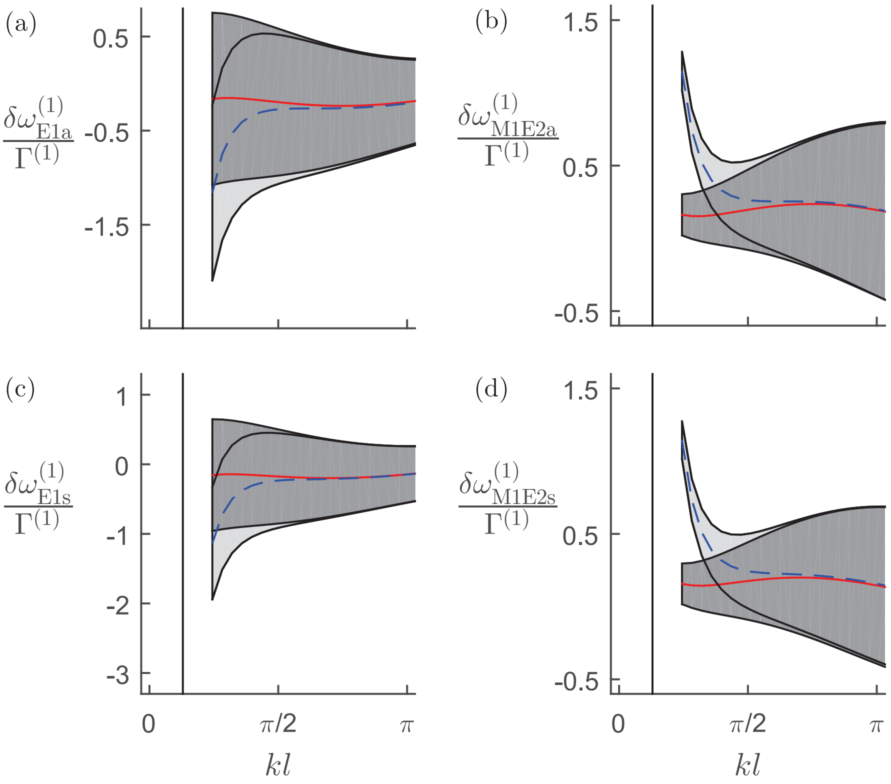

Figure 4.8: The radiative resonance linewidths and line shifts as a function of the metamolecule parameter l, with $ks = 2\pi$, for two pairs of horizontal nanorods and point electric dipoles, see Figure 3.4. For the nanorod parameters and plot descriptions see Figure 4.5 caption.

4.2.3 Four nanorod systems

In this section, we consider four nanorod systems comprising two parallel pairs of nanorods. We utilize the geometries introduced in Section 3.2, two horizontal pairs and two perpendicular pairs of nanorods, see Figures 3.4(a) and 3.9(a). When the rods are arranged as horizontal pairs [see Figure 3.4(a)], the Cartesian coordinates of the center of each nanorod are give in equation (3.77), and equation (3.82) when arranged as perpendicular pairs. We analyze the EM interactions employing the models developed in Section 4.1, for single nanorod interactions (also employed in Section 4.2.2), and interacting pairs of nanorods using the models introduced in Sections 4.1.2–4.1.4. The collective mode resonance frequency shifts and linewidths are compared to the corresponding shifts and widths of the point electric dipole approximation, in a similar manner to Section 4.2.2. We analyze the EM interactions using different approximations for the radiative emission rates Γ_{M1} and Γ_{E2}. In the point multipole approximation, analytical expressions were obtained for Γ_{M1} and Γ_{E2} and applied in Section 3.2. Here, we use the radiative emission rates of a pair of noninteracting nanorods calculated in Section 4.2.1, see Figure 4.4. We also use the radiative emission rate of a pair of anti-symmetrically excited nanorods $\gamma_{\mathrm{a}}^{(1)}$, and point electric dipole resonators estimated in Section 4.2.2, see Figure 4.5.

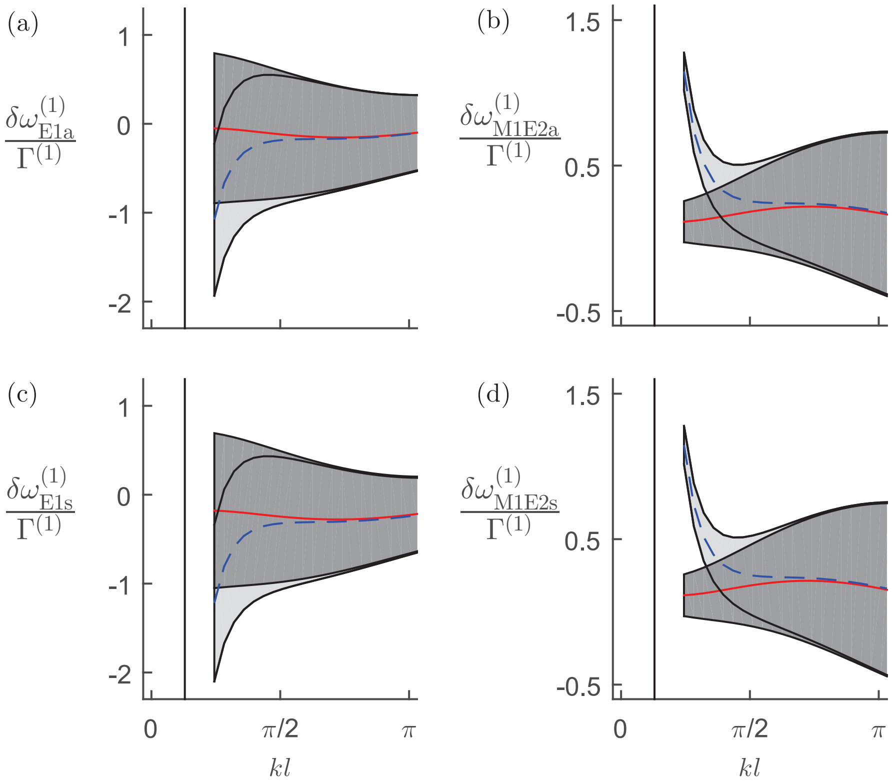

Figure 4.9: The radiative resonance linewidths and line shifts as a function of the metamolecule parameter l, with $ks = 2\pi$, for two perpendicular pairs of nanorods and point electric dipoles, see Figure 3.9. For the nanorod parameters and plot descriptions see Figure 4.5 caption.

In Figures 4.8 and 4.9, we show the resonance linewidths and line shifts of the point electric dipole approximation and those of four interacting nanorods [Section 4.1.1]. The geometry of the nanorods are horizontal and perpendicular pairs, respectively, see Figures 3.4 and 3.9, where the arrows are representative of the collective modes in the nanorod system also. Both horizontal and perpendicular nanorod systems exhibit similar behavior. The line shift of the point electric dipole approximation begins to deviate from the nanorod model when the separation between parallel pairs of rods is $kl \simeq \pi/2$. Here, the E1s mode is superradiant with $\gamma^{(1)}_{\mathrm{E1s}} \simeq 1.8\Gamma^{(1)}$, for both horizontal and perpendicular pairs. The E1a mode is also superradiant with $\gamma^{(1)}_{\mathrm{E1a}} \simeq 1.2\Gamma^{(1)}$ for horizontal pairs and $\gamma^{(1)}_{\mathrm{E1a}} \simeq 1.1\Gamma^{(1)}$ for perpendicular pairs.

Conversely, the M1E2a and M1E2s modes are subradiant with $\gamma^{(1)}_{\mathrm{M1E2a}} \simeq 0.4\Gamma^{(1)}$ and $\gamma^{(1)}_{\mathrm{M1E2s}} \simeq 0.7\Gamma^{(1)}$, for horizontal pairs and $\gamma^{(1)}_{\mathrm{M1E2a}} \simeq 0.5\Gamma^{(1)}$ and $\gamma^{(1)}_{\mathrm{M1E2s}} \simeq 0.6\Gamma^{(1)}$ for perpendicular pairs. Both superradiant and subradiant behavior is exhibited by the

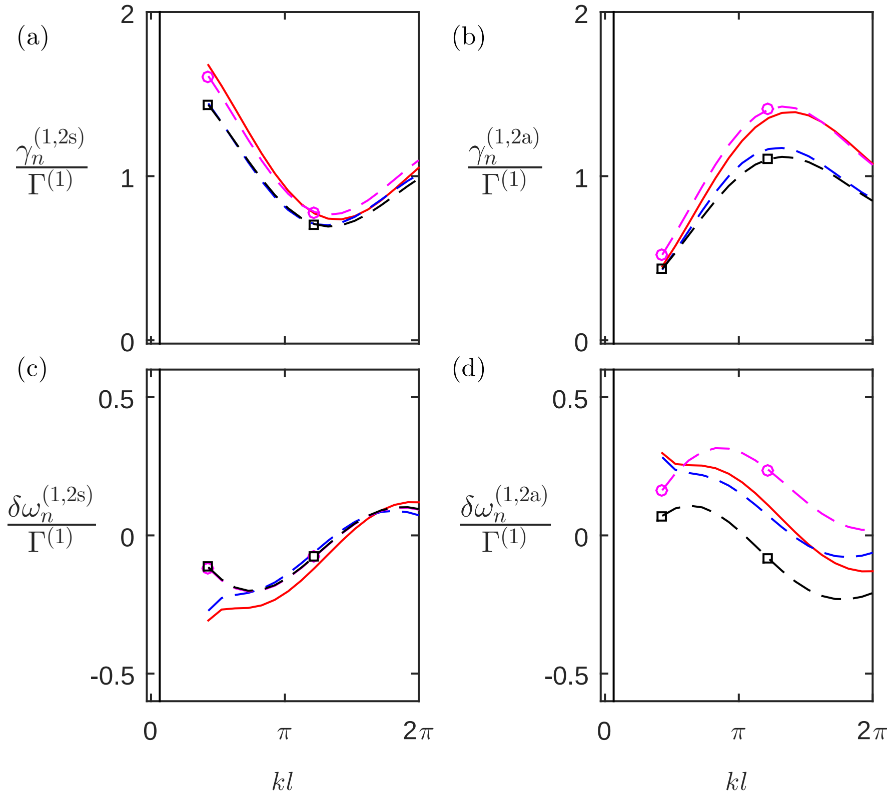

Figure 4.10: The radiative resonance linewidths $\gamma_n^{(1,2s,2a)}$ and line shifts $\delta\omega_n^{(1,2s,2a)}$ for the collective eigenmodes as a function of the separation parameter l, when $ks = 2\pi$, for two horizontal pairs of nanorods. We show: (a) the linewidth of the E1a and E1s collective excitation modes of the point electric dipole model and the symmetric (E1s) and antisymmetric (E1a) collective modes of symmetrically excited pairs of nanorods; (b) the linewidth of the M1E2a and M1E2s collective excitation modes of the point electric dipole model and the symmetric (M1E2s) and antisymmetric (M1E2a) collective modes of antisymmetrically excited pairs of nanorods; (c) the line shift of the E1a and E1s collective excitation modes of the point electric dipole model and the symmetric (E1s) and antisymmetric (E1a) collective modes of symmetrically excited pairs of nanorods; and (d) the line shift of the M1E2a and M1E2s collective excitation modes of the point electric dipole model and the symmetric (M1E2s) and antisymmetric (M1E2a) collective modes of antisymmetrically excited pairs of nanorods. The different lines represent: red solid line (a) and (c), the E1a mode; red solid line (b) and (d), the M1E2a mode; blue dash line (a) and (c), the E1s mode; blue dash line (b) and (d), the M1E2s mode; magenta dash circle (a) and (c), $\gamma_{\rm E1a}^{(2s)}$ and $\delta\omega_{\rm E1a}^{(2s)}$; magenta dash circle (b) and (d), $\gamma_{\rm M1E2s}^{(2a)}$ and $\delta\omega_{\rm M1E2s}^{(2a)}$; black dash square (a) and (c), $\gamma_{\rm E1a}^{(2s)}$ and $\delta\omega_{\rm E1a}^{(2s)}$; and black dash square (b) and (d), $\gamma_{\rm M1E2s}^{(2a)}$ and $\delta\omega_{\rm M1E2s}^{(2a)}$. The radiative losses of each electric dipole are $\Gamma_{\rm E1} = 0.83\Gamma^{(1)}$, the ohmic losses are $\Gamma_{\rm O} = 0.17\Gamma^{(1)}$.

E1a and M1E2s modes. At $kl \simeq 3\pi/2$, the E1a mode is subradiant, with $\gamma_{\rm E1a}^{(1)} \simeq 0.8\Gamma^{(1)}$ (horizontal pairs) and $\gamma_{\rm E1a}^{(1)} \simeq 0.6\Gamma^{(1)}$ (perpendicular pairs), whilst the M1E2s mode is superradiant with $\gamma_{\rm M1E2s}^{(1)} \simeq 1.5\Gamma^{(1)}$ (horizontal pairs) and $\gamma_{\rm M1E2s}^{(1)} \simeq 1.2\Gamma^{(1)}$

(perpendicular pairs).

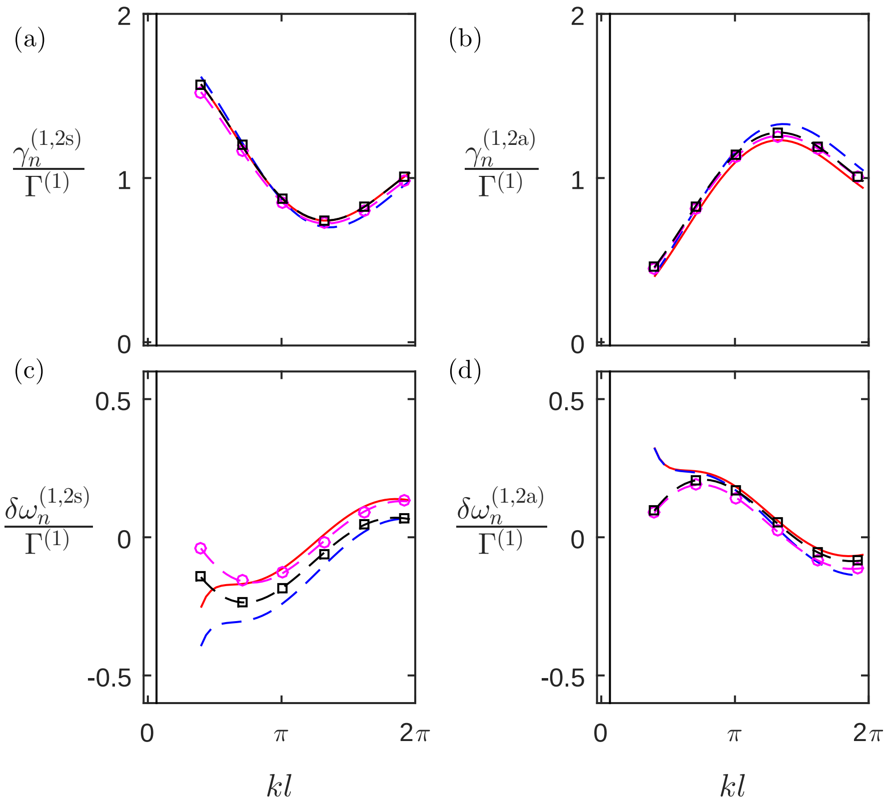

Figure 4.11: The radiative resonance linewidths $\gamma_n^{(1,2s,2a)}$ and line shifts $\delta\omega_n^{(1,2s,2a)}$ for the collective eigenmodes as a function of the separation parameter l, when $ks = 2\pi$, for two perpendicular pairs of nanorods. For plot descriptions, see Figure 4.11 caption.

In Figures 4.10 and 4.11, we show how the radiative linewidths and line shifts of the collective modes of oscillation of the $N = 2$ effective interacting pairs of nanorods vary with the parameter l, and compare the linewidths and line shifts to the corresponding modes of $N = 4$ interacting point electric dipoles. In Figure 4.10, we show the line widths and line shifts for horizontal pairs, see Figure 3.4. In Figure 4.11, we show the line widths and line shifts for perpendicular pairs, see Figure 3.9.

For both horizontal and perpendicular pairs, the line widths resulting from the $N = 4$ point electric dipole interactions qualitatively agree with those of the $N = 2$ interacting pairs of nanorods, even when l is small. The line shifts of the E1a and E1s modes of horizontal pairs of point electric dipoles show negligible differences from the corresponding line shifts $\delta\omega_{\mathrm{E1a}}^{(2s)}$ and $\delta\omega_{\mathrm{E1s}}^{(2s)}$, of symmetrically excited pairs of nanorods, for $kl \gtrsim \pi/4$ with $ks = 2\pi$. However, for $kl \lesssim \pi/2$, the point electric dipole model line shifts begin to blue shift from the nanorod model. The line shifts of the M1E2a and M1E2s modes show similar characteristics, however, at $kl \simeq \pi/2$, $\delta\omega_{\mathrm{M1E2a}}^{(1)}$ and $\delta\omega_{\mathrm{M1E2s}}^{(1)}$ red shift from corresponding line shifts of the antisymmetrically excited pair of nanorods model.

For antisymmetrically excited pairs of horizontal nanorods, for $kl \gtrsim \pi/4$, the line shift $\delta\omega^{(2a)}_{\mathrm{M1E2a}}$ underestimates $\delta\omega^{(1)}_{\mathrm{M1E2a}}$ by approximately $0.1\Gamma^{(1)}$. In a similar manner, the line shift $\delta\omega^{(2a)}_{\mathrm{M1E2s}}$ overestimates $\delta\omega^{(1)}_{\mathrm{M1E2s}}$ by approximately $0.1\Gamma^{(1)}$. Also, the line shifts of the point electric dipole model are approximately equal, i.e., $\delta\omega^{(1)}_{\mathrm{M1E2a}} \simeq \delta\omega^{(1)}_{\mathrm{M1E2s}}$, while $|\delta\omega^{(2a)}_{\mathrm{M1E2a}} - \delta\omega^{(2a)}_{\mathrm{M1E2s}}| \simeq 0.2\Gamma^{(1)}$. For perpendicular pairs of nanorods, the line shifts $\delta\omega^{(1)}_{\mathrm{E1a}}$ and $\delta\omega^{(2s)}_{\mathrm{E1a}}$ are approximately equal for $kl \gtrsim \pi/2$. The line shift $\delta\omega^{(2s)}_{\mathrm{E1s}}$ begins to red shift from $\delta\omega^{(1)}_{\mathrm{E1s}}$ at $kl \simeq 3\pi/2$.

4.3 Summary

In this chapter, we have shown how we can model plasmonic nanorods, accounting for their finite-size and geometry. In particular, we have determined how interacting discrete nanorods can be approximated as interacting point electric dipoles, particularly when their separation is greater than $kl = \pi/2$. Showing that we may approximate our nanorods as electric dipoles is of particular importance, because it allows us to utilize the results of Chapter 3 and create an effective current loop from two antisymmetrically excited nanorods also. This is a key result that we use, later in Chapter 5.

We used parallel pairs of nanorods as building blocks to construct other systems, namely: two horizontal pairs; and two perpendicular pairs, of parallel nanorods. By analyzing these systems, we have determined how they exhibit collective modes that correspond to effective electric dipoles interacting and effective magnetic dipoles and electric quadrupoles interacting. These systems are also greatly important for our work in Chapter 5, as it is precisely a combination of these systems that we will use to construct a toroidal metamolecule.

We have also gone as far as to approximate each pair of nanorods as a single effective resonator, and determined the magnetic dipole and electric quadrupole radiative emission rates of this resonator. While the point multipole resonator model in Chapter 3 worked well in such cases, the finite-size model is not as effective. We find it is much better to proceed in Chapter 5 with single discretely interacting nanorods, i.e., electric dipole interactions.

Chapter 5

Toroidal dipole excitations from interacting plasmonic nanorods

5.1 Introduction

In Chapter 2, we reviewed the general model of closely spaced interacting resonators, and the point electric and magnetic dipole approximation of the scattered EM fields. Later, in Chapter 4, we introduced a novel method to account for the finite-size and geometry of a particular class of resonator, nanorods. In Chapter 4, we also compared the finite-size model of interacting nanorods to the equivalent point electric dipole approximation. We investigated a single pair of parallel nanorods, showing how they can form an effective current loop, and two pairs of horizontal and perpendicular pairs of nanorods. These system choices become clear when we combine them into a single toroidal metamolecule.

Thus far, the theoretical understanding of the toroidal dipole response in resonator systems has been limited and the conditions under which the toroidal moment may be excited on the microscopic level have not been well known. In this chapter, we show theoretically how a simple structure formed by interacting plasmonic nanorods can support a collective excitation eigenmode that corresponds to a radiating toroidal moment. The toroidal mode is subradiant which could be important for the applications of the toroidal moments in nonlinear optics [60, 61] and in surface plasmon sensors [62]. We analyze the light-induced interactions between the closely-spaced plasmonic nanorods using a finite-size rod model as well as a model where the metamolecule is represented by a simple arrangement of point electric dipole emitters. We find that the point dipole model provides an accurate description of the radiative properties, except at very short interrod separations.

The generally weak coupling of the toroidal dipoles to external radiation fields makes it difficult to excite the toroidal mode. The structural symmetry of the mode inhibits the coupling to EM field modes that do not possess a similar ‘vortex-like’ symmetry. We show how a simple linearly-polarized incident light beam, however, can drive the toroidal dipole excitation when the geometric symmetry of the metamolecule is broken. The method is related to the double-resonator configuration introduced in Reference 54 and we provide simple optimization protocols for maximizing the toroidal dipole mode excitation. The emergence of the toroidal dipole excitation is shown in the forward scattered light as a Fano resonance, indicating a destructive interference between the broad-resonance electric dipole and narrow-resonance toroidal dipole modes. Using linearly polarized beams for the excitation of the toroidal dipole mode can be especially beneficial in driving and controlling large metamaterial arrays of toroidal unit-cell resonators, since the coupling in this case is independent of the array or the beam symmetries.

We begin this chapter by presenting a formal mathematical derivation of the toroidal dipole. Later, in Section 5.3, we investigate a toroidal metamolecule comprising plasmonic nanorods. We use the general model introduced in Chapter 2 and the point electric dipole approximation and discrete interacting nanorod models introduced in Chapters 2.2 and 4.1.1, respectively, to carry out the analysis. In Section 5.3.2, we show how the toroidal dipole response may be driven by linearly polarized light. Some concluding remarks are included in Section 5.4.

5.2 Mathematical formulation of the toroidal dipole

In Appendix C, we show a complete spherical multipole expansion of the EM fields **E** and **B** in terms of the multipole moments $\Lambda_{lm}^{(\mathrm{E})}$ and $\Lambda_{lm}^{(\mathrm{M})}$. The magnetic multipole moment $\Lambda_{lm}^{(\mathrm{M})}$ is shown to arise solely due to the transverse currents $(\nabla\times\mathbf{J})$. The electric multipole moments $\Lambda_{lm}^{(\mathrm{E})}$, in their exact form, however, have contributions from radial $(\mathbf{r}\cdot\mathbf{J})$ and longitudinal $(\nabla\rho)$ currents. The exact expression for $\Lambda_{lm}^{(\mathrm{E})}$ for arbitrary source sizes and geometries is

$$\Lambda_{lm}^{(\mathrm{E})} = -\frac{ik^2}{\epsilon_0 c l(l+1)}\int \mathrm{d}^3r\, Y_{lm}^*(\theta,\phi)\left[ikj_l(kr)\mathbf{r}\cdot\mathbf{J}(\mathbf{r}) + c\rho(\mathbf{r})\frac{\partial}{\partial r}\Big[rj_l(kr)\Big]\right]. \tag{5.1}$$

Here, again, $j_l(kr)$ are spherical Bessel functions of order l, and $Y_{lm}(\theta,\phi)$ are spherical harmonics of order lm. When the size a of the source is small, the long wavelength approximation ($ka \ll 1$) is the approach taken by many texts [39, 40, 63]. In this approach, the radial contribution to $\Lambda_{lm}^{(\mathrm{E})}$ is neglected; as it is of the order $(ka)^2$ lesser than the longitudinal contribution, see Appendix C.

When we look beyond the longwave limit, we can no longer ignore the radial current contribution, and $\Lambda_{lm}^{(\mathrm{E})}$ becomes a much more complicated expression. This contribution has been the subject of various publications on the formalism of toroidal multipoles [43, 45, 46, 47]. Reference 43, in particular, provides a complete formalism for all (electric (charge), magnetic and toroidal) multipole moments. The completely parametrized charge and current densities in References 43 and 46, involve complicated expressions involving vector spherical harmonics and Clebsh Gordon coefficients which detract from the brief introduction to toroidal dipoles required in this thesis. Here, to introduce the formalism for the toroidal dipole, we follow the approach presented in the discussion of Reference 46. This approach can be extended to determine the higher order toroidal multipoles.

To see how the radial currents affect $\Lambda_{lm}^{(\mathrm{E})}$, we consider the current and charge contributions separately. We rewrite equation (5.1) in the form

$$\Lambda_{lm}^{(\mathrm{E})} = -\frac{ik^2}{\epsilon_0 c l(l+1)}\left[I_{lm}^{(1)} + I_{lm}^{(2)}\right], \tag{5.2}$$

where $I_{lm}^{(1)}$ and $I_{lm}^{(2)}$ are

$$I_{lm}^{(1)} = ik\int \mathrm{d}^3r\, Y_{lm}^*(\theta,\phi) j_l(kr)\big[\mathbf{r}\cdot\mathbf{J}(\mathbf{r})\big], \tag{5.3}$$

$$I_{lm}^{(2)} = c\int \mathrm{d}^3r\, Y_{lm}^*(\theta,\phi)\rho(\mathbf{r})\frac{\partial}{\partial r}\big[r j_l(kr)\big], \tag{5.4}$$

respectively. Equations (5.3) and (5.4), closely resemble the form factors for the charge and toroidal multipole moments, Q_{lm} and T_{lm}, respectively, in Reference 49. However, $I_{lm}^{(1)}$ alone, for $l = 1, m = 0, \pm 1$, does not provide the usually attributed toroidal dipole moment. To see the complete form of the toroidal dipole moment, we consider the $l = 1$ term, and take the full form of $j_1(kr)$,

$$j_1(kr) = \frac{\sin kr}{(kr)^2} - \frac{\cos kr}{kr}. \tag{5.5}$$

Expanding $j_1(kr)$ as a Taylor series, then

$$j_1(kr) = \frac{kr}{3} - \frac{(kr)^3}{30} + \ldots, \tag{5.6}$$

and

$$\frac{\partial}{\partial r}\big[r j_1(kr)\big] = \frac{2kr}{3} - \frac{4(kr)^3}{30} + \ldots. \tag{5.7}$$

Consider the $l = 1,\ m = 0$ component of equation (5.3). With the spherical harmonic $Y_{10}^*(\theta,\phi)$ [see equation (B.18b)], and equation (5.6), we have,

$$I_{10}^{(1)} = i\frac{k^2}{3}\sqrt{\frac{3}{4\pi}}\int \mathrm{d}^3r\, z\big[\mathbf{r}\cdot\mathbf{J}(\mathbf{r})\big] + O(k^4). \tag{5.8}$$

Similarly, substituting equation (5.7) into equation (5.4), we have

$$\begin{aligned} I_{10}^{(2)} &= ck\frac{2}{3}\sqrt{\frac{3}{4\pi}}\int \mathrm{d}^3r \left[1-\frac{2}{10}(kr)^2\right]\rho(\mathbf{r})z + O(k^5)\,, \\ &= c\frac{k}{2\pi}\sqrt{\frac{4\pi}{3}}p_z - ck^3\frac{4}{30}\sqrt{\frac{3}{4\pi}}\int \mathrm{d}^3r\,\rho(\mathbf{r})zr^2\,. \end{aligned} \tag{5.9}$$

In the first term of equation (5.9), we have recovered the Q_{10} component of the spherical electric dipole moment and its Cartesian component p_z, see equation (C.39). The second term, however, cannot be associated with the electric dipole moment [46]. Using the continuity equation ($\nabla\cdot\mathbf{J} = i\omega\rho$), and the fact that $\omega = kc$, we obtain

$$I_{10}^{(2)} = c\frac{k}{2\pi}\sqrt{\frac{4\pi}{3}}p_z + ik^2\frac{4}{30}\sqrt{\frac{3}{4\pi}}\int \mathrm{d}^3r\,\left[\nabla\cdot\mathbf{J}(\mathbf{r})\right]zr^2\,. \tag{5.10}$$

Integration by parts on the $\left[\nabla\cdot\mathbf{J}\right]zr^2$ term in equation (5.10) [using the vector identity equation (C.27)], we obtain

$$\begin{aligned} I_{10}^{(2)} &= c\frac{k}{2\pi}\sqrt{\frac{4\pi}{3}}p_z - ik^2\frac{4}{30}\sqrt{\frac{3}{4\pi}}\int \mathrm{d}^3r\,\mathbf{J}(\mathbf{r})\cdot\left[2zr + r^2\right], \\ &= c\frac{k}{2\pi}\sqrt{\frac{4\pi}{3}}p_z - ik^2\frac{4}{30}\sqrt{\frac{3}{4\pi}}\int \mathrm{d}^3r\left[2z\big[\mathbf{r}\cdot\mathbf{J}(\mathbf{r})\big] + J_z r^2\right]. \end{aligned} \tag{5.11}$$

Finally, we substitute equations (5.8) and (5.11) into equation (5.2), we have

$$\Lambda_{10}^{(\mathrm{E})} = -\frac{ik^2}{4\pi\epsilon_0 c}\sqrt{\frac{4\pi}{3}}\left[ckp_z + ik^2t_z\right], \tag{5.12}$$

where

$$t_z = \frac{1}{10}\int \mathrm{d}^3r\left[z\big[\mathbf{r}\cdot\mathbf{J}(\mathbf{r})\big] - 2J_z r^2\right], \tag{5.13}$$

is the Cartesian component z, of the toroidal dipole moment $\mathbf{t}$. The Cartesian form of $\mathbf{t}$, is more commonly defined as

$$\mathbf{t} = \frac{1}{10}\int \mathrm{d}^3r\left[\mathbf{r}\big(\mathbf{r}\cdot\mathbf{J}(\mathbf{r})\big) - 2\mathbf{J}r^2\right]. \tag{5.14}$$

Equation (5.12) can be written in the equivalent form

$$\Lambda_{10}^{(\mathrm{E})} = -i\frac{k^2}{4\pi\epsilon_0 c}\left[kcQ_{10} + ik^2T_{10}\right], \tag{5.15}$$

where Q_{10} is the $l = 1, m = 0$ component of the spherical electrostatic multipole moment [see equation (C.39)], and T_{10} is the equivalent component of the spherical multipole moment

$$T_{10} = \frac{1}{10}\sqrt{\frac{4\pi}{3}}\int \mathrm{d}^3r\left[z\big[\mathbf{r}\cdot\mathbf{J}(\mathbf{r})\big] - 2J_z r^2\right]. \tag{5.16}$$

The generalization to equation (5.15) is [46]

$$\Lambda^{(\mathrm{E})}_{lm} = -i\frac{k^2}{4\pi\epsilon_0 c}\left[kcQ_{lm} + ik^2 T_{lm}\right]. \tag{5.17}$$

Where, T_{lm} are the complete spherical toroidal multipole moments, see Reference 43. Systems which exhibit toroidal moments are solenoidal tori, defined by their major and minor radii, carrying poloidal currents (see e.g. Figure 1.3). If the system is not doubly wound there are no magnetic moments, additionally if the system is not charged, there are no electric moments. Within the torus, however, the magnetic field is not zero and there exists a toroidal dipole moment given by equation (5.14) which is perpendicular to the azimuthal plane.

5.3 Toroidal metamolecule

The remainder of this chapter presents original work on a toroidal metamolecule. In this section, the models developed in Chapter 2.2 for point electric dipole interactions, and Chapter 4.1.1 for finite-size nanorod interactions are employed to demonstrate how a toroidal metamolecule may exhibit a toroidal dipole response and how we may drive that response with linearly polarized light.

We introduce a toroidal metamolecule that generally comprises N nanorods distributed over two layers. Each layer has $N_\theta = N/2$ emitters orientated radially outwards from the central axis of the metamolecule and equally spaced in the azimuthal direction. The second layer of emitters, identical to the first, is positioned a distance $2y$ above the first layer. The orientation of both layers is such that there are N_θ pairs of parallel emitters. In general, the symmetry of the metamolecule is therefore $C_{\frac{N}{2}h}$, a combination of $N/2$ rotations about the $N/2$-fold symmetry axis $C_{\frac{N}{2}}$ and the reflection in a horizontal plane σ_h (a plane perpendicular to the principal axis of rotation).

In Cartesian coordinates the orientation vectors of the nanorods are $\hat{\mathbf{d}}_j = \hat{\mathbf{x}}\cos\theta_j + \hat{\mathbf{z}}\sin\theta_j$. The density of the metamolecule is determined by $\Delta\theta = \theta_{j+1} - \theta_j$. As $\Delta\theta \to 0$, the metamolecule approaches a torus. We showed in Chapter 3.2.1, that a pair of parallel antisymmetrically excited electric dipoles forms an effective current loop (magnetic dipole moment). Therefore, in principle, antisymmetrically excited parallel pairs of electric dipoles, orientated radially outwards about the axis of a torus, approximates the quasi-vortex configuration of magnetic dipoles, i.e., a toroidal dipole.

In the present section, for simplicity, the radiative properties of a toroidal metamolecule comprising $N = 8$ nanorods, where $\Delta\theta = \pi/2$, are analyzed. In Chapter 4, we analyzed in detail the interactions of discrete point electric dipole resonators and finite-size nanorods for different $N = 2$ and $N = 4$ resonator systems. Here, we perform a similar analysis of our $N = 8$ nanorod (and equivalent point electric dipole) toroidal metamolecule. Although an eigenmode of such a metamolecule only approximately describes a toroidal dipole, the characteristic properties of the resonator interactions and the toroidal dipole excitation by an incident field are already evident. As the density of the structure increases, the analysis can be easily extrapolated to account for the increased number of resonators as illustrated in the toroidal mode excitation shown in Figure 5.6(a–b).

We first study a symmetric toroidal metamolecule (where all the nanorods are of equal length) and then break the geometric symmetry of the metamolecule in order to excite the toroidal mode using a simple light beam. In the symmetric metamolecule, we identify the associated collective modes of current oscillation and compare the resonance linewidths and line shifts obtained both in the point dipole approximation and in the finite-size resonator models. Finally, we determine how the toroidal dipole response of a toroidal metamolecule with some inherent asymmetry may be driven by linearly polarized light.

5.3.1 Symmetric toroidal metamolecule

A schematic illustration showing the arrangement and labeling system for the nanorods is shown in Figure 5.1. In Cartesian coordinates the locations of the point dipole and

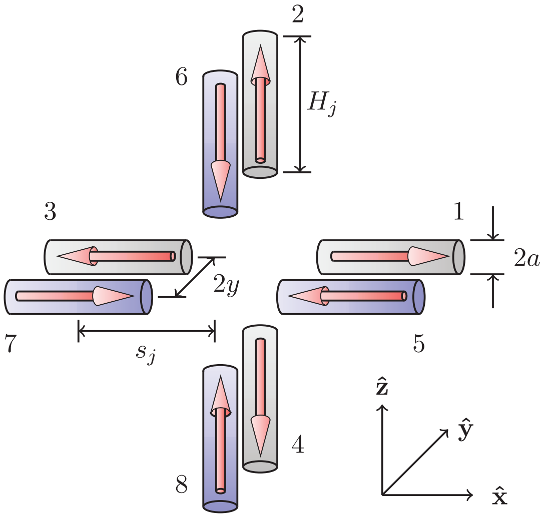

Figure 5.1: Toroidal dipole mode of an eight symmetric rod metamolecule. The shading of the nanorods indicates those nanorods in a shared plane, the arrows indicate the phase of current oscillation. The radial position of the center of an individual nanorod is s_j. The separation between parallel layers is $2y$.

the centers of the nanorods are,

$$\mathbf{r}_{1,5} \;=\; \begin{bmatrix} s_{1,5} \\ \pm y \\ 0 \end{bmatrix}, \quad \mathbf{r}_{2,6} = \begin{bmatrix} 0 \\ \pm y \\ s_{2,6} \end{bmatrix}, \quad \mathbf{r}_{3,7} = \begin{bmatrix} -s_{3,7} \\ \pm y \\ 0 \end{bmatrix}, \quad \mathbf{r}_{4,8} = \begin{bmatrix} 0 \\ \pm y \\ -s_{4,8} \end{bmatrix}. \tag{5.18}$$

In a symmetric system then $s_j = s$ (for all j). Because the nanorods are symmetric (as in Chapter 4), the radiative emission rate, ohmic loss rate and total decay rate of each nanorod are identical, i.e., $\Gamma_{\text{E1},j} = \Gamma_{\text{E1}}\,, \Gamma_{\text{O},j} = \Gamma_{\text{O}}$ and $\Gamma_j = \Gamma$. In this chapter (and the remainder of the thesis), we consider only the interaction between point electric dipoles and single discrete nanorods, hence, for clarity we omit the superscript (1) that was used for such systems in Chapter 3 and 4.

We continue to simplify the comparisons between the point dipole approximation and the finite-size model by assuming that their radiative as well as ohmic decay rates are equal. We use the resonance frequency ω_0 and relative decay rate $\Gamma_{\text{O}}/\Gamma_{\text{E1}}$ calculated in Appendix F for different rod lengths. We choose the nanorods of the symmetric metamolecule to have lengths $H_0 = \lambda_0/4$ and radii $a = \lambda_0/30$, and use these dimensions as those of a reference nanorod (we have analyzed $N = 2$ and $N = 4$ systems of these nanorods in Chapter 4). This corresponds to a radiative emission rate $\Gamma_{\text{E1}} = 0.83\Gamma$ and $\Gamma_{\text{O}} = 0.17\Gamma$, see Figure F.1 and Appendix F. The corresponding resonance wavelength of the nanorod is $\lambda_0 = 859$ nm. We also assume, initially, that the incident light is tuned to the resonance frequency of the nanorods, i.e., $\Omega_0 = \omega_0$, driving the charge oscillations within the nanorods.

In our metamolecule (Figure 5.1), there are $N = 8$ collective modes of oscillation. The different modes may have superradiant or subradiant characteristics. The classification of the different eigenmodes of the toroidal metamolecule comprising symmetric nanorods is shown in Figure 5.2. Here, we find it intuitive to describe the collective modes in terms of EM multipoles. In Table 5.1, we list the character table for the symmetry group C_{nh} (for $n = 4$) [85], where the eigenmodes are related to the corresponding Mulliken symbols [86], commonly used in group theory to denote degenerate and symmetric properties of the point group.

The two modes depicted in Figures 5.2(a) and 5.2(b) are doubly degenerate and symmetric with respect to σ_h. They correspond to vertical and horizontal electric dipole (E1) modes, respectively. In the E1 modes the responsive nanorods oscillate in phase and there is an effective electric dipole. Each of the E1 modes is a rotation of the other, consequently they experience the same resonance frequency shift and decay rate. In a similar manner to the E1 modes, Figures 5.2(c) and 5.2(d) are also doubly degenerate, but are antisymmetric with respect to σ_h. These modes depict vertical and horizontal magnetic dipole modes (M1), respectively. In Chapter 3, we showed that these modes also depict electric quadrupoles, in this chapter, for clarity, we designate these modes as

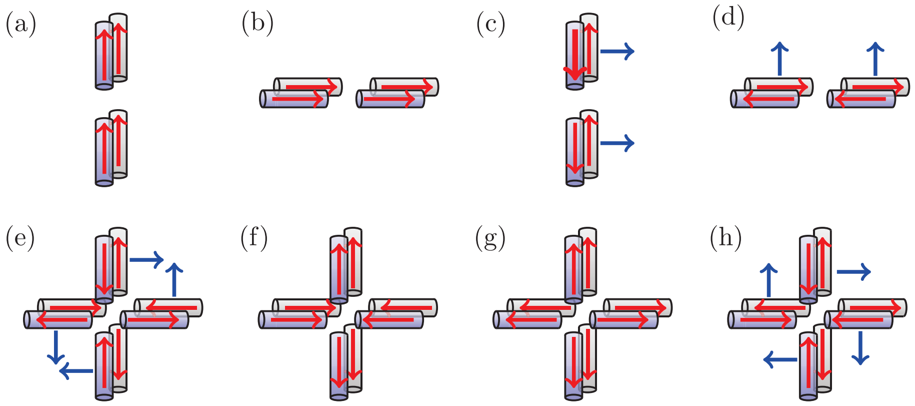

Figure 5.2: Representation of the eigenmodes of a symmetric eight-rod metamolecule. The red arrows represent the electric dipole moments and the blue arrows effective magnetic dipole moments. The modes are classified as: (a) vertical and (b) horizontal electric dipole (E1) modes; (c) vertical and (d) horizontal magnetic dipole (M1) modes; (e) a magnetic quadrupole (M2) mode; (f) an electric quadrupole (E2) mode; (g) a symmetric (sy) mode; and (h) the toroidal dipole (t) mode. For shading and axis properties, see Figure 5.1.

magnetic only. In the M1 modes, pairs of responsive nanorods oscillate out of phase, and the metamolecule forms an effective magnetic dipole. The M1 modes are also rotations of each other, thus experience the same resonance frequency shift and decay rate.

C_{4h}	E[a]	C_4	C_2	C_4^3	i[b]	S_4^3[c]	σ_h	S_4[c]
A (sy)	1	1	1	1	1	1	1	1
B (E2)	1	−1	1	−1	1	−1	1	−1
E (E1)	2	0	−2	0	2	0	−2	0
A′ (t)	1	1	1	1	−1	−1	−1	−1
B′ (M2)	1	−1	1	−1	−1	1	−1	1
E′ (M1)	2	0	−2	0	−2	0	2	0

[a]Identity; [b]Inversion; [c]Improper rotation $S_n = C_n\sigma_h$

Table 5.1: Character table of C_{nh}, for $n = 4$. The terms in parentheses are our physical multipole designation, see Figure 5.2, for the equivalent Mulliken symbols [86] .

The remaining modes are all independent. Figure 5.2(e) corresponds to a magnetic quadrupole (M2) mode. Each parallel pair of emitters oscillates out-of-phase, and four independent effective magnetic dipoles form. The M2 mode is antisymmetric with respect to rotation and σ_h. Figure 5.2(f) depicts an electric quadrupole (E2) mode. In this mode parallel pairs of emitters oscillate in phase with each other, but out of phase with their diametrically opposite parallel pair. Four independent effective dipoles combine to form an effective electric quadrupole. The E2 mode is antisymmetric with respect to rotation, but symmetric with respect to σ_h. Figure 5.2(g) is the symmetric mode, where all nanorods oscillate in phase. This mode is symmetric with respect to rotation and σ_h. The toroidal dipole mode, which is symmetric with respect to rotation, but antisymmetric with respect to σ_h, is shown in Figures 5.2(h) and 5.1. In this mode, parallel pairs of emitters oscillate out of phase in such a way that the effective magnetic dipoles form a circular loop. The orientations of the nanorods lead to the orientation vectors for their corresponding electric dipole moments: $\hat{\mathbf{d}}_{1,7} = \hat{\mathbf{x}}$; $\hat{\mathbf{d}}_{2,8} = \hat{\mathbf{z}}$; $\hat{\mathbf{d}}_{3,5} = -\hat{\mathbf{x}}$; and $\hat{\mathbf{d}}_{4,6} = -\hat{\mathbf{z}}$.

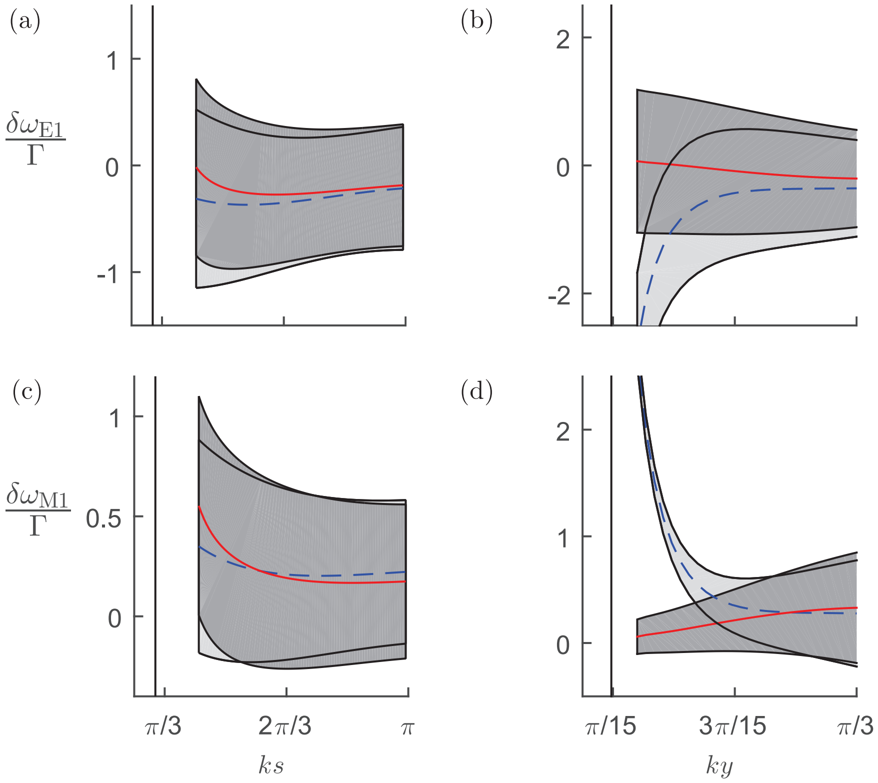

Figure 5.3: The radiative resonance linewidths and line shifts for the collective electric dipole (E1) and magnetic dipole (M1) excitation eigenmodes, as a function of the metamolecule parameters s and y. We show the line shift in the point dipole model (blue dashed line) and finite-size model (red solid line), the linewidth in the point dipole model (light shading about the blue dashed line), and the linewidth in the finite-size model (dark shading about the red solid line). In (a) the E1 mode, and in (c) the M1 mode, are shown as functions of the radial position s, with layer position $ky = \pi/3$. In (b) the E1 mode, and in (d) the M1 mode, are shown as functions of the layer position y, with radial position $ks = \pi/2$. The nanorods have lengths $H_0 = \lambda_0/4$ and radii $a = \lambda_0/30$. The radiative losses of each nanorod are $\Gamma_{\mathrm{E1}} = 0.83\Gamma$, the ohmic losses are $\Gamma_{\mathrm{O}} = 0.17\Gamma$.

We calculate the collective eigenmodes of the dynamic system described by equation (2.26), using the point electric dipole approximation and the finite-size nanorod model discussed in Chapters 2.2 and 4.1.1, respectively. In Figures 5.3–5.5 the line shifts and the corresponding resonance linewidths are shown, for the collective modes, as functions of the metamolecule varying parameters s and y (in the former the layer spacing is fixed at $ky = 2\pi/3$ and in the latter the radial spacing is fixed at $ks = \pi/2$). These modes are depicted in Figures 5.2(a–g) respectively.

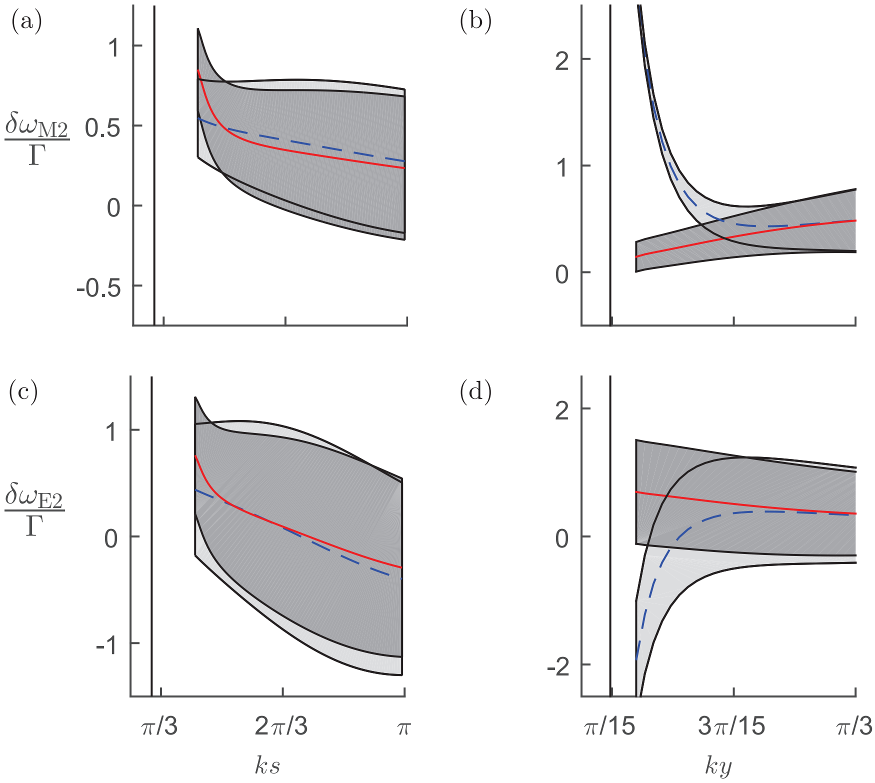

Figure 5.4: The radiative resonance linewidths and line shifts for the collective magnetic quadrupole (M2) and electric quadrupole (E2) excitation eigenmodes, as a function of the metamolecule parameters s and y. In (a) the M2 mode, and in (c) the E2 mode, are shown as functions of the radial position s. In (b) the M2, and in (d) the E2 mode, are shown as functions of the layer position y. For the rod parameters and plot descriptions see Figure 5.3 caption.

We find that the point electric dipole model qualitatively agrees with the finite-size model. The agreement becomes very good for larger rod separations. The toroidal dipole mode and the symmetric mode are subradiant for all parameter values we considered. This is also true for the magnetic quadrupole mode, M2, except for some specific values of the rod positions. The toroidal dipole mode is always the most subradiant mode, indicating a very weak coupling to external light fields. Magnetic dipole and electric quadrupole modes can generally exhibit both superradiant or subradiant characteristics depending on the precise details of the metamolecule's construction, while the electric dipole modes are almost always superradiant.

Specifically, for small radial separation $ks = \pi/3$ (and the layer separation is fixed at $ky = \pi/3$), the superradiant modes, E1 and M1 [Figures 5.3(b) and 5.4(a)], have decay rates $\gamma_{\mathrm{E1}} \approx 1.8\Gamma$ and $\gamma_{\mathrm{M1}} \approx 1.15\Gamma$. The toroidal dipole mode has $\gamma_{\mathrm{t}} \approx 0.3\Gamma$. When $ks \approx \pi/2$, the E2 mode also becomes superradiant ($\gamma_{\mathrm{E2}} \approx 1.25\Gamma$), whilst the decay rates of the E1 and M1 modes reduce to $\gamma_{\mathrm{E1}} \approx 1.5\Gamma$ and $\gamma_{\mathrm{M1}}^{\approx}\Gamma$, respectively. Even for the larger separation the toroidal dipole mode is still strongly subradiant ($\gamma_{\mathrm{t}} \approx 0.4\Gamma$ at $ks \approx \pi/2$ and $\gamma_{\mathrm{t}} \approx 0.6\Gamma$ at $ks \approx \pi$). For large radial positions, $ks \approx \pi$, only the E1 and E2 modes are superradiant ($\gamma_{\mathrm{E1}} \approx 1.2\Gamma$ and $\gamma_{\mathrm{E2}} \approx 1.65\Gamma$, respectively) and the M2 mode becomes subradiant ($\gamma_{\mathrm{M1}} \approx 0.75\Gamma$).

When we reduce the layer spacing to $ky < \pi/8$, with the radial separation fixed at $ks = \pi/2$, several of the modes become subradiant, except the E1 and E2 modes ($\gamma_{\mathrm{E1}} \approx 1.6\Gamma$ and $\gamma_{\mathrm{E2}} \approx 2.2\Gamma$ at $ky \approx \pi/8$). The toroidal dipole decay rate at $ky \approx \pi/8$ is reduced to $\gamma_{\mathrm{t}} \approx 0.25\Gamma$ from $\gamma_{\mathrm{t}} \approx 0.45\Gamma$ at $ky \approx \pi/3$.

Figures 5.3–5.5 also display the resonance line shifts of the modes, $\delta\omega_n = -(\Omega_n - \Omega_0)$. As the radial separation becomes large, these asymptotically approach a constant. This is due to the large separations resulting in the relatively close parallel pairs of nanorods interacting independently as dipoles. The M2 mode has the largest shift with $\delta\omega_{\mathrm{M2}} \approx 0.3\Gamma$. The line shift of the toroidal dipole and E1 modes are small $\delta\omega_{\mathrm{t}} \approx 0.1\Gamma$ and $\delta\omega_{\mathrm{E1}} \approx 0.05\Gamma$. As the separation becomes small, $ks < \pi/2$, the line shifts of the finite-size model begins to deviate from those calculated in the point dipole approximation. At this range the total length of the metamolecule is $0.75\lambda_0$ and finite lengths of the nanorods become increasingly important to their interactions.

When the layer spacing parameter y is varied there is a more pronounced deviation in line shifts for small y. The line shift of the point dipole model begins to deviate when $y \approx 2\lambda_0/15$. Here, the total width of the metamolecule is $\lambda_0/6$, and the nanorods' finite radii begin to affect their interactions. In the region shown for y in Figures 5.3–5.5, the line shifts of the different modes do not approach constant values.

5.3.2 Driving the toroidal dipole response

A natural method of driving the toroidal dipole response in a toroidal metamolecule is to use radially polarized light. In the paraxial approximation, an incident displacement field $\mathbf{D}_{\mathrm{in}}(\mathbf{r},t) = D_{\mathrm{in}}(\rho,y,t)(\cos\phi\ \hat{\mathbf{z}} + \sin\phi\ \hat{\mathbf{x}})$, can be estimated in terms of complex vectors $\hat{\mathbf{e}}_+$ and $\hat{\mathbf{e}}_-$, where $\hat{\mathbf{e}}_\pm = \mp(\hat{\mathbf{z}} \pm i\hat{\mathbf{x}})/\sqrt{2}$, by

$$\mathbf{D}_{\mathrm{in}}(\mathbf{r},t) = \frac{D_{\mathrm{in}}(\rho,y,t)}{\sqrt{2}}\left[e^{i\phi}\hat{\mathbf{e}}_- - e^{-i\phi}\hat{\mathbf{e}}_+\right]. \tag{5.19}$$

Equation (5.19) is a superposition of Laguerre-Gaussian beams with one unit of angular momentum which can couple directly to the toroidal dipole mode. Employing radially polarized light, the toroidal dipole response may be driven in a symmetric toroidal metamolecule. When linearly polarized light is shone on the symmetric toroidal metamolecule the toroidal dipole response is suppressed; the dominant responses driven are the E1 responses.

Here, we analyze in detail how a toroidal dipole mode can also be excited using linearly polarized light and provide a simple protocol how to optimize the toroidal dipole

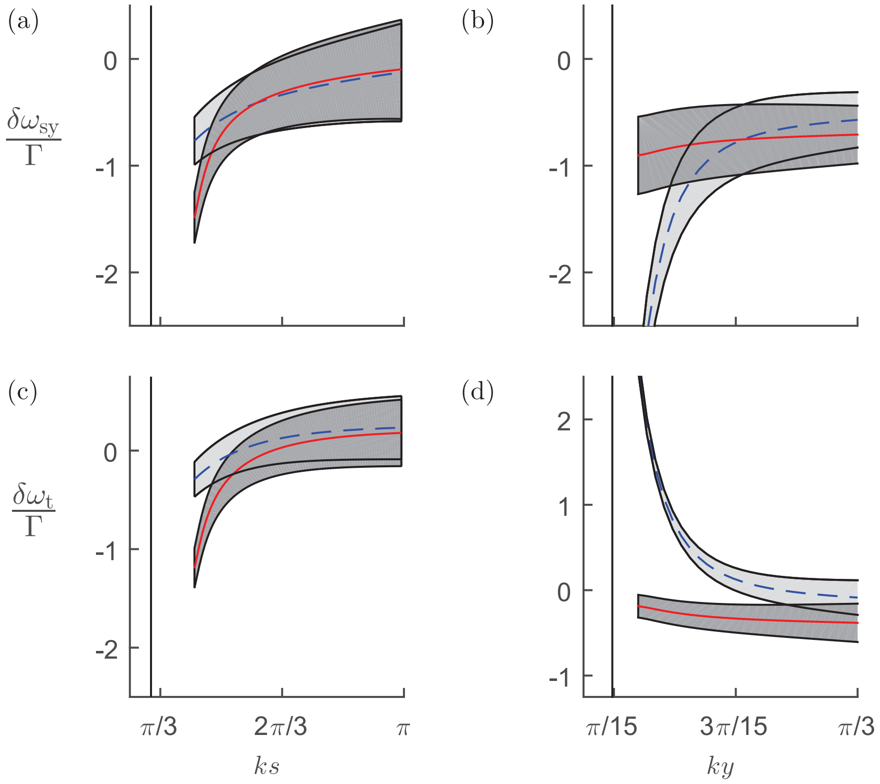

Figure 5.5: The radiative resonance linewidths and line shifts for the collective symmetric and toroidal dipole excitation eigenmodes, as a function of the metamolecule parameters s and y. In (a) the symmetric mode, and (c) the toroidal dipole mode are shown as a function of the radial position s. In (b) the symmetric mode and (d) the toroidal dipole mode are shown as a function of the layer position y. For the rod parameters and plot descriptions see Figure 5.3 caption.

excitation. Linear polarization has an advantage that it is readily available in an experiment and can easily be employed to drive toroidal dipole modes in large arrays of metamolecules, independently of the symmetry of the array or the beam.

Rather than spatially varying the light field to alter the excitation of individual nanorods (as done in the case of radial polarization), we alter the responses of individual nanorods to linearly polarized light by tailoring the length of the nanorods. Introducing the asymmetry in the rod lengths, according to Figure F.1(b), shifts the resonance frequencies and introduces a geometric asymmetry in the metamolecule. A similar principle was phenomenologically introduced in Reference 54, where asymmetric pairs of nanobars were experimentally employed to produce a toroidal dipole response.

To see how the nanorods should be altered, we consider an incident linearly polarized light wave tuned to the resonance frequency $\Omega_0 = \omega_0$ of our reference nanorod. The length of each rod j is then changed by δH_j, whilst the radius is fixed. For sufficiently small δH_j, the alteration shifts the nanorod's resonance frequency by $\delta\omega_j$ in proportion to δH_j, as we demonstrate using the Drude model in Appendix F, see Figure F.1. In this section, we will derive the pattern of rod length asymmetries required for linearly polarized light to excite a toroidal dipole response in the limit that the incident field is far detuned from resonance of any individual nanorod, i.e., $\delta\omega_j \gg \Gamma_j$. In this limit, interactions between nanorods can be neglected. We demonstrate how this scheme functions with smaller asymmetries in the presence of interactions in Appendix G.

We assume that the two layers are separated by a distance much less than a wavelength, hence the phase difference of the incident field between layers is negligible. In order to couple the field to all nanorods, we choose the polarization of the incident field to be such that it bisects the angle created by two adjacent nanorods in the same plane, as depicted in Figure 5.6. For a symmetric metamolecule, a field propagating into the plane of the metamolecule induces an emf [described by equation (2.18)] driving each nanorod j with an amplitude $F_{\mathrm{sym},j}$, where

$$F_{\mathrm{sym},j} = F_0 \cos\theta_j e^{iky_j} \,, \tag{5.20}$$

here F_0 is the driving amplitude of a rod oriented parallel to the incident field polarization, and y_j is the position coordinate of rod j along the incident field's propagation direction. The strength of interaction between the driving field and a nanorod varies with the angle θ_j between the nanorod and polarization of the incident light. Because the emf induced by the incident field along a rod is proportional to its length, the asymmetry in rod lengths perturbs the driving strength of each rod j in proportion to δH_j, so that the rod driving is

$$F_j = (F_0 + \delta F_j)\cos\theta_j \,, \tag{5.21}$$

where $\delta F_j \propto \delta H_j$ is the change in driving amplitude rod j would experience if it were parallel to the incident field.

Under these circumstances, when $\delta\omega_j \gg \Gamma_j$, interactions between resonators can also be ignored (i.e., $\delta\omega_j \gg \mathcal{C}_{ij}$ for $i \neq j$) in the dynamics of nanorod j, and

$$\dot{b}_j \approx i\delta\omega_j b_j + (F_0 + \delta F_j)\cos\theta_j \,. \tag{5.22}$$

Thus, to lowest order in δH_j, nanorod j has the steady-state response to the incident field

$$b_j \simeq i\frac{\cos\theta_j}{\delta\omega_j} F_0 \,. \tag{5.23}$$

Therefore, in the noninteracting limit, one could engineer the response of a metamolecule simply by adjusting the resonance frequencies of its individual nanorods.

In a toroidal dipole excitation, all resonators in the layer $+y$ oscillate radially outward (inward) in phase with each other, whilst those resonators in the layer $-y$ oscillate radially inward (outward) in phase. Such an excitation corresponds to the toroidal dipole eigenmode of the completely symmetric metamolecule and a quasi-vortex of magnetic dipoles. This is indicated by the arrows in Figure 5.1. To obtain this excitation profile, equation (5.23) suggests that the rod lengths should be modified such that

$$\delta H_j = \begin{cases} \delta H_0 \cos\theta_j & \text{for } j = 1, \dots, \dfrac{N}{2} \\ -\delta H_0 \cos\theta_j & \text{for } j = \dfrac{N}{2} + 1, \dots, N \end{cases} , \tag{5.24}$$

where δH_0 is a reference change in rod length, and we have assumed that δH_0 is sufficiently small that $\delta\omega_j \propto \delta H_j$. Although this profile of rod lengths was arrived at in a regime where interactions are neglected, we show that a similar distribution of lengths can also be effective in producing a toroidal dipole from a linearly polarized light wave driving in Appendix G. We illustrate the dependence of a nanorod's length, and hence resonance frequency, on its position within the metamolecule for the cases of $N = 16$ and $N = 8$ nanorods in Figure 5.6.

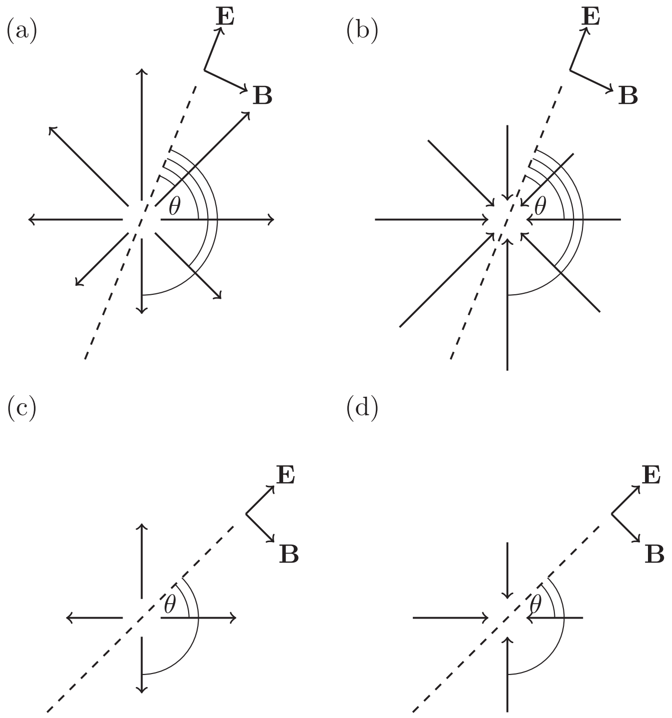

Figure 5.6: The excitation of the toroidal dipole mode by linearly polarized light. The length of the arrows indicate the rod lengths which, together with the angle θ each rod makes with the polarization of the incident light, ensures each rod is equally excited. The arrow direction indicates the state of the current oscillation within each nanorod. In (a) the top layer and (b) the bottom layer of the more general $N = 16$ case is shown. In (c) the top layer and (d) the bottom layer of the $N = 8$ case is shown. The $N = 8$ case is considered in the numerical simulation.

For a toroidal metamolecule which comprises eight nanorods, only two distinct lengths (resonance frequencies) are required in order to produce a toroidal dipole excitation from linearly polarized light. This equates to a difference in nanorod length $\mp\delta H$ about a mean rod length H_0. We define $H_{l,s} = H_0 \pm \delta H$ with $H_{1,2,7,8} = H_l$ and $H_{3,4,5,6} = H_s$, such that each parallel pair of nanorods comprises a long and short rod, see Figures 5.6(c) and 5.6(d), whose center's are located at $s_j = s$. The polarization vector of the incident field, equation (2.14), that will excite the toroidal dipole mode is $\hat{\mathbf{e}}_{\text{in}} = (\hat{\mathbf{x}} + \hat{\mathbf{z}})/\sqrt{2}$. The eigenmodes and line shifts and widths for a symmetric toroidal metamolecule comprising nanorods with length H_0 were discussed in Section 5.3.1. When the radial position of the reference rod is fixed, e.g., $s_l = \lambda_0/3$, and some asymmetry in rod length is introduced, the response of the metamolecule becomes a function of the relative rod lengths H_s/H_l.

The asymmetry discussed in this section is designed to promote the toroidal dipole response. Choosing different asymmetries, one may, in principle, excite any of the modes associated with the symmetric toroidal metamolecule [see Figure 5.2]. For example, we excite the M1 mode with an incident plane wave, also with polarization vector $\mathbf{e}_{\text{in}} = (\hat{\mathbf{x}} + \hat{\mathbf{z}})/\sqrt{2}$, by choosing $H_s = H_{1,2,3,4}$ and $H_l = H_{5,6,7,8}$.

5.3.3 Excitations of the toroidal dipole mode

The eigenmodes in Figure 5.2 are those of a symmetric toroidal metamolecule. When analyzing the amplitudes of the eigenmodes, of an asymmetric metamolecule, we do so using the symmetric metamolecule basis. The coupling matrix $\mathcal{C}$ is decomposed as

$$\mathcal{C} = \mathcal{C}_{\text{sym}} + \mathcal{A}\,, \tag{5.25}$$

where $\mathcal{C}_{\text{sym}}$ is the coupling between nanorods whose lengths are the mean rod length H_0. The matrix $\mathcal{A}$ contains the detail on asymmetry. The variation of the resonance frequencies between the nanorods generally suppresses the light-mediated interactions in the metamolecule [87]. For the point dipole model, we define this as a diagonal matrix whose elements are the resonance frequency shifts of the different nanorods, see Appendix G. In the finite-size nanorod model, in addition to the resonance frequency shifts in the diagonals, the off-diagonal elements give the difference in the finite-size nanorod interactions of a symmetric system and an asymmetric system, see Appendix G.

The amplitude of the different modes may be analyzed by expanding the vector of dynamic variables $\mathbf{b}(t)$ as

$$\mathbf{b}(t) = \sum_n c_n(t)\mathbf{v}_n\,, \tag{5.26}$$

where $c_n(t)$ is the amplitude of the eigenmode $\mathbf{v}_n$ of $\mathcal{C}_{\text{sym}}$. We denote the toroidal dipole amplitude as c_{t}. In the absence of any asymmetry, the only modes driven by linearly polarized light are the E1 modes. When the asymmetry depicted in Figure 5.6 is introduced to the metamolecule, the toroidal dipole mode (in addition to the E1 modes) is also driven.

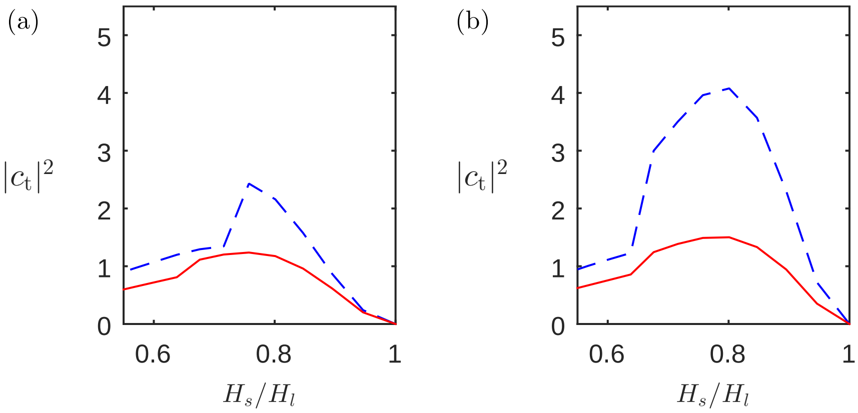

Figure 5.7: The intensity of the collective toroidal dipole excitation as a function of the ratio of rod lengths H_s/H_l. The centers of the longer nanorods are located at $ks_l = 2\pi/3$ and the layer position is $ky = \pi/5$. We show the point dipole model (blue dashed lines) and finite-size model (red solid lines). The nanorod mean length and radius are those of the reference nanorod. The radiative emission rate in (a) is $\Gamma_{\mathrm{E1}} = 0.83\Gamma$. In (b) there are no ohmic losses.

In Figure 5.7 we show the maximum intensity of the toroidal dipole mode as a function of the asymmetry between the cylindrical nanorods, for the point electric dipole approximation and for the finite-size model, when the metamolecule is driven at the resonance of the toroidal mode of the symmetric metamolecule. If there are no ohmic losses the finite-size model shows a maximum intensity when $H_s/H_l \approx 0.8$, and the intensity here of the point dipole model is approximately four times that of the finite-size model. As the asymmetry between the nanorods increases, the intensity of both the finite-size model and the point dipole approximation decreases.

When ohmic losses are accounted for, the maximum intensity is when $H_s/H_l \approx 0.75$ before decreasing. The incorporation of losses significantly affects the point electric dipole approximation, the maximum intensity is approximately 50 % less than when no losses were present. Conversely, the effect on the finite-size model is negligible.

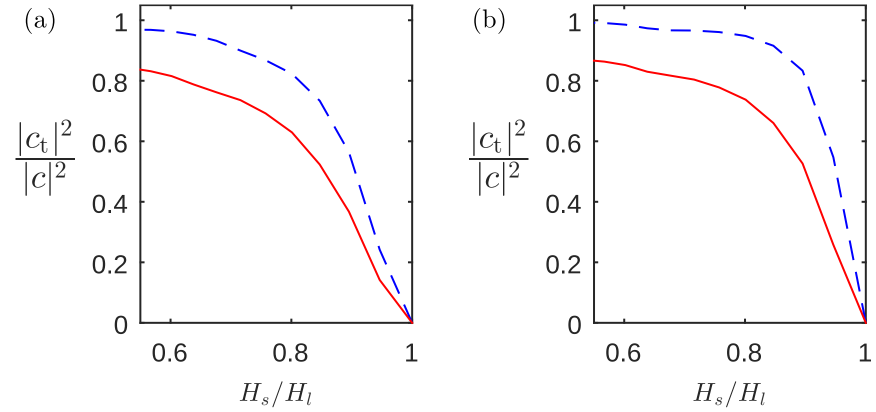

Figure 5.8: The relative amplitude of the collective toroidal dipole excitation as a function of the ratio of rod lengths when driven on the toroidal dipole resonance. The parameters as in Figure 5.7.

In Figure 5.8, the relative occupation of the toroidal dipole mode is shown as a function of the ratio of nanorod lengths. Although we consider a non-unitary, open system, the eigenmodes have periodic boundary conditions and in the studied cases form a well-behaving orthonormal pseudo-basis. We define the overlap between an eigenmode $\mathbf{v}_n$ with an excitation $\mathbf{b}$ by

$$O_n(\mathbf{b}) \equiv \frac{|\mathbf{v}_n^T \mathbf{b}|^2}{\sum_n |\mathbf{v}_n^T \mathbf{b}|^2} \,, \tag{5.27}$$

where the summation runs over all the eigenmodes. In both cases, when losses are present and when they are neglected, the relative occupation of the point electric dipole approximation over-estimates the finite-size model. In the absence of ohmic losses, the relative occupation of the point dipole model saturates at $H_s/H_l \approx 0.8$, where the total excitation of the metamolecule is in the toroidal dipole mode. In the finite-size model when $\Gamma_{\mathrm{O}} = 0$, saturation occurs when $H_s/H_l \approx 0.7$ and the relative occupation is approximately 0.8. When losses are present, the relative occupation at the maximum intensity of the toroidal dipole excitation ($H_s/H_l \approx 0.75$) is 0.95 for the point electric dipole approximation. The finite-size model here shows a relative occupation of 0.75.

In the absence of asymmetry between the nanorods $H_s/H_l = 1$, both the intensity plots in Figure 5.7, and the relative occupation plots Figure 5.8, show that there is no toroidal dipole excitation. However, even a small asymmetry in rod lengths produces a toroidal dipole excitation. Although the intensity of the toroidal mode excitation can be maximized at a relatively small value of the nanorod asymmetry, the fidelity of the toroidal dipole mode keeps increasing when the asymmetry is increased.

5.3.4 Scattered light intensity in the far field

It is also interesting to study the scattered light from a toroidal metamolecule in the far-field response. We again assume that the incident field propagating normal to the plane of the metamolecule excites the current oscillations in the nanorods. We calculate the collective excitations of the metamolecule by including all the radiative interactions between the nanorods. In Figure 5.9 we show the intensity of the scattered light in the forward direction (without the incident field contribution) from: a symmetric toroidal metamolecule; a toroidal metamolecule with the asymmetry designed to promote the toroidal dipole response; and a toroidal metamolecule designed to promote the M1 response. Two cases are displayed corresponding to two layer separations y.

In the symmetric case only the E1 collective modes are excited, displaying broad resonances. For large y, the E1 resonance is close to the resonance frequency, ω_0 of our reference nanorod, for small y the resonance is blue-shifted.

In the asymmetric case $H_{1,2,7,8} = H_l$ and $H_{3,4,5,6} = H_s$ (asymmetry promoting the toroidal dipole response), the light excites the E1 modes and the toroidal dipole mode.

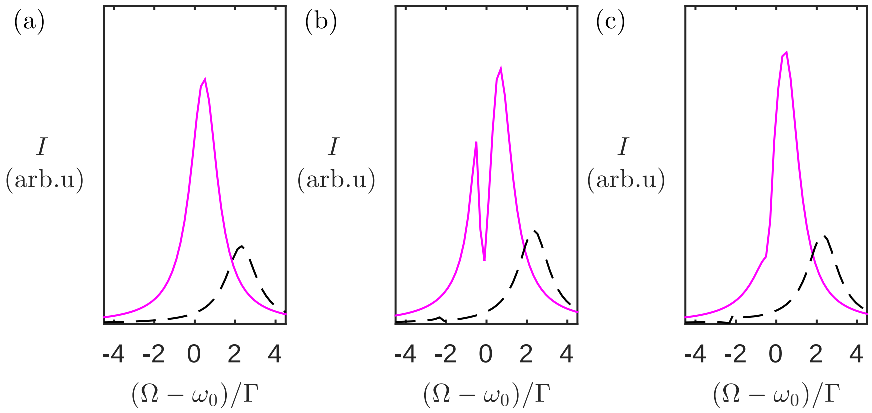

Figure 5.9: The scattered light intensity in the forward direction I, as a function of the detuning of the incident light from the resonance frequency ω_0 of our reference nanorod. We show the responses of: a symmetric toroidal metamolecule (a); a toroidal metamolecule with asymmetry promoting a toroidal response (b); and a toroidal metamolecule with asymmetry promoting the M1 response (c). The radial position of the nanorods $ks = 2\pi/3$, the layer position $ky = \pi/10$ (black dashed lines) and $ky = \pi/5$ (magenta solid line), $H_s/H_l = 0.75$, and $\Gamma_{\mathrm{E}} = 0.83\Gamma$. The intensity dip in (b) indicates a Fano resonance due to the interference between the E1 and toroidal dipole modes. The calculations are performed in the point dipole approximation.

A destructive interference between the broad-resonance E1 and the narrow-resonance toroidal modes produces a Fano resonance [88]. For the case of a large layer separation y, the Fano resonance clearly shows up as a dip in the spectrum of the scattered light intensity at the resonance of the toroidal dipole mode, indicating suppressed forward scattering. This is because a toroidal dipole excitation on a plane normal to the propagation direction does not contribute to the far-field radiation.

In the asymmetric case $H_{1,2,3,4} = H_l$ and $H_{5,6,7,8} = H_s$ (asymmetry promoting the M1 response), the light excites the E1 modes and the M1 mode. There is again a destructive interference between the E1 and M1 modes. Though in this case, the Fano resonance is much weaker.

The interference of the Fano resonance has an analogy in atomic physics in the interference of bright and dark modes in the electromagnetically-induced transparency [89]. Here, the subradiant toroidal mode (t) (and the M1 mode) acts as a dark radiative mode and the superradiant electric dipole mode (E1) as a bright mode. In the excitation of the E1 mode the different scattering paths, →E1, →E1→t→E1, etc., destructively interfere at the Fano resonance peak. The Fano resonances may also appear in other complex metamolecules, such as in oligomers [90], or as a result of a collective behavior of the metamaterial array [81]. The existence of more than one subradiant mode in a toroidal metamolecule and the possibility to employ collective effects in ensembles of toroidal metamolecules is particularly promising for tunable control of the resonances [81] and for sensing applications.

Our simple model of the radiative intensity provides a qualitative description of the Fano resonance of the toroidal dipole mode in the forward-scattered far-field spectrum. For 2D metamaterial arrays of asymmetric split-ring metamolecules, the point dipole radiation model provides a good qualitative agreement with the experimental findings due to weak higher-order multipole radiation of individual split-ring arcs [80]. In the studied cases of the resonances of individual nanorods, higher-order multipole radiation is similarly weak. Comparisons between multipole expansions and complete field calculations were performed in Reference 57 between the far-field radiation patterns of toroidal dipole resonances in a noninteracting resonator system.

5.4 Summary

This chapter is the culmination of the thesis, drawing on the work in the preceding chapters and using those results in a novel way to model our toroidal dipole. We theoretically studied light-induced interactions in a toroidal metamolecule that comprised closely-spaced, strongly-coupled plasmonic nanorods. The interactions lead to collective excitation eigenmodes that exhibit collective resonance frequencies, linewidths and line shifts. When the nanorod pairs are pointing radially outwards, one of the collective eigenmodes is identified as a toroidal dipole mode. We provided simple criteria to optimize a structural asymmetry of the metamolecule that allows a strong excitation of the toroidal dipole mode by a simple, linearly-polarized, light beam. By analyzing a specific eight-rod case, we have shown how even small asymmetries lead to a large proportion of the total excitation to be found in the toroidal dipole mode.

By comparing the point dipole approximation to a finite-size resonator model, we have shown that the point dipole approximation is sufficient to model interacting nanorods for large inter-rod separations, providing accurate descriptions when the layer and radial separations satisfy $ky \gtrsim \pi/3$ and $ks \gtrsim \pi/2$. For more closely-spaced rods the nanorods' finite length and thickness become increasingly important.

Chapter 6

Conclusions and future work

6.1 Summary

In this thesis, we have analyzed the EM interactions of plasmonic resonators with an incident EM field and the EM fields scattered by the resonators' themselves. We have shown how, through careful design of the resonators, normally subradiant collective modes can be excited over the more dominant superradiant collective modes. In particular, we have shown how we excite the toroidal dipole collective mode in a toroidal metamolecule. Also, we have shown how the toroidal excitation is achieved with readily available linearly-polarized light, and that the toroidal excitation shows as a Fano resonance in the forward scattered light.

We developed two complementary models to analyze the interactions of the resonators: a point multipole model; and a finite-size model accounting for the geometry and size of individual resonators. Firstly, in Chapter 2, we reviewed the general model of closely spaced resonators interacting with themselves and an incident EM field. Additionally, we reviewed the point electric and magnetic dipole approximation of the resonators' scattered EM fields.

In Chapter 3, we introduced the electric quadrupole contribution to the point multipole approximation of a resonator, and its interactions with other multipole moments. Additionally, we showed how simple electric dipole systems can be approximated by higher order multipoles. We analyzed in detail systems comprising parallel electric dipoles, and found that under certain conditions these can be closely approximated by interacting magnetic dipoles and electric quadrupoles.

In Chapter 4, we approximated the resonators in our systems as nanorods and showed that when the separation between nanorods is large, they can be approximated as point electric dipoles. We developed a model that accounted for the finite-size of the resonators when the separations were small. By using the analogy of electric dipoles, we were able to show that closely spaced parallel nanorods also exhibited an effective current circulation, hence an effective magnetic dipole and electric quadrupole moment.

In Chapter 5, we presented novel work analyzing a toroidal metamolecule comprising closely spaced, strongly-coupled, plasmonic nanorods. The nanorods themselves can be approximated as single point electric dipoles when the relative separation is large enough, $ks > \pi/2$. The metamolecule exhibits a number collective modes of oscillation depending on the number of resonators. When arranged in the toroidal structure investigated, the most subradiant mode exhibited is the toroidal dipole mode. We have provided optimization protocols for the structural asymmetry of the nanorods that will allow the toroidal dipole mode to be strongly excited by linearly polarized light which is readily available to experimentalists. Though our toroidal metamolecule comprised only eight nanorods, the model used may be easily extrapolated to account for greater numbers of nanorods.

6.2 Future work

In this thesis, we have developed a model that has been utilized to analyze the interactions of the resonators comprising a toroidal metamolecule. When the relative separations of the resonators are large, the individual nanorods can be approximated as point electric dipole resonators, neglecting the resonators' finite-sizes. When the separations become small, the finite-size can no longer be ignored. We can readily scale our model to analyze an ensemble of N toroidal metamolecules, each comprising N' resonators. Our point electric dipole model will have an $(NN') \times (NN')$ coupling matrix, with NN' collective modes. The mode corresponding to each metamolecule oscillating in the toroidal dipole mode must then be carefully identified and analyzed.

In Chapter 3, we showed how two parallel antisymmetrically excited electric dipoles can be approximated as a single resonator with both magnetic dipole and electric quadrupole moments. In our example of a toroidal metamolecule in Chapter 5, we employed $N = 8$ nanorods arranged in parallel pairs, and utilized the point electric dipole approximation to carry out the analysis. A next step, is to extend the work of Chapter 3, and approximate each parallel pair of electric dipoles as a single resonator with a magnetic dipole moment and electric quadrupole moment. Rather than an 8×8 coupling matrix, we would then have an 4×4 coupling matrix. One may then compare the electric dipole approximation to the magnetic dipole and electric quadrupole approximation and determine the validity of both models.

For an ensemble of toroidal metamolecules, a natural progression is to approximate the toroidal metamolecule as a single resonator with a point toroidal dipole source. The coupling matrix for an ensemble of toroidal metamolecules, in our model, is then an $N \times N$ matrix of N interacting point toroidal dipole resonators (rather than the

$(NN') \times (NN')$ matrix in the electric dipole approximation); a significant simplification. To reach this model of interacting point toroidal dipole sources, one must first develop the theoretical model. This will include how the scattered EM fields from toroidal dipole sources drive the charge and current sources of other multipole sources, including: electric dipoles; magnetic dipoles; electric quadrupoles; and toroidal dipoles. The self interaction of toroidal dipole sources will result in the radiative emission rate of the toroidal dipole [$\Gamma_{\mathrm{T1},j}$, in our notation], and an analytical expression for this must be determined.

The computational efficiency of our model lends itself to large ensembles of resonators. When current programs, e.g., Comsol, are employed to model the interactions between resonators. Maxwell's equations must be solved for each resonator and typically some finite difference solver is then used for an ensemble. Each additional resonator increases the degree of freedom. Our model can capture the fundamental physics, such as resonance frequency and radiative decay rate, of the resonators while retaining its efficiency and allowing the formulation of optimization protocols useful for the design of experiments. The insights gained can provide information and explanations for experimentalists.

Appendix A

Common symbols

Symbol	Description	SI Units	Page
$\mathbf{B}$	Magnetic induction	T	8
b	Dynamic variable	C s F$^{-1/2}$	18
C	Capacitance	F	17
$\mathcal{C}$	Coupling matrix	s^{-1}	19
$\mathbf{D}$	Electric displacement field	C m^{-2}	8
$\mathbf{E}$	Electric field	V m^{-1}	8
$\mathcal{E}$	Emf	V	18
ϵ	Permittivity	F m^{-1}	9
ϵ_{r}	Relative permittivity	n/a	12
ϵ_{∞}	Bound electron permittivity	n/a	12
Γ, γ	Decay rate	s^{-1}	19,20
$\mathbf{H}$	Magnetic field	A m^{-1}	8
I	Current	Q s^{-1}	17
$\mathbf{J}$	Current density	A m^{-2}	8
$\mathbf{J}_{\mathrm{f}}$	Free current density	Am^{-2}	8
$\mathbf{J}_{\mathrm{tot}}$	Total current density	A m^{-2}	8
L	Inductance	H	17
λ	wavelength	m	20
$\mathbf{M}$	Magnetization	A m^{-1}	9
$\mathbf{m}$	Magnetic dipole moment	m^{2}	9
μ	Permeability	H m^{-1}	9
ω	Angular frequency	Rads s^{-1}	10
ω_p	Plasma frequency	Rads s^{-1}	12
$\mathbf{P}$	Polarization	C m^{-2}	8

Symbol	Description	SI Units	Page
P	Radiated power	$\mathrm{W\,m^{-2}}$	9
$\mathbf{p}$	Electric dipole moment	m	9
Φ	Magnetic flux	A m	18
ϕ	Conjugate momentum	$\mathrm{C\ H^{1/2}\ F^{-1/2}}$	18
Q	Charge	C	17
$\mathbf{r}$	location vector	n/a	9
ρ	Charge density	$\mathrm{C\,m^{-3}}$	8
ρ_{f}	Free charge density	$\mathrm{Cm^{-3}}$	8
ρ_{tot}	Total charge density	$\mathrm{C\,m^{-3}}$	8
$\mathbf{t}$	Toroidal dipole moment	$\mathrm{m^3}$	9
$\mathbf{v}$	Eigenvector	n/a	20
ξ	Eigenvalue	n/a	20

Table A.1: List of symbols, their SI units where appropriate, and page number where the symbol is first introduced. For the SI unit abbreviation see Table A.2.

SI unit	Abbreviation
Ampere	A $(\mathrm{C\,s^{-1}})$
Coulomb	C
Farad	F $(\mathrm{A\,s\,V^{-1}})$
Henry	H $(\mathrm{kg\,m^2\,s^{-2}\,A^{-2}})$
Hertz	Hz
Joule	J $(\mathrm{kg\,m^2\,s^{-2}})$
Kilogram	kg
Metre	m
Ohm	Ω
Radian	rads
Second	s
Tesla	T $(\mathrm{V\,s\,m^{-2}})$
Volt	V $(\mathrm{kg\,m^2\,C^{-1}\,s^{-2}})$
Watt	$\mathrm{J\,s^{-1}}$
Weber	Wb $(\mathrm{V\,s})$

Table A.2: SI unit abbreviations.

Appendix B

Special functions

In this appendix, we collate the special functions used throughout this thesis for easy reference.

B.1 Bessel functions

Bessel functions $J_n(x) = (-1)^m J_{-n}(x)$ are linearly independent solutions to Bessel's differential equation,

$$\frac{\mathrm{d}^2 R}{\mathrm{d}x^2} + \frac{1}{x}\frac{\mathrm{d}R}{\mathrm{d}x} + \left[1 - \frac{n^2}{x^2}\right] R = 0\,, \tag{B.1}$$

in the region $x \geq 0$ for integer values of n. An associated solution is the Neumann function $N_n(x)$,

$$N_n(x) = \frac{J_n(x)\cos nx - J_{-n}(x)}{\sin n\pi}\,. \tag{B.2}$$

The integral representation of $J_n(x)$ is [91]

$$J_n(x) = \frac{1}{2\pi}\int_0^{2\pi} \mathrm{d}\psi\, e^{i(x\sin\psi - n\psi)}\,. \tag{B.3}$$

Hankel functions $H_n^{(1)}(x)$ and $H_n^{(2)}(x)$, of the first and second kind respectively, are related to the Bessel and Neumann functions by

$$H_n^{(1)}(x) = J_n(x) + iN_n(x)\,, \tag{B.4}$$

$$H_n^{(2)}(x) = J_n(x) - iN_n(x)\,. \tag{B.5}$$

$H_n^{(1)}(x)$ behaves asymptotically like an outgoing wave, while $H_n^{(2)}(x)$ behaves asymptotically like on incoming wave.

B.2 Spherical Bessel functions

Real valued spherical Bessel $j_n(x)$ and spherical Neumann $n_n(x)$ functions are defined by

$$j_n(x) = \sqrt{\frac{\pi}{2x}} J_{n+\frac{1}{2}}(x)\,, \tag{B.6}$$

$$n_n(x) = \sqrt{\frac{\pi}{2x}} N_{n+\frac{1}{2}}(x)\,. \tag{B.7}$$

Explicit formulae for $j_n(x)$ and $n_n(x)$ are

$$j_n(x) = (-1)^n x^n \left(\frac{1}{x}\frac{\mathrm{d}}{\mathrm{d}x}\right)^n \frac{\sin(x)}{x}\,, \tag{B.8}$$

$$n_n(x) = -(-1)^n x^n \left(\frac{1}{x}\frac{\mathrm{d}}{\mathrm{d}x}\right)^n \frac{\cos(x)}{x}\,. \tag{B.9}$$

For small arguments

$$\lim_{x\to 0} j_n(x) = \frac{x^n}{(2n+1)!!}\,, \tag{B.10}$$

$$\lim_{x\to 0} n_n(x) = -\frac{(2n-1)!!}{x^{n+1}}\,. \tag{B.11}$$

Spherical Hankel functions of the first $h_n^{(1)}(x)$, and second $h_n^{(2)}(x)$ kind are defined as

$$h_n^{(1)}(x) = j_n(x) + i n_n(x)\,, \tag{B.12}$$

$$h_n^{(2)}(x) = j_n(x) - i n_n(x)\,. \tag{B.13}$$

The first few $h_n^{(1,2)}(x)$ are

$$h_0^{(1,2)}(x) = \mp i \frac{e^{ix}}{x}\,, \tag{B.14a}$$

$$h_1^{(1,2)}(x) = \mp \left[1 + \frac{i}{x}\right] \frac{e^{ix}}{x}\,, \tag{B.14b}$$

$$h_2^{(1,2)}(x) = \pm i \left[1 + \frac{3i}{x} - \frac{3}{x^2}\right] \frac{e^{ix}}{x}\,, \tag{B.14c}$$

$$h_3^{(1,2)}(x) = \pm \left[1 + \frac{6i}{x} - \frac{15}{x^2} - \frac{15i}{x^3}\right] \frac{e^{ix}}{x}\,, \tag{B.14d}$$

$$h_4^{(1,2)}(x) = \mp i \left[1 + \frac{10i}{x} - \frac{45}{x^2} - \frac{105i}{x^3} + \frac{105}{x^4}\right] \frac{e^{ix}}{x}\,. \tag{B.14e}$$

A simple relationship between spherical Hankel functions $n \geq 1$ is

$$\frac{2n+1}{x} h_n^{(1,2)}(x) = h_{n+1}^{(1,2)}(x) + h_{n-1}^{(1,2)}(x)\,. \tag{B.15}$$

B.3 Spherical harmonics

Spherical harmonics $Y_{lm}(\theta,\phi)$, with complex conjugate $Y^*_{lm}(\theta,\phi)=(-1)^{-m}Y_{l,-m}(\theta,\phi)$, are eigenfunctions of the eigenvalue problem

$$\frac{1}{\sin\theta}\frac{\partial}{\partial\theta}\left(\sin\theta\frac{\partial Y}{\partial\theta}\right)+\frac{1}{\sin^2\theta}\frac{\partial^2 Y}{\partial\theta^2}=-l(l+1)Y\,, \tag{B.16}$$

defined on the sphere with the boundary conditions that $Y_{lm}(\theta,\phi)$ be finite and single valued. The spherical harmonics can be written in terms of the associated Legendre polynomials as

$$Y_{lm}(\theta,\phi)=\sqrt{\frac{2l+1}{4\pi}\frac{(l-m)!}{(l+m)!}}P_l^m(\cos\theta)e^{im\phi} \qquad m\geq 0\,. \tag{B.17}$$

The first few scalar spherical harmonics $Y_{lm}(\theta,\phi)$ (in Cartesian coordinates) are,

$$Y_{00}=\frac{1}{\sqrt{4\pi}}\,, \tag{B.18a}$$

$$Y_{10}=\sqrt{\frac{3}{4\pi}}\frac{z}{r}\,, \tag{B.18b}$$

$$Y_{1\pm1}=\mp\sqrt{\frac{3}{8\pi}}\frac{x\pm iy}{r}\,, \tag{B.18c}$$

$$Y_{20}=\sqrt{\frac{5}{16\pi}}\frac{3z^2-r^2}{r^2}\,, \tag{B.18d}$$

$$Y_{2\pm1}=\pm\sqrt{\frac{15}{8\pi}}\frac{z(z\pm iy)}{r^2}\,, \tag{B.18e}$$

$$Y_{2\pm2}=\sqrt{\frac{15}{32\pi}}\frac{(x\pm iy)^2}{r^2}\,. \tag{B.18f}$$

Appendix C

Spherical multipole expansion

In this appendix, we obtain a spherical multipole decomposition of the dynamic EM fields $\mathbf{E}(\mathbf{r},t)$ and $\mathbf{B}(\mathbf{r},t)$, external to the source charge and current distributions $\rho(\mathbf{r},t)$ and $\mathbf{J}(\mathbf{r},t)$, respectively. Formal derivations can be found in many texts, see, e.g., Reference 39, 40, 63. In addition, Gray [92, 93] provides an excellent treatment of the spherical multipole expansion in the longwave limit using Debye potentials. Here, we provide a brief overview in order to supplement the main text of the thesis.

We assume all sources, and the EM fields they produce, vary harmonically in time with frequency $\omega = k/c$ (e.g., $\mathbf{E}(\mathbf{r},t) = \mathbf{E}(\mathbf{r})e^{-i\omega t}$). The microscopic form of Maxwell's equations are [63];

$$\nabla\cdot \mathbf{E} = \frac{\rho}{\epsilon_0}\,, \tag{C.1}$$

$$\nabla \times \mathbf{E} = -\frac{\partial \mathbf{B}}{\partial t}\,, \tag{C.2}$$

$$\nabla\cdot \mathbf{B} = 0\,, \tag{C.3}$$

$$\nabla \times \mathbf{B} = \mu_0 \mathbf{J} + \frac{1}{c^2}\frac{\partial \mathbf{E}}{\partial t}\,, \tag{C.4}$$

where ϵ_0 and μ_0 are the permittivity and permeability, respectively, of free space and $c = (\epsilon_0\mu_0)^{-1/2}$ is the speed of light in a vacuum. The fields and their sources are connected through the inhomogeneous Helmholtz wave equations. Taking the curl of equation (C.2) and inserting equation (C.4) (and vice versa), the vector inhomegeneous Helmholtz wave equations for $\mathbf{E}$ and $\mathbf{B}$, are [39, 63]

$$\left(\nabla^2 + k^2\right)\mathbf{E} = \frac{1}{\epsilon_0}\nabla\rho + \mu_0\frac{\partial \mathbf{J}}{\partial t}\,, \tag{C.5}$$

$$\left(\nabla^2 + k^2\right)\mathbf{B} = -\mu_0\nabla \times \mathbf{J}\,. \tag{C.6}$$

The radial components of the time harmonic electric field and magnetic flux, $\mathbf{r}\cdot\mathbf{E}$ and $\mathbf{r}\cdot\mathbf{B}$, both satisfy equations (C.5) and (C.6), resulting in [63]

$$(\nabla^2 + k^2)\mathbf{r}\cdot\mathbf{E} = \frac{1}{\epsilon_0}\Big[2\rho + \mathbf{r}\cdot\nabla\rho\Big] - i\omega\mu_0\mathbf{r}\cdot\mathbf{J}\,, \tag{C.7}$$

$$(\nabla^2 + k^2)\mathbf{r}\cdot\mathbf{B} = -\mu_0\mathbf{r}\cdot\nabla\times\mathbf{J}\,, \tag{C.8}$$

where we have used the vector identity (for some vector field $\mathbf{F}$),

$$\mathbf{r}\cdot(\nabla^2\mathbf{F}) = \nabla^2(\mathbf{r}\cdot\mathbf{F}) - 2\nabla\cdot\mathbf{F}\,, \tag{C.9}$$

and Gauss's law [equation (C.1)]. The solutions to equations (C.7) and (C.8) are the radial components [63]

$$\mathbf{r}\cdot\mathbf{E} = \frac{1}{\epsilon_0 c}\int \mathrm{d}^3r'\, G_0(\mathbf{r},\mathbf{r}')\Big[ik(\mathbf{r}'\cdot\mathbf{J}(\mathbf{r}')) - c(2 + \mathbf{r}'\cdot\nabla')\rho(\mathbf{r}')\Big]\,, \tag{C.10}$$

$$\mathbf{r}\cdot\mathbf{B} = \mu_0\int \mathrm{d}^3r'\, G_0(\mathbf{r},\mathbf{r}')\Big[\mathbf{r}'\cdot\nabla'\times\mathbf{J}(\mathbf{r}')\Big]\,, \tag{C.11}$$

where $G_0(\mathbf{r},\mathbf{r}')$ is the outgoing free space Green's function [63]

$$G_0(\mathbf{r},\mathbf{r}') = \frac{e^{ik|\mathbf{r}-\mathbf{r}'|}}{|\mathbf{r}-\mathbf{r}'|}\,, \tag{C.12}$$

a solution to the inhomogeneous Helmholtz equation

$$(\nabla^2 + k^2)\frac{e^{ik|\mathbf{r}-\mathbf{r}'|}}{|\mathbf{r}-\mathbf{r}'|} = -4\pi\delta(\mathbf{r}-\mathbf{r}')\,. \tag{C.13}$$

The spherical expansion of equation (C.12) in the region $r' < r$ is [63]

$$\frac{e^{ik|\mathbf{r}-\mathbf{r}'|}}{|\mathbf{r}-\mathbf{r}'|} = ik\sum_{l=0}^{\infty}\sum_{m=-l}^{l} j_l(kr')h_l^{(1)}(kr)Y^*_{lm}(\theta',\phi')Y_{lm}(\theta,\phi)\,, \tag{C.14}$$

where: $j_l(kr)$ and $h_l^{(1)}(kr)$ are spherical Bessel and Hankel (first kind) functions, respectively, of order l; and $Y_{lm}(\theta,\phi)$ are the spherical harmonics of order lm, see Appendix B. Equations (C.10) and (C.11) are valid anywhere in space [92] and may be expanded in spherical harmonics [92]

$$\mathbf{r}\cdot\mathbf{E} = (\mathbf{r}\cdot\mathbf{E})_{lm}h_l^{(1)}(kr)Y_{lm}(\theta,\phi)\,, \tag{C.15}$$

$$\mathbf{r}\cdot\mathbf{B} = (\mathbf{r}\cdot\mathbf{B})_{lm}h_l^{(1)}(kr)Y_{lm}(\theta,\phi)\,. \tag{C.16}$$

The expansion coefficients $(\mathbf{r}\cdot\mathbf{E})_{lm}$ and $(\mathbf{r}\cdot\mathbf{B})_{lm}$ are closely related to the charge and current densities. To visualize this, and determine the EM fields $\mathbf{E}$ and $\mathbf{B}$ in source free regions, we introduce the expansion coefficients $\Lambda^{(\mathrm{E})}$ and $\Lambda^{(\mathrm{M})}$ (these are sometimes referred to as Debye potentials [92]). The superscripts (E) and (M) are so called because, as we show later, they arise due electric and magnetic multipole moments, respectively. Maxwell's equations in source free regions reduce to [63]

$$\mathbf{E} = \frac{ic}{k}\nabla\times\mathbf{B} \qquad \text{and} \qquad \mathbf{B} = -\frac{i}{k}\nabla\times\mathbf{E}\,, \tag{C.17}$$

with $\nabla\cdot\mathbf{E} = \nabla\cdot\mathbf{B} = 0$. These source free equations are satisfied by [63, 92]

$$\mathbf{E} = \mathbf{L}\Lambda^{(\mathrm{M})} + \frac{i}{k}\nabla\times\mathbf{L}\Lambda^{(\mathrm{E})}\,, \tag{C.18}$$

$$c\mathbf{B} = \mathbf{L}\Lambda^{(\mathrm{E})} - \frac{i}{k}\nabla\times\mathbf{L}\Lambda^{(\mathrm{M})}\,, \tag{C.19}$$

where $\mathbf{L} = -i\mathbf{r}\times\nabla$ is the angular momentum operator, with operator identities

$$\nabla\cdot\mathbf{L} = 0 \qquad \text{and} \qquad \nabla\times(\nabla\times\mathbf{L}) = -\nabla^2\mathbf{L}\,. \tag{C.20}$$

The Debye potentials $\Lambda^{(\mathrm{E})}$ and $\Lambda^{(\mathrm{M})}$ are required to satisfy the homogeneous Helmholtz scalar wave equation [63], i.e., $(\nabla^2 + k^2)\Lambda^{(\mathrm{E,M})} = 0$. Thus, $\Lambda^{(\mathrm{E,M})}$ must be expandable as sums of elementary outgoing solutions [92], i.e.,

$$\Lambda^{(\mathrm{E,M})} = \sum_{l=0}^{\infty}\sum_{m=-1}^{l}\Lambda_{lm}^{(\mathrm{E,M})}h_l^{(1)}(kr)Y_{lm}(\theta,\phi)\,. \tag{C.21}$$

Taking the dot product of $\mathbf{r}$ with equations (C.18) and (C.19), we see that the radial components of the EM fields are due to the $\nabla\times\mathbf{L}$ terms, because $\mathbf{r}\cdot\mathbf{L} = 0$ and $\mathbf{r}\cdot\nabla\times\mathbf{L} = iL^2$, where $L^2 \equiv L_x^2 + L_y^2 + L_z^2$. The radial components are thus [63]

$$\mathbf{r}\cdot\mathbf{E} = -\frac{1}{k}L^2\Lambda^{(\mathrm{E})} \quad \text{and} \quad \mathbf{r}\cdot c\mathbf{B} = \frac{1}{k}L^2\Lambda^{(\mathrm{M})}\,. \tag{C.22}$$

Using the relationship $L^2Y_{lm}(\theta,\phi) = l(l+1)Y_{lm}(\theta,\phi)$, then [66]

$$\Lambda_{lm}^{(\mathrm{E})} = -\frac{k}{l(l+1)}(\mathbf{r}\cdot\mathbf{E})_{lm}\,, \tag{C.23}$$

$$\Lambda_{lm}^{(\mathrm{M})} = \frac{k}{l(l+1)}(\mathbf{r}\cdot c\mathbf{B})_{lm}\,. \tag{C.24}$$

The moments $\Lambda_{lm}^{(\mathrm{E})}$ and $\Lambda_{lm}^{(\mathrm{M})}$ are called the spherical electric and magnetic multipole moments, respectively [39, 63]. They are commonly written [63]

$$\Lambda_{lm}^{(\mathrm{E})} = -\frac{ik^2}{\epsilon_0 cl(l+1)}\int \mathrm{d}^3r\, j_l(kr)Y_{lm}^*(\theta,\phi)\big[ik\mathbf{r}\cdot\mathbf{J}(\mathbf{r}) + c(2+\mathbf{r}\cdot\nabla)\rho(\mathbf{r})\big]\,, \tag{C.25}$$

$$\Lambda_{lm}^{(\mathrm{M})} = \frac{ick^2\mu_0}{l(l+1)}\int \mathrm{d}^3r\,\big[\mathbf{r}\times\mathbf{J}(\mathbf{r})\big]\cdot\nabla\Big[j_l(kr)Y_{lm}^*(\theta,\phi)\Big]\,. \tag{C.26}$$

There are different, but equivalent, ways of writing the integrals in equations (C.25) and (C.26), see, for example, Reference 63 for different expressions of $\Lambda_{lm}^{(\mathrm{M})}$. In the form presented in equation (C.26), the operator ∇ acts on the product $j_l(kr)Y^*_{lm}(\theta,\phi)$, this is useful for easily determining the lth order spherical magnetic multipole moment in terms of $\mathbf{r}\times\mathbf{J}(\mathbf{r})$. In equation (C.25), however, the operator ∇ acts on ρ. A more useful, equivalent, expression for $\Lambda^{(\mathrm{E})}_{lm}$ is obtained through integration by parts and using Gauss's theorem. We use the identity

$$\nabla\cdot(f\mathbf{F}) = f(\nabla\cdot\mathbf{F}) + \mathbf{F}\cdot(\nabla f)\,, \tag{C.27}$$

for some vector $\mathbf{F}$ and scalar function f, to write

$$\Lambda^{(\mathrm{E})}_{lm} = -\frac{ik^2}{\epsilon_0 cl(l+1)}\int \mathrm{d}^3r\, Y^*_{lm}(\theta,\phi)\Big[ikj_l(kr)\mathbf{r}\cdot\mathbf{J}(\mathbf{r}) + c\rho(\mathbf{r})\frac{\partial}{\partial r}\big[rj_l(kr)\big]\Big]\,. \tag{C.28}$$

The complete $\mathbf{E}$ and $\mathbf{B}$ fields in spherical multipole form are thus [63]

$$\mathbf{E} = \sum_{l=0}^{\infty}\sum_{m=-1}^{l}\Big[\Lambda^{(\mathrm{M})}_{lm}\mathbf{L}h^{(1)}_l(kr)Y_{lm}(\theta,\phi) + \frac{i}{k}\Lambda^{(\mathrm{E})}_{lm}\nabla\times\mathbf{L}h^{(1)}_l(kr)Y_{lm}(\theta,\phi)\Big]\,, \tag{C.29}$$

$$c\mathbf{B} = \sum_{l=0}^{\infty}\sum_{m=-1}^{l}\Big[\Lambda^{(\mathrm{E})}_{lm}\mathbf{L}h^{(1)}_l(kr)Y_{lm}(\theta,\phi) - \frac{i}{k}\Lambda^{(\mathrm{M})}_{lm}\nabla\times\mathbf{L}h^{(1)}_l(kr)Y_{lm}(\theta,\phi)\Big]\,. \tag{C.30}$$

C.1 Longwave length limit

Traditionally, in texts treating the spherical multipole expansion, the long wavelength limit (where the size a of the source is small ($ka \ll 1$)) is applied to equations (C.26) and (C.28). In the long wavelength limit, the spherical Bessel function takes the form

$$\lim_{kr\to 0} j_l(kr) = \frac{(kr)^l}{(2l+1)!!}\,. \tag{C.31}$$

The magnetic multipole moment approaches

$$\lim_{ka\to 0}\Lambda^{(\mathrm{M})}_{lm} = \frac{ick^{l+2}\mu_0}{l(2l+1)!!}M_{lm}\,, \tag{C.32}$$

where M_{lm} is the magnetostatic multipole moment defined as

$$M_{lm} = \frac{1}{l+1}\int \mathrm{d}^3r\,\big[\mathbf{r}\times\mathbf{J}(\mathbf{r})\big]\cdot\nabla\big[r^lY^*_{lm}(\theta,\phi)\big]\,. \tag{C.33}$$

The form of equation (C.33) allows one to immediately see that the $l=0$ term of the magnetostatic multipole moments vanishes. The magnetic dipole ($l=1$) is the leading order term of equation (C.33). The distinct $l=1, m=0,\pm1$ terms of equation (C.33) are

$$M_{10} = \frac{1}{2}\sqrt{\frac{3}{4\pi}}\int \mathrm{d}^3r\,\big[\mathbf{r}\times\mathbf{J}(\mathbf{r})\big]z = \sqrt{\frac{3}{4\pi}}m_z\,, \tag{C.34}$$

$$M_{1,\pm1} = \mp\frac{1}{2}\sqrt{\frac{3}{8\pi}}\int \mathrm{d}^3r\,\big[\mathbf{r}\times\mathbf{J}(\mathbf{r})\big](x\mp iy) = \mp\sqrt{\frac{3}{4\pi}}(m_x\mp im_y)\,, \tag{C.35}$$

where m_x, m_y and m_z are the Cartesian components of the magnetic dipole moment $\mathbf{m}$, normally defined as [39]

$$\mathbf{m} = \frac{1}{2}\int \mathrm{d}^3r\,\mathbf{r}\times\mathbf{J}(\mathbf{r})\,. \tag{C.36}$$

In the longwave length limit, the continuity equation ($\nabla\cdot\mathbf{J} = i\omega\rho$) shows us $J/a \sim ck\rho \implies k\mathbf{r}\cdot\mathbf{J}/(c\rho) \sim (ka)^2$. Thus the first term in equation (C.28) is a factor of $(ka)^2$ lesser than the second term. Hence, in many texts [39, 40, 63], the first term in equation (C.28) is neglected and

$$\lim_{ka\to 0}\Lambda^{(\mathrm{E})}_{lm} = -\frac{ik^{l+2}}{4\pi\epsilon_0(2l-1)!!}Q_{lm}\,, \tag{C.37}$$

where Q_{lm} is the electrostatic multipole moment defined by [63]

$$Q_{lm} = \frac{4\pi}{(2l+1)}\int \mathrm{d}^3r\,\rho(\mathbf{r})r^lY^*_{lm}(\theta,\phi)\,. \tag{C.38}$$

The Cartesian components of the electric dipole ($l=1, m=0,\pm1$) term are given by

$$Q_{10} = \sqrt{\frac{4\pi}{3}}\int \mathrm{d}^3r\,\rho(\mathbf{r})z = \sqrt{\frac{4\pi}{3}}p_z\,, \tag{C.39}$$

$$Q_{1,\pm1} = \mp\sqrt{\frac{4\pi}{6}}\int \mathrm{d}^3r\rho(\mathbf{r})(x\mp iy) = \mp\sqrt{\frac{4\pi}{6}}(p_x\mp ip_y)\,, \tag{C.40}$$

where p_x, p_y and p_z are the Cartesian components of the electric dipole moment $\mathbf{p}$,

$$\mathbf{p} = \int \mathrm{d}^3r\,\mathbf{r}\rho(\mathbf{r})\,. \tag{C.41}$$

Appendix D

Electric quadrupole supporting calculations

In Chapter 3, we calculated the EM fields scattered from a point electric quadrupole source, and the interaction between these scattered EM fields and other: electric quadrupoles; electric dipoles; and magnetic dipoles. The scattered EM fields and the resulting emf and flux terms contain derivatives of the radiation kernel and cross kernel, equations (2.5) and (2.6). In this Appendix, we give the first derivatives of $\mathbf{G}(\mathbf{r})$ and $\mathbf{G}_\times(\mathbf{r})$ and the second derivatives of $\mathbf{G}(\mathbf{r})$.

D.1 Radiation kernel and cross kernel derivatives

The scattered electric $\mathbf{E}_{\mathrm{E2},j}$ and magnetic $\mathbf{H}_{\mathrm{E2},j}$ fields from the jth electric quadrupole are given in equations (3.9) and (3.10). These equations contain rank three tensors which are the gradients of $\mathbf{G}(\mathbf{r})$ and $\mathbf{G}_\times(\mathbf{r})$. Explicitly, these rank three tensors are

$$\begin{aligned}
\frac{\partial}{\partial r_\mu}\mathbf{G}(\mathbf{r}) = i\Bigg[&\left[\frac{1}{5}\frac{r_\mu}{r}\mathbf{I} + \frac{1}{5}\frac{\mathbf{r}\hat{\mathbf{r}}_\mu + \hat{\mathbf{r}}_\mu\mathbf{r}}{r} - \frac{r_\mu}{r}\frac{\mathbf{r}\mathbf{r}}{r^2}\right] h_3^{(1)}(kr) \\
&- \left[\frac{12}{15}\frac{r_\mu}{r}\mathbf{I} - \frac{1}{5}\frac{\mathbf{r}\hat{\mathbf{r}}_\mu + \hat{\mathbf{r}}_\mu\mathbf{r}}{r}\right] h_1^{(1)}(kr)\Bigg], \qquad \text{(D.1)} \\
\frac{\partial}{\partial r_\mu}\mathbf{G}_\times(\mathbf{r}) = \frac{1}{r^2}&\Big[r_\eta\hat{\mathbf{r}}_\nu\left(\mathbf{r}_\mu + \mathbf{r}_\nu + \mathbf{r}_\eta\right) - r_\nu(\hat{\mathbf{r}}_\eta\left(\mathbf{r}_\mu + \mathbf{r}_\nu + \mathbf{r}_\eta\right)\Big] h_2^{(1)}(kr) \\
&- \frac{1}{r}\Big[\hat{\mathbf{r}}_\nu\hat{\mathbf{r}}_\eta - \hat{\mathbf{r}}_\eta\hat{\mathbf{r}}_\nu\Big] h_1^{(1)}(kr)\,. \qquad \text{(D.2)}
\end{aligned}$$

Here: r_μ is Cartesian component $\mu = x, y, z$ of the vector $\mathbf{r}$; $\mathbf{r}\mathbf{r}$ is the outer product of $\mathbf{r}$ with itself; $\mathbf{I}$ is the identity matrix; and $\hat{\mathbf{r}}_\mu\mathbf{r}$ is the outer product of the unit vector $\hat{\mathbf{r}}_\mu$ in the Cartesian direction $\mu = x, y, z$ with the vector $\mathbf{r}$; and $h_n^{(1)}(kr)$ are the jth order spherical Hankel functions of the first kind, see equation (B.14).

The interaction between two separate electric quadrupoles i and j results in an effective emf $\mathcal{E}_{i,j}^{\mathrm{sc,E2}}$, see equations (3.39)–(3.41). Equation (3.41) describes the interaction matrix $\mathcal{G}_{\mathrm{E2}}$ whose off-diagonal elements are the interactions between two electric quadrupoles, taking into account their relative locations and orientations only. $\mathcal{G}_{\mathrm{E2}}$ is a contraction of the quadrupole moment tensors $\hat{A}_{\alpha\beta,m}$ and $\hat{A}_{\mu\nu,n}$ and a rank four tensor. The rank four tensor contains second order derivatives of $\mathbf{G}(\mathbf{r})$, these can be written

$$\begin{aligned}\left.\frac{\partial^2}{\partial r_\mu \partial r_\mu}\right|_{r_\mu = r_\mu} \mathbf{G}(\mathbf{r}) = i\Bigg\{ & \Bigg[\frac{r_\mu^2}{r^4}\mathbf{rr} - \frac{1}{7r^2}\left(\mathbf{rr} + r_\mu^2\mathbf{I} - 4\hat{\mathbf{r}}_\mu\hat{\mathbf{r}}_\mu - 2\left[\mathbf{r}_\mu\mathbf{r}_\nu + \mathbf{r}_\nu\mathbf{r}_\mu\right]\right) \\ & + \frac{1}{35}\left(\mathbf{I} + 2\hat{\mathbf{r}}_\mu\hat{\mathbf{r}}_\mu\right)\Bigg] h_4^{(1)}(kr) - \Bigg[\frac{1}{7r^2}\Big[\mathbf{rr} + 2\left(\mathbf{r}_\mu\mathbf{r}_\nu + \mathbf{r}_\nu\mathbf{r}_\mu\right) \\ & + r_\mu^2\mathbf{I} + 3\mathbf{r}_\mu\mathbf{r}_\mu\Big] + \frac{5}{21}\left(\mathbf{I} + 4\hat{\mathbf{r}}_\mu\hat{\mathbf{r}}_\mu\right)\Bigg] h_2^{(1)})kr) \\ & - \frac{4}{15}\left[\mathbf{I} + 2\hat{\mathbf{r}}_\mu\hat{\mathbf{r}}_\mu\right] h_0^{(1)}(kr)\Bigg\}\,, \end{aligned} \tag{D.3}$$

$$\begin{aligned}\left.\frac{\partial^2}{\partial r_\mu \partial r_\nu}\right|_{r_\mu \neq r_\nu} \mathbf{G}(\mathbf{r}) = i\Bigg\{ & \Bigg[\frac{r_\mu r_\nu}{r^4}\mathbf{rr} - \frac{1}{7r^2}\left[r_\mu\left(\mathbf{r}\hat{\mathbf{r}}_\nu + \hat{\mathbf{r}}_\nu\mathbf{r}\right) + r_\nu\left(\mathbf{r}\hat{\mathbf{r}}_\mu + \hat{\mathbf{r}}_\mu\mathbf{r}\right) + r_\mu r_\nu\mathbf{I}\right] \\ & + \frac{1}{35}\left(\hat{\mathbf{r}}_\mu\hat{\mathbf{r}}_\nu + \hat{\mathbf{r}}_\nu\hat{\mathbf{r}}_\mu\right)\Bigg] h_4^{(1)}(kr) - \Bigg[\frac{1}{7r^2}\Big(r_\mu\left[\mathbf{r}\hat{\mathbf{r}}_\nu + \hat{\mathbf{r}}_\nu\mathbf{r}\right] \\ & + r_\nu\left[\mathbf{r}\hat{\mathbf{r}}_\mu + \hat{\mathbf{r}}_\mu\mathbf{r} - 6r_\mu\mathbf{I}\right]\Big) - \frac{2}{21}\left(\hat{\mathbf{r}}_\mu\hat{\mathbf{r}}_\nu + \hat{\mathbf{r}}_\nu\hat{\mathbf{r}}_\mu\right)\Bigg] h_2^{(1)}(kr) \\ & + \frac{1}{15}\left[\hat{\mathbf{r}}_\mu\hat{\mathbf{r}}_\nu + \hat{\mathbf{r}}_\nu\hat{\mathbf{r}}_\mu\right] h_0^{(1)}(kr)\Bigg\}\,. \end{aligned} \tag{D.4}$$

The associated spherical Hankel functions $h_n^{(1)}(kr)$ are, again, defined in equations (B.14).

D.2 Electric quadrupole radiated power

In Section 3.1, we obtain an expression for the electric quadrupole radiative emission rate $\Gamma_{\mathrm{E2},j}$, by calculating the radiated power P_{E2}, see equations (3.17) and (3.18). To arrive at equation (3.18), we had to evaluate the integral of $|\hat{\mathbf{r}} \times \mathbf{q}_j(\hat{\mathbf{r}})|^2$, over all angles. To do so, we note the Cartesian coordinate identity [63]

$$|\hat{\mathbf{r}} \times \mathbf{q}_j(\hat{\mathbf{r}})|^2 = \sum_{\alpha\beta\eta} q_{\alpha\beta,j}\hat{r}_\beta q^*_{\alpha\eta,j}\hat{r}_\eta - \sum_{\alpha\beta\eta\nu} \hat{r}_\alpha q_{\alpha\beta,j}\hat{r}_\beta\hat{r}_\eta q^*_{\eta\nu,j}\hat{r}_\nu\,. \tag{D.5}$$

The different $\hat{r}_\alpha$'s are direction cosines which obey the identities [63]

$$\int \mathrm{d}\Omega\, \hat{r}_\beta \hat{r}_\eta = \frac{4\pi}{3} \delta_{\beta\eta}\,, \tag{D.6}$$

$$\int \mathrm{d}\Omega\, \hat{r}_\alpha \hat{r}_\beta \hat{r}_\eta \hat{r}_\nu = \frac{4\pi}{15} \Big[\delta_{\alpha\beta}\delta_{\eta\nu} + \delta_{\alpha\eta}\delta_{\beta\nu} + \delta_{\alpha\nu}\delta_{\beta\eta} \Big]\,. \tag{D.7}$$

Evaluation of the integrals in equations (D.6) and (D.7), and summing over the Cartesian indices x, y and z, hence arrive at equation (3.18).

Appendix E

Two perpendicular pairs of point electric dipoles, supplementary figures

In this appendix, we provide additional figures showing the collective mode linewidths and line shifts of two perpendicular pairs of parallel electric dipoles (see Figure 3.9) and their corresponding effective point multipoles. The plots are included here for reference in order to aid the flow of the main text. In Figures E.1 and E.2, we vary the parameter l, when $ks = 2\pi/5$ and $ks = 2\pi$. In Figure E.3, we vary the parameter s when $kl = \pi/4$ and $kl = 2\pi$.

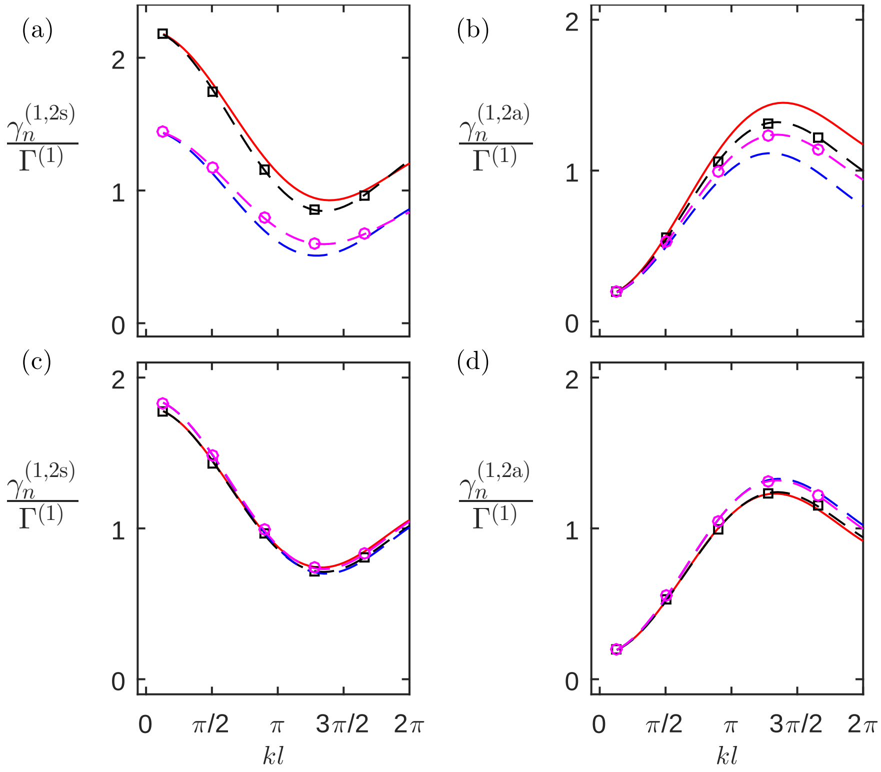

Figure E.1: The radiative resonance linewidth γ for the collective eigenmodes as a function of the separation parameter l, for two perpendicular pairs of point electric dipoles, with: (a) and (b) $ks = 2\pi/5$; and (c) and (d) $ks = 2\pi$. We show the linewidth $\gamma_n^{(1)}$ in the $N = 4$ point electric dipole model, with the different modes shown as: E1a–red solid line (a) and (c); E1s–blue dashed line (a) and (c); M1E2a–red solid line (b) and (d); and M1E2s–blue dashed line (b) and (d). We show the linewidth $\gamma_n^{(2s)}$ in the $N = 2$ effective electric dipole resonator model: antisymmetric (E1a) excitations–magenta dash circles (a) and (c); and symmetric (E1s) excitations–black dash squares (a) and (c). The linewidth $\gamma_n^{(2a)}$ in the $N = 2$ effective magnetic dipole–electric quadrupole resonator model: antisymmetric (M1E2a) excitations–magenta dash circles (b) and (d); and symmetric (M1E2s) excitations–black dash squares (b) and (d). The radiative losses of each electric dipole are $\Gamma_{\text{E1}} = 0.83\Gamma^{(1)}$, the ohmic losses are $\Gamma_{\text{O}} = 0.17\Gamma^{(1)}$.

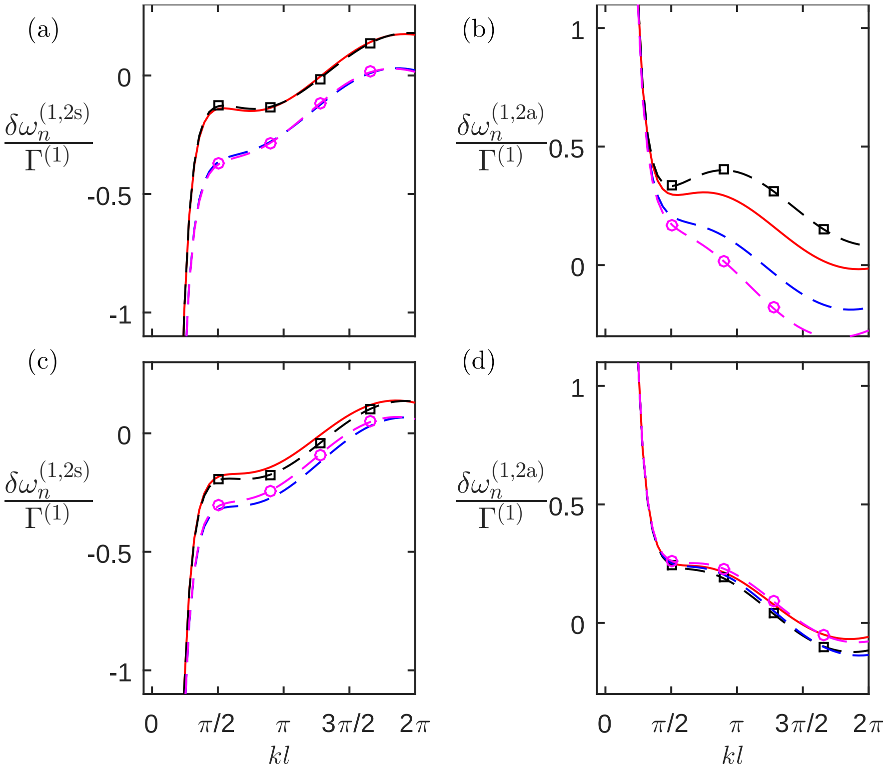

Figure E.2: The radiative resonance line shift $\delta\omega$ for the collective eigenmodes as a function of the separation parameter l, for two perpendicular pairs of point electric dipoles, with: (a) and (b) $ks = 2\pi/5$; and (c) and (d) $ks = 2\pi$. For plot descriptions, see Figure E.1 caption.

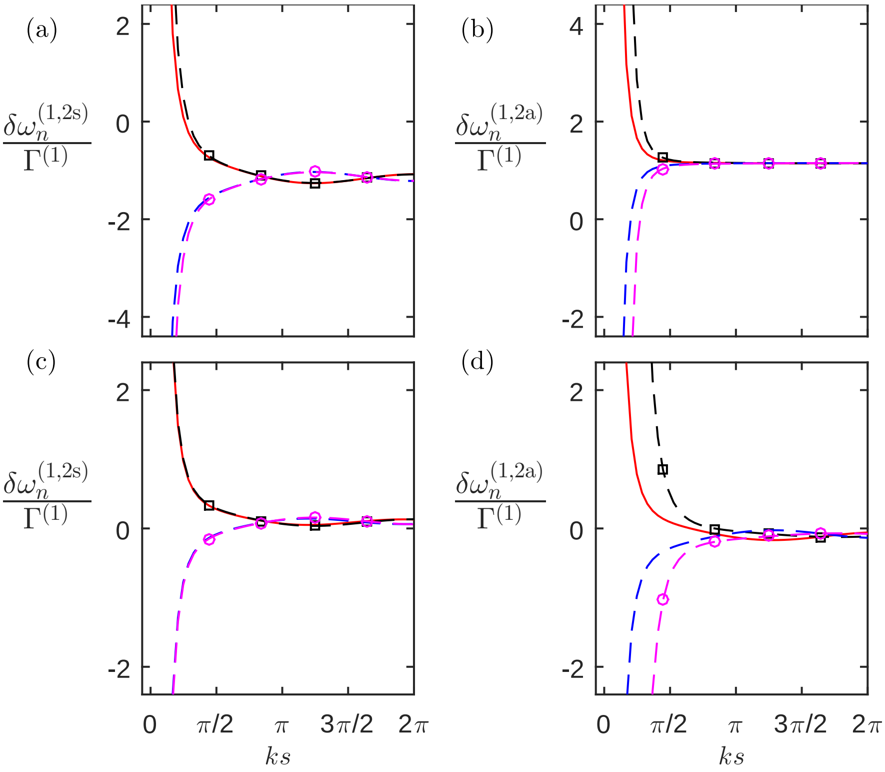

Figure E.3: The radiative resonance line shift $\delta\omega$ for the collective eigenmodes as a function of the separation parameter l, for two perpendicular pairs of point electric dipoles, with: (a) and (b) $kl = \pi/4$; and (c) and (d) $kl = 2\pi$. For plot descriptions, see Figure E.1 caption.

Appendix F

Scattering using the Drude model

In this Appendix, we consider the scattering and polarizability of small metallic nanorods in order to estimate the resonance frequency, as well as the radiative and ohmic decay rates of a single nanorod. In Chapter 1, we introduced the Drude model of the relative permittivity ϵ_r for a free electron gas [75]

$$\epsilon_\mathrm{r}(\omega) = \epsilon_\infty - \frac{\omega_p^2}{\omega(\omega + i\Gamma_\mathrm{D})}\,, \tag{F.1}$$

where ϵ_∞ is the permittivity at infinite frequencies, ω_p is the plasma frequency and Γ_D is the decay rate of current oscillations within the material. The scattering cross section of a small particle is dependent upon its polarizability α [75] and the wavelength λ of the incident field

$$\sigma_\mathrm{sc} = \frac{8\pi^3}{3\lambda^4}|\alpha|^2\,. \tag{F.2}$$

The polarizability depends on the physical characteristics of the particle, including its volume V_0 and geometry, which is introduced through the depolarization factor L [75]. In the Rayleigh approximation, the polarizability is

$$\alpha_i = V_0\frac{\epsilon_\mathrm{r} - 1}{1 + L_i(\epsilon_\mathrm{r} - 1)}, \qquad i = x, y, z\,. \tag{F.3}$$

The depolarization factor for a cylinder (with radius a and height H) aligned along the z axis is [94, 95]

$$L_x = L_y = \frac{1}{2\sqrt{1+\kappa^2}} \quad \text{and} \quad L_z = 1 - \frac{1}{\sqrt{1+\kappa^2}}\,, \tag{F.4}$$

where $\kappa = 2a/H$ is the aspect ratio of the cylinder. The curve produced by the scattering cross section equation (F.2), has two Lorentzian profiles with two independent resonance frequencies. There is a resonance representing the longitudinal polarizability α_z with depolarization factor L_z, and a separate resonance for the radial polarizability $\alpha_x = \alpha_y$ with depolarization factors $L_x = L_y$.

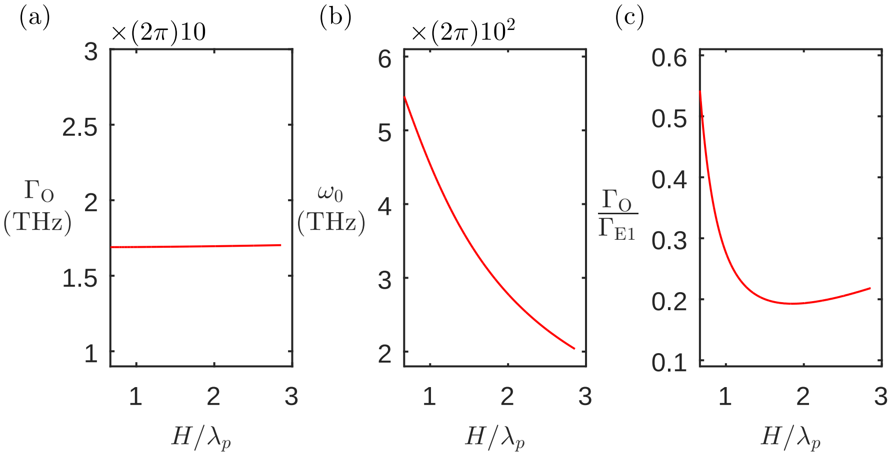

Figure F.1: The ohmic losses, resonance frequency and relative radiative decay rate as a function of the rod length for a gold nanorod with radius $a = \lambda_p/5$. We show: (a) the ohmic losses Γ_{O}; (b) the resonance frequency ω_0; and (c) the relative radiative decay rate $\Gamma_{\mathrm{O}}/\Gamma_{\mathrm{E1}}$.

For gold, the Drude parameters are [76, 77, 78]: $\epsilon_\infty = 9.5$; $\omega_p = (2\pi)2200$ THz; and $\Gamma_{\mathrm{D}} = (2\pi)17$ THz. In the Rayleigh approximation the full width at half maximum (FWHM) of the scattering cross section equation (F.2) is approximately independent of the length of the rod and gives the value of the ohmic loss rate Γ_{O}. In Figures F.1(a) and F.1(b) we show Γ_{O} and resonance frequency ω_0 for a gold nanorod with radius $a = \lambda_p/5$, where $\lambda_p = 2\pi c/\omega_p \simeq 139$ nm. We find $\Gamma_{\mathrm{O}} \simeq \Gamma_{\mathrm{D}} \simeq (2\pi)17$ THz.

For larger particles, the Rayleigh approximation is insufficient and retardation effects must be considered. Mie's formulation accounts for this retardation for spherical particles. In Reference 84, a generalization of Mie's polarizability is obtained for non-spheroidal particles that has been used successfully to model the scattering of metallic nanoparticles. The approximate ratio of ohmic losses to the radiative decay rate is

$$\begin{aligned}\frac{\Gamma_{\mathrm{O}}}{\Gamma_{\mathrm{E1}}} &= -\mathrm{Im}\left(\frac{3\lambda_0^3}{4\pi^3 a^2 H(\epsilon_{\mathrm{r}}-1)}\right), \\ &= \frac{6\Gamma_{\mathrm{D}}\omega_p^2 c^3}{a^2 H\omega_0^2\left[\omega_0^2\Gamma_{\mathrm{D}}^2(\epsilon_\infty-1)+\left(\omega_0^2(\epsilon_\infty-1)-\omega_p^2\right)^2\right]}. \qquad \text{(F.5)}\end{aligned}$$

In Figure F.1(c), we show the relative decay rates as a function of the rod length. For shorter rods $H < \lambda_p$, the ohmic losses are dominant. For longer rods the radiative emission rate is dominant. For $\lambda_p < H < 3\lambda_p$ the radiative decay rate is approximately constant, $\Gamma_{\mathrm{E1}} \approx 5\Gamma_{\mathrm{O}}$. In Chapters 3–5 we model the interactions between nanorods as point electric dipoles and as finite-size nanorods using this value. In Sections 5.3.2 and 5.3.3 where the length of the nanorod is important, the resonance frequency of each nanorod is assumed to depend upon the length of the rod as shown in Figure F.1.

Appendix G

Asymmetric coupling of collective modes

In Chapter 5.3.3, we showed how linearly polarized light could drive a toroidal dipole response in a metamolecule whose constituent rods vary in resonance frequency. We found an optimal variation in the limit that the resonance frequency shifts were much larger than the rod linewidths, and interactions between individual rods can be neglected. In this Appendix, we show how this scheme also works in the presence of interactions. Describing the evolution of the system in terms of collective eigenmodes of a symmetric metamolecule, we see how the introduced asymmetry couples collective metamolecule modes. We will see that a judicious combination of rod lengths can strongly couple an electric dipole mode (driven by the incident linearly polarized light) to the toroidal dipole mode (which is invisible to the incident field without rod asymmetries).

Formally, the evolution of the resonator excitations can be expressed in terms of the driven system of equations, equation (2.26). When all rods are of equal length $H_j = H_0$, the coupling matrix $\mathcal{C} = \mathcal{C}_{\text{sym}}$, and we denote the driving of the resonators as $\mathbf{F}_{\text{sym}}$, with elements $F_{\text{sym},j}$, given in equation (5.20). As discussed in Section 5.3.1, this symmetric metamolecule has eigenmodes of oscillation (labeled by index n) corresponding to eigenvectors $\mathbf{v}_n$ of $\mathcal{C}_{\text{sym}}$ and eigenvalues $\xi_n = -i\delta\omega_n - \gamma_n/2$, where $\delta\omega_n$ is the shift of the collective mode resonance frequency from the reference Ω_0, and γ_n is the collective decay rate, equation (2.29). Generally, any metamolecule excitation b can be expressed as

$$\mathbf{b} = \sum_n c_n(t)\mathbf{v}_n = \mathcal{S}\mathbf{c}\,, \tag{G.1}$$

where $\mathcal{S}$ is a matrix whose nth column is the eigenvector $\mathbf{v}_n$ of $\mathcal{C}_{\text{sym}}$, and $\mathbf{c} \equiv (c_1, \ldots, c_n)^T$. The electric dipole excitation $\mathbf{v}_{\text{E1}}$ directly driven by the incident field, and the toroidal dipole $\mathbf{v}_{\text{t}}$ are eigenmodes of the symmetric metamolecule. When the two layers of nanorods are separated by much less than a wavelength, the incident field drives only one of the two modes where the adjacent electric dipoles oscillate symmetrically, leaving all of the other modes, including the toroidal dipole unexcited.

Here, we generalize the treatment of Section 5.3.2, which dealt with the limit of non-interacting nanorods, to show how introducing an asymmetry into the rod lengths can lead to the excitation of a toroidal dipole. Perturbing the lengths of each rod j by δH_j during the fabrication, alters the coupling matrix $\mathcal{C}$. As discussed in Section 5.3.2, the primary consequence of altering the rod lengths is that each rod has its resonance frequency shifted by $\delta\omega_j$ proportional to δH_j, as indicated in Figure F.1. Additionally, changing rod lengths impacts the interactions between metamolecules. We denote the deviation of the coupling matrix from that of the symmetric system as

$$\mathcal{A} \equiv \mathcal{C} - \mathcal{C}_{\text{sym}} \,. \tag{G.2}$$

From equation (2.26), the amplitude of each c_n in the expansion of equation (G.1) obeys

$$\dot{\mathbf{c}} = \left[\Lambda + \mathcal{S}^{-1}\mathcal{A}\mathcal{S}\right]\mathbf{c} + \mathbf{f} + \delta\mathbf{f} \,, \tag{G.3}$$

where $\mathbf{f} \equiv \mathcal{S}^{-1}\mathbf{F}_{\text{sym}}$ is the vector of driving amplitudes for each individual mode, and Λ is the diagonal matrix of eigenvalues of $\mathcal{C}_{\text{sym}}$. Changing the lengths of the nanorods also alters the driving by $\delta\mathbf{f} \equiv \mathcal{S}^{-1}\delta\mathbf{F}$, where $\delta F_j = \delta \mathcal{F}_j \cos\theta_j$ is the change in driving amplitude experienced by nanorod j, and $\delta\mathcal{F}_j$ is the change in driving amplitude a nanorod would experience if it were oriented along the incident field polarization, as discussed in Section 5.3.2. Essentially, altering the lengths of the nanorods induces coupling between the eigenmodes via the asymmetry matrix $\mathcal{S}^{-1}\mathcal{A}\mathcal{S}$. At the same time, whilst a linearly polarized incident field only drives electric dipole modes in the symmetric metamolecule, a non-zero $\delta\mathbf{f}$ introduced by the asymmetry permits other modes to be driven directly by the incident field.

As in Section 5.3.2, our goal in altering the lengths is to find a perturbation that permits the excitation of the toroidal dipole mode, while reducing the contribution of other collective modes. In particular, consider the steady-state excitation induced by a field resonant on the toroidal dipole of the symmetric system

$$\mathbf{c} = -\left[\Lambda + i\delta\omega_{\text{t}} + \mathcal{S}^{-1}\mathcal{A}\mathcal{S}\right]^{-1}(\mathbf{f} + \delta\mathbf{f}) \,,$$

where the subscript ‘t’ refers to the toroidal dipole mode. Since altering the lengths of the nanorods induces coupling between the modes, one can produce a toroidal dipole excitation by introducing a coupling between the toroidal dipole mode and other modes in the metamolecule, in particular the electric dipole mode. In general, one would obtain the optimal excitation of the toroidal dipole by optimizing the nanorod length perturbations δH_j. The general optimization procedure would account for changes in interactions between resonators produced by the asymmetry as well as the interactions that are present in the symmetric metamolecule.

Here, we illustrate how the lengths of the nanorods would be chosen when the only effect of δH_j is to produce changes in resonance frequencies $\delta\omega_j = \chi\delta H_j$ and individual nanorod decay rates $\delta\Gamma_j = \nu\delta H_j$ in proportion to δH_j for some constants χ and ν. In this case, the matrix $\mathcal{A} = \mathrm{diag}\left(-i\delta\omega_1 - \delta\Gamma_1/2, \ldots, -i\delta\omega_N - \delta\Gamma_N/2\right)$. We will also assume the separation between rod layers is much less than a wavelength so that each layer experiences an identical driving. In these limits, we ask the question: what conditions would have to be satisfied to have the steady-state response of the metamolecule to be purely in the toroidal dipole mode? From there, we deduce a combination of δH_j, that could yield a toroidal dipole response. Consider an excitation of the form $\mathbf{b} = c_0\mathbf{v}_\mathrm{t}$ at time $t = t_0$, entirely in the toroidal dipole mode. Then, from equations (2.26), (5.20) and (5.21), we have, for each nanorod j,

$$\left.\frac{db_j}{dt}\right|_{t=t_0} = -c_0\frac{\gamma_\mathrm{t}}{2}\mathbf{v}_\mathrm{t}(j) - ic_0(\chi - i\nu)\delta H_j\mathbf{v}_\mathrm{t}(j) + (F_0 + \delta F_j)\cos\theta_j \,. \tag{G.4}$$

From equation (G.4), we see that if γ_t is negligible (i.e., $\gamma_\mathrm{t} \ll \delta\omega_j$, Γ), the toroidal excitation is in the steady state when for each nanorod j, δH_j solves

$$ic_0(\chi - i\nu)\delta H_j\mathbf{v}_\mathrm{t}(j) = (F_0 + \delta F_j)\cos\theta_j \,. \tag{G.5}$$

As in Section 5.3.2, where we considered non-interacting metamolecules, to lowest order in δH_j, the asymmetry in nanorod lengths needed to generate a toroidal dipole is given by equation (5.24).

Thus, when the collective decay rate $\gamma_\mathrm{t} \ll \delta\omega_j$, and we have neglected how the asymmetry of rod lengths alters interactions between the nanorods, the asymmetry of equation (5.24) would yield a toroidal dipole amplitude

$$c_0 = -i\sqrt{N}\frac{F_0}{(\chi - i\nu)\delta H_0} \,.$$

This is remarkably similar in form to the toroidal dipole amplitude one would obtain if one neglected all interactions between nanorods, as done in Section 5.3.2. In accounting for interactions, we no longer need to assume that $\delta\omega_j \gg \Gamma$. One does, however, need to drive the metamolecule with a field resonant on the toroidal dipole mode of the symmetric metamolecule, rather than resonant with a single nanorod.

References

[1] D. W. Watson, S. D. Jenkins, J. Ruostekoski, V. A. Fedotov, and N. I. Zheludev, "Toroidal dipole excitations in metamolecules formed by interacting plasmonic nanorods," Phys. Rev. B **93**, 125420 (2016).

[2] D. W. Watson, S. D. Jenkins, and J. Ruostekoski, "Point dipole and quadrupole scattering approximation to collectively responding resonator systems," Phys. Rev. B **96**, 035403 (2017).

[3] V. G. Veselago, "Properties of materials having simultaneously negative values of the dielectric ϵ and the magnetic μ susceptibilites," Sov. Phys. Usp **10**, 509 (1968).

[4] J. Pendry, A. Holden, D. Robbins, and W. Stewart, "Magnetism from conductors and enhanced nonlinear phenomena," IEEE Trans. Microwave Theory Tech. **47**, 2075 (1999).

[5] V. M. Shalaev, "Optical negative-index metamaterials," Nat Photon **1**, 41 (2007).

[6] D. R. Smith, W. J. Padilla, D. C. Vier, S. C. Nemat-Nasser, and S. Schultz, "Composite medium with simultaneously negative permeability and permittivity," Phys. Rev. Lett. **84**, 4184 (2000).

[7] R. A. Shelby, D. R. Smith, and S. Schultz, "Experimental verification of a negative index of refraction," Science **292**, 77 (2001).

[8] A. Biswas, I. S. Bayer, A. S. Biris, T. Wang, E. Dervishi, and F. Faupel, "Advances in topdown and bottomup surface nanofabrication: Techniques, applications & amp; future prospects," Adv. Colloid and Interface Sci. **170**, 2 (2012).

[9] B. D. Gates, Q. Xu, M. Stewart, D. Ryan, C. G. Willson, and G. M. Whitesides, "New approaches to nanofabrication: molding, printing, and other techniques," Chem. Rev. **105**, 1171 (2005).

[10] A. A. Tseng, K. Chen, C. D. Chen, and K. J. Ma, "Electron beam lithography in nanoscale fabrication: recent development," IEEE Trans. Elec. Pack. Man. **26**, 141 (2003).

[11] N. Jana, “Gram-scale synthesis of soluble, near-monodisperse gold nanorods and other anisotropic nanoparticles,” Small **1**, 875 (2005).

[12] C. Ziegler and A. Eychmller, “Seeded growth synthesis of uniform gold nanoparticles with diameters of 15300 nm,” J. Phys. Chem. C **115**, 4502 (2011).

[13] N. I. Landy, S. Sajuyigbe, J. J. Mock, D. R. Smith, and W. J. Padilla, “Perfect metamaterial absorber,” Phys. Rev. Lett. **100**, 207402 (2008).

[14] V. M. Shalaev, “Optical negative-index metamaterials,” Nat. Photon **1**, 41 (2007).

[15] A. Alu and N. Engheta, “Pairing an epsilon-negative slab with a mu-negative slab: resonance, tunneling and transparency,” IEEE Trans. Antennas Propag **51**, 2558 (2003).

[16] D. Schurig, J. J. Mock, B. J. Justice, S. A. Cummer, J. B. Pendry, A. F. Starr, and D. R. Smith, “Metamaterial electromagnetic cloak at microwave frequencies,” Science **314**, 977 (2006).

[17] J. B. Pendry, D. Schurig, and D. R. Smith, “Controlling electromagnetic fields,” Science **312**, 1780 (2006).

[18] J. B. Pendry, “Negative refraction makes a perfect lens,” Phys. Rev. Lett. **85**, 3966 (2000).

[19] Z. Jacob, L. V. Alekseyev, and E. Narimanov, “Optical hyperlens: Far-field imaging beyond the diffraction limit,” Opt. Express **14**, 8247 (2006).

[20] A. Grbic and G. V. Eleftheriades, “Overcoming the diffraction limit with a planar left-handed transmission-line lens,” Phys. Rev. Lett. **92**, 117403 (2004).

[21] C. M. Soukoulis and M. Wegener, “Past achievements and future challenges in the development of three-dimensional photonic metamaterials,” Nat Photon **5**, 523 (2011).

[22] D. R. Smith, S. Schultz, P. Markoš, and C. M. Soukoulis, “Determination of effective permittivity and permeability of metamaterials from reflection and transmission coefficients,” Phys. Rev. B **65**, 195104 (2002).

[23] D. R. Smith and J. B. Pendry, “Homogenization of metamaterials by field averaging (invited paper),” J. Opt. Soc. Am. B **23**, 391 (2006).

[24] A. V. Kildishev, A. Boltasseva, and V. M. Shalaev, “Planar photonics with metasurfaces,” Science **339** (2013).

[25] Z. H. Jiang, S. Yun, L. Lin, J. A. Bossard, D. H. Werner, and T. S. Mayer, “Tailoring dispersion for broadband low-loss optical metamaterials using deep-subwavelength inclusions,” Sci. Rep. **3**, 1571 (2013).

[26] F. Monticone, N. M. Estakhri, and A. Alù, “Full control of nanoscale optical transmission with a composite metascreen,” Phys. Rev. Lett. **110**, 203903 (2013).

[27] N. Liu, L. Langguth, T. Weiss, J. Kastel, M. Fleischhauer, T. Pfau, and H. Giessen, “Plasmonic analogue of electromagnetically induced transparency at the drude damping limit,” Nat Mater **8**, 758 (2009).

[28] A. Lovera, B. Gallinet, P. Nordlander, and O. J. Martin, “Mechanisms of fano resonances in coupled plasmonic systems,” ACS Nano **7**, 4527 (2013).

[29] J. A. Fan, C. Wu, K. Bao, J. Bao, R. Bardhan, N. J. Halas, V. N. Manoharan, P. Nordlander, G. Shvets, and F. Capasso, “Self-assembled plasmonic nanoparticle clusters,” Science **328**, 1135 (2010).

[30] N. Liu, M. Hentschel, T. Weiss, A. P. Alivisatos, and H. Giessen, “Three-dimensional plasmon rulers,” Science **332**, 1407 (2011).

[31] N. Verellen, P. Van Dorpe, C. Huang, K. Lodewijks, G. A. E. Vandenbosch, L. Lagae, and V. V. Moshchalkov, “Plasmon line shaping using nanocrosses for high sensitivity localized surface plasmon resonance sensing,” Nano Lett. **11**, 391 (2011).

[32] V. A. Fedotov, N. Papasimakis, E. Plum, A. Bitzer, M. Walther, P. Kuo, D. P. Tsai, and N. I. Zheludev, “Spectral collapse in ensembles of metamolecules,” Phys. Rev. Lett. **104**, 223901 (2010).

[33] V. A. Fedotov, M. Rose, S. L. Prosvirnin, N. Papasimakis, and N. I. Zheludev, “Sharp trapped-mode resonances in planar metamaterials with a broken structural symmetry,” Phys. Rev. Lett. **99**, 147401 (2007).

[34] A. M. Kern and O. J. F. Martin, “Excitation and reemission of molecules near realistic plasmonic nanostructures,” Nano Lett. **11**, 482 (2011).

[35] D. N. Chigrin, C. Kremers, and S. V. Zhukovsky, “Plasmonic nanoparticle monomers and dimers: from nanoantennas to chiral metamaterials,” App. Phys. B **105**, 81 (2011).

[36] A. Artar, A. A. Yanik, and H. Altug, “Directional double fano resonances in plasmonic hetero-oligomers,” Nano Lett. **11**, 3694 (2011).

[37] Z.-J. Yang, Z.-S. Zhang, Z.-H. Hao, and Q.-Q. Wang, “Fano resonances in active plasmonic resonators consisting of a nanorod dimer and a nano-emitter,” App. Phys. Lett. **99**, 081107 (2011).

[38] J. Petschulat, A. Chipouline, A. Tünnermann, T. Pertsch, C. Menzel, C. Rockstuhl, T. Paul, and F. Lederer, “Simple and versatile analytical approach for planar metamaterials,” Phys. Rev. B **82**, 075102 (2010).

[39] J. D. Jackson, *Classical Electrodynamics* (Wiley, New York, 1999).

[40] Morse and Feshbach, *Methods of Theoretical Physics, Part II* (McGraw-Hill, New York, 1953).

[41] L. D. Landau and E. M. Lifsshitz, eds., *The Classical Theory of Fields*, 4th ed., Course of Theoretical Physics, Vol. 2 (Pergamon, Amsterdam, 1975) pp. ii –.

[42] V. Dubovik and V. Tugushev, "Toroid moments in electrodynamics and solid-state physics," Phys. Reports **187**, 145 (1990).

[43] V. M. Dubovik and A. A. Cheskov, "Multipole expansion in classical and quantum field theory and radiation," Fiz. Elem. Chast. At. Yadra **5**, 791 (1974), [Sov. J. Part. Nucl. **5**, 318 (1974)].

[44] I. B. Zel'dovich, "Electromagnetic interaction with parity violation," Zh Eksp. Teor Fiz. **633**, 1531 (1957), [Sov. Phys. JETP **6**, 1184 (1958)].

[45] E. E. Radescu and D. H. Vlad, "Angular momentum loss by a radiating toroidal dipole," Phys. Rev. E **57**, 6030 (1998).

[46] E. E. Radescu and G. Vaman, "Exact calculation of the angular momentum loss, recoil force, and radiation intensity for an arbitrary source in terms of electric, magnetic, and toroid multipoles," Phys. Rev. E **65**, 046609 (2002).

[47] A. T. Góngora and E. Ley-Koo, "Complete electromagnetic multipole expansion including toroidal moments," Rev. Mex. Fis. E **52(2)**, 188 (2006).

[48] K. Marinov, A. D. Boardman, V. A. Fedotov, and N. Zheludev, "Toroidal metamaterial," New J. Phys. **9**, 324 (2007).

[49] N. Papasimakis, V. A. Fedotov, V. Savinov, T. A. Raybould, and N. I. Zheludev, "Electromagnetic toroidal excitations in matter and free space," Nat Mater **15**, 263 (2016).

[50] T. Kaelberer, V. A. Fedotov, N. Papasimakis, D. P. Tsai, and N. I. Zheludev, "Toroidal dipolar response in a metamaterial," Science **330**, 1510 (2010).

[51] V. A. Fedotov, A. V. Rogacheva, V. Savinov, D. P. Tsai, and N. I. Zheludev, "Resonant transparency and non-trivial non-radiating excitations in toroidal metamaterials," Sci. Rep. **3** (2013).

[52] Y. Fan, Z. Wei, H. Li, H. Chen, and C. M. Soukoulis, "Low-loss and high-q planar metamaterial with toroidal moment," Phys. Rev. B **87**, 115417 (2013).

[53] Q. W. Ye, L. Y. Guo, M. H. Li, Y. Liu, B. X. Xiao, and H. L. Yang, "The magnetic toroidal dipole in steric metamaterial for permittivity sensor application," Phys. Scr. **88**, 055002 (2013).

[54] Z.-G. Dong, J. Zhu, J. Rho, J.-Q. Li, C. Lu, X. Yin, and X. Zhang, "Optical toroidal dipolar response by an asymmetric double-bar metamaterial," Appl. Phys. Lett. **101**, 144105 (2012).

[55] Y.-W. Huang, W. T. Chen, P. C. Wu, V. Fedotov, V. Savinov, Y. Z. Ho, Y.-F. Chau, N. I. Zheludev, and D. P. Tsai, "Design of plasmonic toroidal metamaterials at optical frequencies," Opt. Express **20**, 1760 (2012).

[56] Y.-W. Huang, W. T. Chen, P. C. Wu, V. A. Fedotov, N. I. Zheludev, and D. P. Tsai, "Toroidal lasing spaser," Sci. Rep. **3** (2013).

[57] V. Savinov, V. A. Fedotov, and N. I. Zheludev, "Toroidal dipolar excitation and macroscopic electromagnetic properties of metamaterials," Phys. Rev. B **89**, 205112 (2014).

[58] Z.-G. Dong, J. Zhu, X. Yin, J. Li, C. Lu, and X. Zhang, "All-optical hall effect by the dynamic toroidal moment in a cavity-based metamaterial," Phys. Rev. B **87**, 245429 (2013).

[59] Z.-G. Dong, P. Ni, J. Zhu, X. Yin, and X. Zhang, "Toroidal dipole response in a multifold double-ring metamaterial," Opt. Express **20**, 13065 (2012).

[60] H. Wang, E. Yan, E. Borguet, and K. Eisenthal, "Second harmonic generation from the surface of centrosymmetric particles in bulk solution," Chem. Phys. Lett. **259**, 15 (1996).

[61] B. K. Canfield, S. Kujala, H. Husu, M. Kauranen, B. Bai, J. Laukkanen, M. Kuittinen, Y. Svirko, and J. Turunen, "Local-field and multipolar effects in the second-harmonic response of arrays of metal nanoparticles," J. Nonlinear Opt. Phys. Mater. **16**, 317 (2007).

[62] S. A. Maier and H. A. Atwater, "Plasmonics: Localization and guiding of electromagnetic energy in metal/dielectric structures," J. Appl. Phys. **98** (2005).

[63] A. Zangwill, *Modern Electrodynamics* (Cambridge University Press, New York, 2013).

[64] Born and Wolf, *Principles of Optics*, 4th ed. (Pergamon Press, Oxford, Oxford, 1970).

[65] J. A. Stratton, *Electromagnetic Theory* (McGraw–Hill, New York, 1941).

[66] C. G. Gray and B. G. Nickel, "Debye potential representation of vector fields," Am. J. Phys. **46** (1978).

[67] N. Yu and F. Capasso, "Optical negative-index metamaterials," Nat. Mater. **13**, 139 (2014).

[68] C. Sönnichsen and A. P. Alivisatos, "Gold nanorods as novel nonbleaching plasmon-based orientation sensors for polarized single-particle microscopy," Nano Lett. **5**, 301 (2005).

[69] F. M. van der Kooij, K. Kassapidou, and H. N. W. Lekkerkerker, "Liquid crystal phase transitions in suspensions of polydisperse plate-like particles," Nature **406**, 868 (2000).

[70] . Catherine J. Murphy, T. K. Sau, A. M. Gole, C. J. Orendorff, J. Gao, L. Gou, S. E. Hunyadi, and T. Li, "Anisotropic metal nanoparticles: synthesis, assembly, and optical applications," J. Phys. Chem. B **109**, 13857 (2005).

[71] E. Hao, K. L. Kelly, J. T. Hupp, and G. C. Schatz, "Synthesis of silver nanodisks using polystyrene mesospheres as templates," J. Am. Chem. Soc. **124**, 15182 (2002).

[72] G. L. Hornyak, C. J. Patrissi, and C. R. Martin, "Fabrication, characterization, and optical properties of gold nanoparticle/porous alumina composites: the non-scattering maxwellgarnett limit," J. Phys. Chem. B **101**, 1548 (1997).

[73] D. L. Feldheim and C. A. Foss Jr, *Metal Nanoparticles: Synthesis, Characterization, and Applications* (Marcel Dekker, New York, 2002).

[74] H. U. Yang, J. D'Archangel, M. L. Sundheimer, E. Tucker, G. D. Boreman, and M. B. Raschke, "Optical dielectric function of silver," Phys. Rev. B **91**, 235137 (2015).

[75] C. Bohren and D. Huffman, *Absorption and Scattering of Light by Small Particles* (Wiley VCH Verlag GmbH & Co. KGaA, Weinheim, Germany, 2004).

[76] P. B. Johnson and R. W. Christy, "Optical constants of the noble metals," Phys. Rev. B **6**, 4370 (1972).

[77] E. J. Zeman and G. C. Schatz, "An accurate electromagnetic theory study of surface enhancement factors for silver, gold, copper, lithium, sodium, aluminum, gallium, indium, zinc, and cadmium," J. Phys. Chem. **91**, 634 (1987).

[78] N. Grady, N. Halas, and P. Nordlander, "Influence of dielectric function properties on the optical response of plasmon resonant metallic nanoparticles," Chem. Phys. Lett. **399**, 167 (2004).

[79] S. D. Jenkins and J. Ruostekoski, "Theoretical formalism for collective electromagnetic response of discrete metamaterial systems," Phys. Rev. B **86**, 085116 (2012).

[80] S. D. Jenkins and J. Ruostekoski, "Cooperative resonance linewidth narrowing in a planar metamaterial," New J. Phys. **14**, 103003 (2012).

[81] S. D. Jenkins and J. Ruostekoski, "Metamaterial transparency induced by cooperative electromagnetic interactions," Phys. Rev. Lett. **111**, 147401 (2013).

[82] S. D. Jenkins, J. Ruostekoski, N. Papasimakis, S. Savo, and N. I. Zheludev, "Many-body subradiant excitations in metamaterial arrays: Experiment and theory," ArXiv e-prints (2016).

[83] G. Adamo, J. Y. Ou, J. K. So, S. D. Jenkins, F. De Angelis, K. F. MacDonald, E. Di Fabrizio, J. Ruostekoski, and N. I. Zheludev, "Electron-beam-driven collective-mode metamaterial light source," Phys. Rev. Lett. **109**, 217401 (2012).

[84] H. Kuwata, H. Tamaru, K. Esumi, and K. Miyano, "Resonant light scattering from metal nanoparticles: Practical analysis beyond rayleigh approximation," Appl. Phys. Lett. **83**, 4625 (2003).

[85] B. Schrader, "Infrared and raman spectroscopy: Methods and applications," (Wiley-VCH Verlag GmbH, Weinheim, Germany, 2007).

[86] R. S. Mulliken, "Report on notation for the spectra of polyatomic molecules," J. Chem. Phys. **23** (1955).

[87] S. D. Jenkins and J. Ruostekoski, "Resonance linewidth and inhomogeneous broadening in a metamaterial array," Phys. Rev. B **86**, 205128 (2012).

[88] B. Luk'yanchuk, N. I. Zheludev, S. A. Maier, N. J. Halas, P. Nordlander, H. Giessen, and C. T. Chong, "The fano resonance in plasmonic nanostructures and metamaterials," Nat. Mater. **9**, 707 (2010).

[89] M. Fleischhauer, A. Imamoglu, and J. P. Marangos, "Electromagnetically induced transparency: Optics in coherent media," Rev. Mod. Phys. **77**, 633 (2005).

[90] M. Hentschel, D. Dregely, R. Vogelgesang, H. Giessen, and N. Liu, "Plasmonic oligomers: The role of individual particles in collective behavior," ACS Nano **5**, 2042 (2011).

[91] I. S. Gradshteyn and I. M. Ryzhik, *Table of Integrals, Series and Products, Seventh Edition* (Academic Press, 2007).

[92] C. G. Gray, "Multipole expansions of electromagnetic fields using debye potentials," Am. J. Phys. **46** (1978).

[93] R. G. Barrera, G. A. Estevez, and J. Giraldo, "Vector spherical harmonics and their application to magnetostatics," Eur. J. Phys. **6**, 287 (1985).

[94] V. I. Emel'yanov, "Defect-deformational surface roughening and melting and giant enhancement of optical processes at surface of solids," Laser Physics **8**, 937 (1998).

[95] V. I. Emel'yanov, E. M. Zemskov, and V. N. Seminogov, "The influence of collective effects on the local field resonance in the interaction between radiation and a rough solid surface," Phys. Chem. Mech. Surfaces **3**, 381 (1985).